# TRANSITION METAL-BASED CATALYSTS FOR ENHANCED OXYGEN ELECTROCATALYTIC REACTION

by

Ziqi Liu

A thesis submitted in partial satisfaction of
requirements for the degree of Doctor of Philosophy
August 2022

in

Mechanical Engineering

Committee in charge:
Professor Po-Ya (Abel) Chuang
Professor Ashlie Martini
Professor Son Nguyen
Professor Min Hwan Lee

The thesis of Ziqi Liu is approved:

| | |
|---|---|
| Po-Ya Abel Chuang, Chair | Date |
| Ashlie Martini | Date |
| Son Nguyen | Date |
| Min Hwan Lee, Advisor | Date |

# ACKNOWLEDGEMENTS

I would like to acknowledge my advisor, Min Hwan Lee, for his kind patience, guidance, and support of me during these 5 years.

I am deeply grateful to all my mentors and committee members who dedicated their time and helped me at every stage of the research project: Abel Chuang, James Palko, Ashlie Martini, Son Nguyen.

I would like to offer my special thanks to my colleges: Angela Macedo Andrade, Simranjit Kaur Grewal, Haoyu Li, Hung-Sen Kang, Orbel Barkhordarian and Alireza Karimaghaloo for a cherished time spent together in the lab, and in social settings.

I also want to acknowledge and recognize my friends Cheng Chen, Di An, Ruihao Li who were always there for me, supporting and encouraging me every step through.

Finally, I would like to express my gratitude to my parents, my wife Yuan, and my children Chloe. Without their tremendous understanding and encouragement in the past few years, it would be impossible for me to complete my study.

# TABLE OF CONTENTS

# LIST OF FIGURES

# CURRICULUM VITAE: Ziqi Liu

**Education**

| | |
|---|---|
| Ph.D., Mechanical Engineering | Aug. 2017 - present |
| *University of California, Merced, CA* | GPA: 3.69/4.0 |
| Courses: Transport Phenomena, Fuel Cell Fundamentals, Modeling and Diagnostic etc. | |
| M.S., Materials Engineering | Aug. 2014 - May. 2016 |
| University of Southern California, Los Angeles, CA | GPA: 3.44/4.0 |
| Courses: Basics of Atomistic Simulation of Materials, etc. | |
| B.S., Material Chemistry | Sep. 2010 - Jul. 2014 |
| Qingdao University of Science and Technology, China | GPA: 3.10/4.0 |
| Courses: Material Surface and Interface Chemistry, etc. | |

**Research experience**

*3D transition metal doped carbon-based fuel cell catalysts*

*Ph.D.*

- Prepared a mixed metal/metal oxide integrated N-doped 3-D carbon structure via ALD and achieved excellent bifunctional oxygen electrocatalytic performance.
- Quasi-operando XPS and XRD analysis to investigate the active sites for the enhancement.

*Core shell nanostructure with enhanced oxygen evolution reaction*

*Ph.D.*

- Synthesized a unique 3D core-shell structure with enhanced OER performance.
- Characterization of as-prepared BDC@CoNi-LDH structure with different tools: SEM, TEM, XRD, Raman, XPS, FT-IR, XAS, BET.
- Quasi-operando and ex-situ studies to reveal the active site of the sample.

*Basics of Atomistic Simulation of Materials* *M.S.*

- Monte Carlo and Molecular dynamic simulation project were designed for computing the pi value and the motion of atoms in different argon phases. The Newtonian equations of motion was applied to study the structural, transport properties under different thermodynamics state

*The Graphene/Nickel Materials' Electrocatalytic Activity for Methanol Oxidation in Alkaline Environment*

*B.S.*

- Graphene-supported different proportion of Pt, Ni catalysts were prepared with ethylene glycol as the reducing agent.
- Lower the price of the catalysts while maintain the overall electrochemical performance.

*Controllable Synthesis and Electrichemical Property of two-Dimensional Antimony Chalcogenide Nanomaterials, Journal of Alloys and Compounds* *B.S.*

- Employed polyacids and polyols as templates to prepare nanostructured Antimony Chalcogenide via hydrothermal/solvothermal method.
- Investigated the formation mechanism of these antimony chalcogenide nanomaterials.

**Publications**

[1] **Z. Liu**, H. Li, H. Kang, A. T. Diaye, M. H. Lee, Facile fabrication of Layered double hydroxide core-shell structure derived from Metal-organic framework for efficient oxygen evolution reaction, *Chemical Engineering Journal*, in revision

[2] **Z. Liu**, A. Macedo Andrade, S. Grewal, A. J. Nelson, K. Thongrivong, H.-S. Kang, H. Li, Z. Nasef, G. Diaz, M. H. Lee*, Trace Amount of Ceria Incorporation by Atomic Layer Deposition in Co/CoOx-embedded N-doped Carbon for Efficient Bifunctional Oxygen Electrocatalysis: Demonstration and Quasi-Operando Observations, *International Journal of Hydrogen Energy*, **46**, 38258, 2021

[3] A. Macedo Andrade, **Z. Liu**, S. Grewal, A. J. Nelson, Z. Nasef, G. Diaz, M. H. Lee*, MOF- derived Co/Cu-embedded N-doped Carbon for Trifunctional ORR/OER/HER Catalysis in Alkaline Media, *Dalton Transactions*, **50**, 5473, 2021

[4] S. Grewal, A. Macedo Andrade, **Z. Liu**, J. A. Garrido Torres, A. J. Nelson, A. Kulkarni, M. Bajdich*, M. H. Lee*, "Highly Active Bifunctional Oxygen Electrocatalytic Sites Realized in Ceria–Functionalized Graphene", *Advanced Sustainable Systems*, **4**, 2000048, 2020

[5] Rencheng Jin, **Ziqi Liu**, Lixia Yang, Junshen Liu, Yanbin Xu, Guihua Li. "Facile synthesis of sulfur doped Sb2Se3 nanosheets with enhanced electrochemical performance*", Journal of Alloys and Compounds*, **579**, 209-217, 2013.

[6] Lixia Yang, Feng Wang and **Ziqi Liu**. Fabrication and Characterization of Manganese Ferrite Nanospheres as a Magnetic Adsorbent of Chromium, *Journal of Nanomaterials*, **2013**, 293464, 2013.

**Conference Presentations**

PRiME 2020 Oct.04 - Oct.09, 2020

Ceria Nanodots Anchored on ZIF67-Derived Framework by Atomic Layer Deposition for Efficient Bifunctional Oxygen Electrocatalysis.

236th ECS Meeting Oct.13 - Oct.17, 2019

Bimetallic Cobalt-Copper MOF Material for Bifunctional Oxygen Electrocatalysis.

AiMES 2018 Meeting Sep.30 - Oct.4, 2018

Co-Embedded Carbon Nano-Polyhedron Supported on Functionalized Graphene Oxide for Efficient Oxygen Reduction Reaction.

Uio-66 As an Effective Support of Metal Oxides for Oxygen Evolution Catalysis.

**Fellowships**

School of Engineering ME Graduate Bobcat Fellowship Award Jun. 2020 - Aug. 2020

School of Engineering ME Graduate Bobcat Fellowship Award Jun. 2021 - Aug. 2021

School of Engineering ME Graduate Bobcat Fellowship Award Jun. 2022 - Aug. 2022

**Teaching Experience (Teaching Assistant)**

*Engineering Computing* Fall 2017/Spring 2018/Fall 2018/Fall 2019

· Introduction to Python, Matlab and Fortran.

· Concepts of formatted input/output, data types, variables, arrays, strings, variable scopes, logic statements, loops and repetition, functions and subroutines, and data graphing

*Statics and Dynamics* Spring 2019/Fall 2020

· Guide student on developing an understanding of the fundamentals and principles of engineering mechanics: statics and dynamics of particles and rigid bodies in two and three dimensions

· Theory and applications are complemented by demonstrations, hands-on exercises, and lab assignments. The labs endeavor to give students a hands-on feel for both quantities and concepts.

*Fluid mechanics* Fall 2021/Spring 2022

· Introduce engineers to the mechanics of fluids in natural and engineered system and guide student on analyzing internal and external flows as well as perform design of flow systems.

Engineering Capstone Design Spring 2020

· Guidance of students working on multidisciplinary teams on selected and approved design projects, practice design methodology, complete project feasibility study and preliminary design, including optimization, product reliability and liability, economics, and application of engineering codes.

**Professional Skills**

| | |
|---|---|
| Material Characterization | SEM, TEM, XRD, XPS, Raman, FT-IR, AFM, BET |
| 3D Modeling tools | ANSYS Workbench, AutoCAD, 3DS Max, Materials Studio |
| Data acquire and analysis | Electrochemical workstation, Oscilloscope, Signal generator, JMP, Origin Pro |
| Engineering | Modal analysis, static structure analysis, mechanics of materials |
| Languages | MATLAB, Python, Fortran |

# ABSTRACT

The development of high efficiency and cost-effective bifunctional electrocatalysts for both oxygen reduction reaction (ORR) and oxygen evolution reaction (OER) is critical to a wide commercialization of metal-air batteries and unified regenerative fuel cells. Pt and $IrO_2$ and their alloys have been applied as favorable catalysts due to their prominent performance. However, their high cost, low stability and susceptibility to poisoning greatly limit their widespread commercial adoption. Transition metal has been regarded as a good alternative to noble metal-based catalysts because of their tunable valence state, cost-effectiveness and variety of chemical composition, structure, and morphology. However, the catalytic activity of the transition metal electrocatalysts is largely hindered by their inherent corrosion and oxidation susceptibility. Therefore, my research mainly focusses on the development and modification of transition metal-based catalysts with enhanced catalytic activity towards ORR and OER.

In the first project (Chapter 4), I propose to investigate the beneficial effect of atomic layer deposition (ALD)-derived incorporation of transition metal-based materials for electrocatalytic oxygen reduction reaction (ORR) and oxygen evolution reaction (OER). Gas-evolving electrochemical reactions primarily occurs at the triple phase boundary regions where electrons, ions and reactant molecules meet altogether. Therefore, ALD-based dispersion of atomic-scale transition metal species can be an ideal approach for maximizing catalytically active sites. Our proposed research is to investigate the effect of ALD treatment of functionalized carbon-based materials with different transition metals on electrocatalytic ORR and OER reactions via both experimental and theoretical studies. In the first work, a mixed metal/metal oxide-integrated N-doped carbon is prepared by performing atomic layer deposition (ALD) of $CeO_2$ nanodots on a three-dimensional Co and N co-doped carbon polyhedron nanostructure derived from zeolitic imidazolate framework (ZIF; a type of metal-organic framework). An optimally prepared hybrid catalyst achieved excellent bifunctional oxygen electrocatalytic performance comparable to or even better than noble metal-based benchmark catalysts (Pt/C for ORR and $IrO_2$ for OER) thanks to the synergistic effect between Co and Ce, high-surface-area backbone structure, rich Co-$N_x$ moieties and oxygen vacancies. This work proves the effectiveness

of ALD in uniformly incorporating the second metal/metal oxide onto a monometallic system for enhanced electrocatalytic performance.

In the second project (Chapter 5), I demonstrate a unique 3D core-shell nanostructure for efficient OER electrocatalysis. Two-dimensional (2D) layered double hydroxides (LDHs) are promising as an effective electrocatalyst towards OER, but their poor conductivity and tendency to stack together limits their activity and durability as an electrocatalyst. Herein, 3D core-shell structures are synthesized through a facile one-step reaction strategy, in which the terephthalic acid and urea is employed as the organic ligand for the metal organic framework (MOF) precursor and surface coordination buffer between LDH and MOF. Benefiting from the hierarchical 3D microstructure with uniform nanosheets grown on the surface, the as-prepared electrocatalyst exhibits rich carbon edge sites and high electrochemical surface area. The representative sample (CoNi-BDC@LDH) achieves an OER activity with the overpotential of 280 mV at 100 mA $cm^{-2}$ and robust cyclic and chronoamperometric stability. A series of *quasi-operando* studies by X-ray absorption spectroscopy, X-ray photoelectron spectroscopy, Raman and Fourier-transform infrared spectroscopy further elucidate that Co-Ni acts as the main active site while the high valence state of Ni facilitates $O_2$ desorption from O-O bond linking metal sites. The high OER performance is additionally attributed to a high valence state of metal ions in $\gamma$-NiOOH/CoOOH, lattice edge sites of carbon, and a synergistic effect between neighboring metal atoms.

In the third study (Chapter 6), a Co-Ni based LDH structure with thin layer coating of ceria and/or titania by ALD is synthesized. Benefiting from the result of the first two project, ALD was applied to the LDH structure directly. The effects of tri-metal incorporation on the electrocatalytic properties of the resulting hybrid systems toward OER is further investigated. The primary electrochemical studies and XPS characterization results suggests the improved OER performance is mainly attributed to the synergistic effect between metal cations.

# CHAPTER 1. Background

## 1.1 Energy sources

Over the last century, global energy consumption has increased rapidly, driven by an increasing population and growing prosperity. Demand for virtually all energy sources has increased, including coal, oil, natural gas, nuclear power, and renewables. A combustion-based energy conversion using fossil fuels release large quantities of $CO_2$ and sulfide into the atmosphere. Despite the surging concern over global warming, the humankind is still heavily reliant on fossil fuels to meet much of our energy needs today; ~ 86 percent of the world's energy production comes from fossil fuels.[1] Global warming is the primary threat to the near-term future of life on Earth.[2–4] To address the imminent concern, it is critical to find and develop alternatives to fossil fuel in a timely manner.

In the last few years, there has been significant advances in the renewable energy technologies – in particular, of wind and solar energy – and their cost competitiveness. Wind energy is one of the cleanest and most environment-friendly source of electricity. Solar energy is another inexhaustible resource for generating clean and sustainable electricity.[1] However, they are strongly dependent on the weather conditions, and thus are intermittent and unpredictable. The generation of electricity from these energy sources are controlled by nature, not by human needs. Further, the electricity generated by these sources are momentary; those not stored or consumed at the time of production should be discarded. Therefore, for a stable and scalable renewable energy-based ecosystem, a massive scale energy storage scheme is indispensable.

Hydrogen and batteries are promising energy storage scheme for future energy ecosystem. They can generate and store electricity reversibly without producing toxic byproducts as opposed to other means of energy conversion.[5] In comparison to common internal combustion engines, fuel cells and batteries achieve a significantly higher efficiency. While other energy conversion scheme involves an intermediate energy state (e.g., heat energy, mechanical energy, etc.) before generating electricity, batteries and fuel cells convert chemical energy into electrical energy directly. As a result, the efficiency of

energy conversion in batteries and fuel cells reaches to >90% for batteries and >60% for fuel cells, much higher than those achieved by conventional combustion-based energy conversion. Fuel cells are exceptional in their ability to transform the energy locked up in chemical bonds into electrical energy efficiently. Fuel cells achieve this efficiency by transforming the chemical energy in a fuel directly into electrical energy without an intermediate step, producing more usable energy from the same amount of fuel than any other scheme.

There is no doubt that batteries are highly useful in a wide range of modern applications, especially for mobile devices, vehicular applications, and small-scale stationary energy storage. However, applying batteries to a scale of grid-level energy is a challenge due to their intrinsic nature in scaling. To scale the energy capacity by a thousand times, one needs to use a thousand times bigger battery. This will pose a significant challenge in both sourcing raw materials needed to build the battery system and achieving cost competitiveness. Hydrogen-based energy storage is drastically more advantageous in scaling into a massive scale. This is because the scaling of energy capacity is mainly achieved by using a larger hydrogen storage tank, not necessarily by making a proportionally larger fuel cell or electrolyzer stack.

Unlike batteries, fuel cells do not run out of power. They generate electricity and heat as long as fuel is supplied.[6] In a simple description, a fuel cell consists of two electrodes separated by an electrolyte membrane. A traditional fuel cell operates by providing hydrogen molecule to its anode and oxygen to the cathode. The hydrogen molecules are ionized at the anode while oxygen molecules are ionized at the cathode, both of which are facilitated by catalysts integrated in each electrode. The generated ions (protons, oxygen ions, or others, depending on the type of fuel cells) migrate through the electrolyte membrane while electrons are pushed through an external circuit, resulting in an electric current and some biproduct heat. The ions and electrons recombine to form water molecules, which has lower free energy than the reactants ($H_2$ and $O_2$). Fuel cells are quiet and potentially advantageous in achieving high durability because they have no moving components unlike a steam turbine or internal combustion engine.

A higher cell performance in fuel cells and electrolyzers is mainly achieved by the enhancement of electrocatalyst performance. Between the hydrogen and oxygen electrocatalysis in these devices, oxygen reactions – oxygen reduction reaction (ORR) and oxygen evolution reaction (OER) – have been studied more intensively due to their intrinsically sluggish kinetics and complicated reactino pathways in comparison to hydrogen reactions.

## 1.2 Oxygen reduction reaction and oxygen evolution reaction

Regenerative fuel cell (RFCs) has both fuel cell and electrolyzer components. In the fuel cell mode (Figure 1a), $H_2$ is provided and oxidized at anode, producing $H^+$ and $e^-$; $H_2 \rightarrow 2H^+ + 2e^-$ (hydrogen oxidation reaction; HOR). At the cathode, $H_2O$ is generated while $O_2$ is reduced into $O^{2-}$ and combined with the $H^+$ transferred from anode side; $O^2 + 4H^+ + 4e^- \rightarrow 2H_2O$ (ORR). Simultaneously, the electrons are collected and transported through an external electric circuit to power a device in need of electricity. The reactions are reversed in an electrolyzer (Figure 1b): water is oxidized to produce oxygen at the anode: $2H_2O \rightarrow O_2 + 4H^+ + 4e^-$ (OER), while $H^+$ and electrons are transferred to the anode forming hydrogen gas: $2H^+ + 2e^- \rightarrow H_2$ (hydrogen evolution reaction; HER).

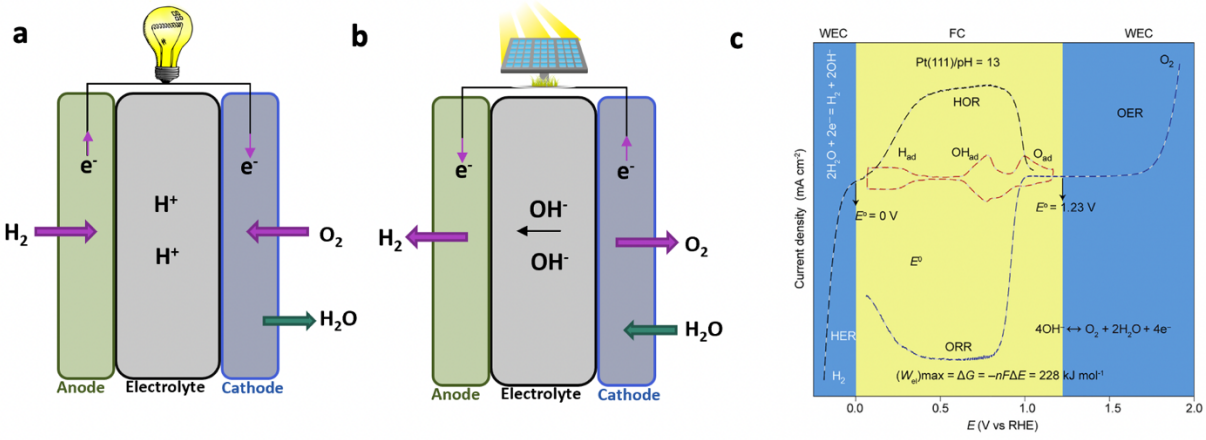


**Figure 1.1** Schematic diagrams of (a) fuel cell and (b) electrolyzer operation. (c) Representative polarization curves for related reactions: HER, HOR, OER, and ORR[7].

Since ORR and OER involve four electrons and generates multiple intermediates, they are orders of magnitude slower than HOR and HER.[7] Typically, molecular oxygen is electrochemically reduced by four electrons to form water or by two electrons to form hydrogen peroxide. The ORR in acid environment can be written as:

$$O_2 + 4H + 4e^- \rightarrow 2H_2O;\ E^0 = 1.229\ V\ vs.\ SHE \quad (1.1)$$

$$O_2 + 2H^+ + 2e^- \rightarrow H_2O_2;\ E^0 = 0.695\ V\ vs.\ SHE \quad (1.2)$$

$$H_2O_2 + 2H^+ + 2e^- \rightarrow H_2O_2\ E^0 = 1.776\ V\ vs.\ SHE \quad (1.3)$$

while the ORR in alkaline environment can be written as:

$$O_2 + 2H_2O + 4e^- \rightarrow 4OH^-;\ E^0 = 0.401\ V\ vs.\ SHE \quad (1.4)$$

$$O_2 + H_2O + 2e^- \rightarrow H_2O_2^- + OH^-;\ E^0 = -0.076\ vs.\ SHE \quad (1.5)$$

$$H_2O_2^- + H_2O + 2e^- \rightarrow 3OH^-;\ E^0 = 0.878\ V\ vs.\ SHE \quad (1.6)$$

There are mainly two ways for ORR to proceed. First, an adsorbed $O_2$ is dissociated and bonded on to a single active site on the surface of the catalyst (usually a single metal center or a defect site), forming M-O bond. It is further reduced to complete the four-electron reduction to generate water molecules. (Equation 1.7-1.9)

$$O_2 + 2^* \rightarrow 2^*O \quad (1.7)$$

$$2^*O + 2H^+ + 2e^- \rightarrow 2^*OH \quad (1.8)$$

$$2^*OH + 2H^+ + 2e^- \rightarrow 2H_2O + 2^* \quad (1.9)$$

Second, $O_2$ can be adsorbed on to a single metal center or two metal sites forming M-O-O or M-O-O-M bond, without dissociation of O-O bond into $^*O$. In this case, both $H_2O$ and $H_2O_2$ products will be created during the reduction process (Equation 1.10-1.15). The reason for the producing of $H_2O_2$ is due to the Pauling adsorption mode, which involves donation from an O-centered $sp^2$ hybrid orbital to the M-centered $d_{z2}$ orbital.[7] This configuration alone cannot contribute to the separation of O-O bond, and hence favor a selective two-electron reduction with $H_2O_2$ as a final product. (Equation 1.12)

$$O_2 + {}^* \rightarrow {}^*O_2 \quad (1.10)$$

$${}^*O_2 + H^+ + e^- \rightarrow {}^*OOH \quad (1.11)$$

$${}^*OOH + H^+ + e^- \rightarrow H_2O_2 \quad (1.12)$$

$${}^*OOH + H^+ + e^- \rightarrow {}^*O + H_2O \quad (1.13)$$

$${}^*O + H^+ + e^- \rightarrow {}^*OH \quad (1.14)$$

$${}^*OH + H^+ + e^- \rightarrow H_2O + {}^* \quad (1.15)$$

An OER process comprises four basic steps involving various reaction intermediates and O–O bond formation, which is ultimately released as molecular oxygen. The OER process in acid media is represented as:

$$2H_2O \rightarrow O_2 + 4H^+ + 4e^- \; E^0 = 1.23V \; vs. \; RHE \quad (1.16)$$

And, in alkaline media:

$$4OH^- \rightarrow O_2 + 2H_2O + 4e^- \; E^0 = 1.23V \text{ vs. RHE} \quad (1.17)$$

Additionally, there are two primary pathways proposed for the formation of O-O bond. Both steps start with the proton-coupled electron transfer (PCET) where the $H_2O$ moleculars are first adsorbed on the surface metal site.[8–10] For the first mechanism, O-O bond forming is carried out between two metal-oxo units, which will ultimately lead to peroxo-species, producing $O_2$ and regenerating the catalysts. In the latter mechanism, the adsorbed OH ($HO^*$ species) undergoes subsequent deprotonation to form $O^*$. The single $O^*$ site is then attacted by another water molecular to form $HOO^*$ intermediate. Finally, $O_2$ is generated through the deprotonation of $HOO^*$ with the regeneration of the metal active site.

$$H_2O + {}^* \rightarrow HO^* + H^+ + e^- \quad (1.18)$$

$$HO^* \rightarrow O^* + e^- + H^+ \quad (1.19)$$

$$2HO^* \rightarrow O_2{}^* + 2e^- + 2H^+ \quad (1.20)$$

$$O^* + H_2O \rightarrow HOO^* + H^+ + e^- \quad (1.21)$$

$$HOO^* \rightarrow O_2 + H^+ + e^- \quad (1.22)$$

Theoretical studies on scaling relation of ORR and OER based upon the Gibbs free energies of intermediate steps have been widely reported. Controlling the adsorption-free energies of these intermediates is crucial for the development of effective catalysts. Since both HOO* and HO* bind to the catalyst surface with a single bond via an oxygen atom, their binding energies are closely related, with a constant difference of $\Delta G(^*OOH) = \Delta G(^*OH) + 3.2 \pm 0.2$ eV for either metals or oxide surfaces, independent of the binding site. Similar scaling relationships also exist between the binding energy of various oxygen-containing intermediates for a series of catalysts, such as single metal-based materials, alloys, metal-doped carbon materials and non-metal nitrogen doped carbon catalysts. These relationship often result in a 'volcano plot' (Figure 2a and 2b) between catalytic activity and the rate limiting adsorption energies, which can be used as the descriptor for the optimization of the catalysts to obtain the lowest overpotential during the catalytic process.

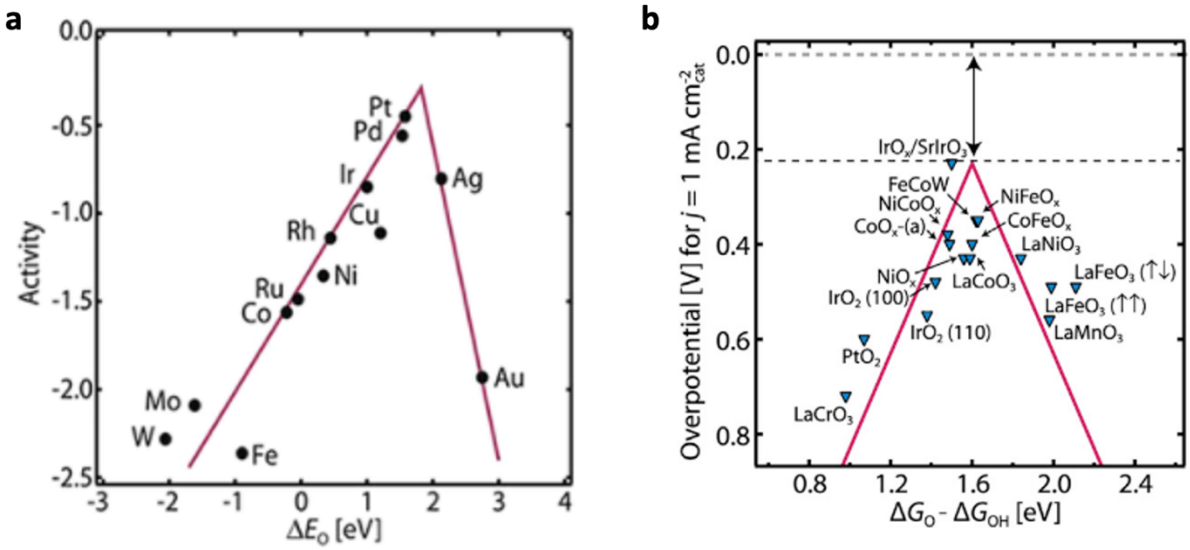


**Figure 1.2** (a) ORR volcano plot for metals. Copyright 2004, ACS. (b) OER volcano plot for metal oxides.[11] Copyright 2017, American Association for the Advancement of Science.

## 1.3 Electrocatalyst for ORR and OER

Substantial efforts have been devoted to the study of various types of catalysts for higher catalytic activity and conversion efficiency. To date, precious metal-based catalysts,

especially Pt-based and Ir/Ru-based catalysts, have been widely employed due to their superior electrocatalytic activity. The efficiency of the precious metal electrode materials is due to their d-band vacancies and shorter metal to metal interatomic distances that allow for strong metal-reactant interactions during the separation state (also known as dissociative adsorption) of ORR and OER.[12] However, high cost, lack of stability and scarcity prevent them from being applied to large scale utilization. Moreover, noble materials such as Pt/C and $RuO_2$ are not applicable as bifunctional catalysts for achieving both ORR and OER at the same time, which made them not suitable for metal-air batteries or unified regenerative fuel cells. For these reasons, intense efforts have been made to develop efficient bifunctional oxygen electrocatalysts with low cost and high durability.

### 1.3.1 MOF-based materials and its derivatives

A MOF is a two- or three-dimensional porous structure composed of organic ligands and metal ions (or metal clusters). It has been intensively studied and applied for energy conversion applications due to their highly ordered crystalline structures, high specific surface areas and structural designability.[13–15] Specifically, it is easy to dope highly scattered heteroatoms (such as metal atoms, nitrogen) into a MOF structure; heteroatom doping is widely used to customize the local electronic structure of catalysts, thus lowering the adsorption energy of intermediate species and improving catalytic efficiency. Furthermore, the morphology and structure of MOFs can be tuned by modifying the organic ligands and post synthesis modification, which provides us additional means of further improving catalytic performance.[6][16–18] For this purpose, MOFs with suitable metal ions, organic ligands, structures, and accessible defects can be developed in order to achieve highly efficient MOF-based catalysts. Series MOF structures such as MIL-53, ZIF-7, MOF-5 and Mn/Fe-HIB-MOF have exhibited promising ORR/OER properties.

Optimized MOF derivatives often have excellent electrocatalytic activities toward various reactions including ORR and OER due to the unique properties of MOFs. The high porosity of MOFs, for example, will render high surface areas, potentially with hierarchical structure for both efficient mass transport and higher catalytic activity. The uniform composition of MOFs also ensures that active sites are embedded uniformly within the

catalyst structure. A wide range of pore cavities makes MOFs suitable for hosting different molecules with different functions. Because of these features, MOF materials have been considered as an effective precursor to readily prepare a highly heterogeneous catalytically active sites in a uniform fashion for various hybrid electrocatalysts (e.g., metal-nitrogen-carbon materials, carbon-based metal compounds metal/metal oxide-doped carbons). M-N-C structures have been widely reported for their excellent ORR catalytic activity due to the $MN_x$ moieties (M refers to transition metals. x: 2-4). In addition, as a result of synergistic effect between metal and metal sites or metal and porous carbon materials, bimetallic doping of MOF precursors can be an effective strategy to produce bifunctional carbon-based materials and achieve both excellent ORR and OER performance.

### 1.3.2 Metal-free carbon-based catalyst

Carbon materials such as carbon nanotubes (CNTs) and graphene oxide (GO) can be manipulated into various morphologies with high conductivity and high specific surface area. In addition, defect-free carbon is known to be robust in harsh environment in both acidic and alkaline solutions. More importantly, the introduction of heteroatoms (e.g., N, S, O) or defects into the surface of carbon materials can further regulate the partial electronic structure and change the charge density distribution of carbon atoms, leading to the enhancement of catalytic performance. N and B doping has drawn most scientific interest for the design of high-performance metal-free catalysts. Owing to the large electronegativity variations between N/B atoms ($\chi_N$= 3.04, $\chi_B$ = 2.04 in on the Pauling scale) and carbon atoms ($\chi_C$ = 2.55), the process of chemisorption of $O_2$ molecules has been changed, and electron attraction from the anode has been facilitated.[19][20] Dual doping of two types of heteroatoms in a carbon skeleton can provide a synergistic effect that facilitates catalytic activity. Additional boron doping in nitrogen-doped graphene materials could reduce the energy gap of N-doped graphene materials, which benefits oxygen reaction activity.[6][21]

Defects in carbon materials also play imperative roles in ORR and OER kinetics. Defects are often anion/cation vacancies formed during the synthesis process. A difference in the structure of carbon atoms around a defect result in a change of spin or charge distribution

of the $sp^2$ carbon plane. Similar to the impact of heteroatom doping, which causes the charge polarization of carbon atoms to produce strong adsorption to O-containing species during the electrocatalytic process, the introduction of defect regions in a $sp^2$-C matrix also can disrupt conjugation integrity.[14,22,23] Therefore, it is critical to have the capability of controlling the position, amount, and type of defects of carbon-based catalysts to achieve high catalytic activities.

### 1.3.3 Transition metal-based catalysts

Non-precious transition metal (TM; e.g., Co, Ni, Fe, Cu, etc.) based catalysts have received extensive attention due to their variable valence states, promising catalytic activities, abundant resources and environmentally friendly nature. Transition metal oxides are candidates for bifunctional electrocatalysts due to promising intrinsic activities and stabilities. However, their application is restricted due to relatively small surface areas, low electronic conductivities and relatively slow ORR kinetics caused by broad band gaps. Therefore, several strategies can be conducted to address these issues.

First, carbon-based structures such as reduced graphene oxide (rGO) or carbon fibers (CFs), which has good electronic conductivity, can be used to support transition metal oxides and eventually improve the overall catalytic performance. For example, Zhou et al. synthesized ultrathin surface layer of $CoO_x$ onto a Co/N-RGO substrate, which demonstrated high bifunctional ORR/OER catalytic activity.[24] A proper incorporation of Co/N-RGO substrate facilitates electron transfer process and provides more active sites, thus improving the catalytic activity. Second, mixing different type of transition metal oxides could also achieve a high conductivity as the result of the synergistic effect, in which the change of valence state would decrease the activation energies between cations species. Third, surface engineering of the metal oxides materials to create more active sites (oxygen vacancies) is another effective way of improving the conductivity and surface areas. The bandgap or charge distribution of materials may be adjusted by the concentration and distribution of oxygen vacancies. Since the electronic energy profile can be tailored by adjusting the concentration of oxygen defects, the presence of vacancies is considered to increase the kinetics of adsorbing reactants.[25–27]

Other than transition metal oxide, metal chalcogenides, metal phosphides, metal nitrides, metal hydroxides have also been studied as bifunctional ORR/OER electrocatalysts because of their high active site density, high chemical stability, and electron-rich nature of the nonmetal sites[28–31] However, their poor electrical conductivity and aggregation of nanoparticles often limit their catalytic activity and stability. Furthermore, their limited surface area and intrinsic issue of fast degradation mechanism still need further investigation.

## 1.4 Motivation

According to the recent reported research, TM-based catalysts exhibit promises as an alternative to noble-based electrocatalysts for both ORR and OER. However, they often produce non-uniform aggregates of metals, compromising their catalytic activity per mass. Agglomeration lowers the amount of catalytically active sites exposed to reactants, which is not ideal for effective electrocatalysis. Furthermore, this leads to the reduction of heteroatomic interfaces, limiting a higher fraction of the catalyst confined to mono-metallic catalytic abilities. We can create synergistic associations where transition metals are incorporated into heteroatom-doped carbon supports or other types of substrates to prevent the agglomeration of TM-based species and enhance the durability for ORR and OER catalysis.

Binary metal composites and multi-valence species can be formed to allow multiple reactions to be catalyzed. Hence, the development of carbon structures in transition bimetal sites will enhance the utilization and bifunctional electrode content catalytic activity by overcoming the relative low activity of single-TM catalytic systems. The synergetic effects of a multi-metallic species also result in a facile charge transfer between different metals and a reduction in the kinetic energy barrier of electronic structure modulation. Whereas other methods of controlled synthesis have been studied in the past, many have been limited to a narrow set of materials and conditions.

Atomic layer deposition (ALD), an emerging chemical deposition variant, has a unique self-limiting nature during the deposition of a film or a layer of nanoparticles. More importantly, with the utilization of ALD method, which is capable of precise control over

coating thickness and composition, an ultrathin overcoat of metal oxides encapsulating high-surface-area catalyst backbone can be realized. The synergetic effects of a multi-metallic species also result in an easy charge transfer between different metals and a reduction in the kinetic energy barrier of electronic structure modulation. Furthermore, atomically precise synthesis of ALD together with the state of art *in situ* and *ex situ* analysis such as X-ray photoelectron spectroscopy (XPS), X-ray diffraction (XRD) and X-ray adsorption spectroscopy (XAS) provide an effective means of characterizing structural and electronic properties, revealing the active sites during the reaction, and eventually contributing to the effective design of hybrid catalysts.

# CHAPTER 2. Objectives and Introduction

## 2.1 Proposed research

In this thesis, I present three studies that focus on synthesizing multiple transition metal-based hybrid electrocatalysts for ORR and OER with excellent catalytic performance:

1. Synthesis of transition metal-embedded doped-carbon-based catalysts by applying ALD on a MOF-derived structure.
2. Development of 3D CoNi-based layered double hydroxide (LDH) core-shell structure toward high performance of OER catalytic activity.
3. Engineering of ceria assisted 2D layered double hydroxide electrocatalyst with enhanced OER performance.

*The objectives of these studies are:*

1. To develop efficient transition metal-based electrocatalysts through a combination of solvothermal synthesis and vaccum-based chemical deposition.
2. To identify the active sites responsible for the enhanced catalytic activity.
3. To understand the process-property-performance relations for hybrid oxygen electrocatalysts.
4. To propose oxygen reaction pathways occurring in the synthesized electrocatalysts.

### *2.1.1 Trace amount of ceria incorporation by ALD in Co/CoOx-embedded N-doped carbon for efficient bifunctional oxygen electrocatalysis*

Due to its organized high-surface-area layout and uniformly dispersed catalytically active sites within the structure, MOFs have been widely employed as a precursor structure for the synthesis of 3D carbon-based electrocatalysts.[32] The zeolitic imidazolate framework (ZIF) is a class of MOFs where metal cations are bridged by imidazole-based ligands.[33] ZIF-67, which is made of $Co^{2+}$ ions and 2-methylimidazole, can be used as a precursors to synthesis MOF-derived TM-based porous carbon structures by annealing under high

temperature, which could potentially achieve high oxygen electrocatalytic activity as the result of Co-$N_x$ moieties, high graphitization of carbon, and high surface area.[26,34,35] In addition, even after pyrolysis at high temperatures, ZIF-67's distinctive polyhedron structure could be well preserved, offering a highly porous and stable support as a catalyst.[33] Aggregation of organic ligands while pyrolysis at high temperatures is a widely known issue for MOF structures, which will lead to several performance degradation for the catalysts. It is intended to leverage ALD in preventing ZIF-67 from aggregation at high temperatures.

The self-limiting gas-solid reaction of ALD, which allows for atomically precise control to produce high homogeneity in the sizes of Pt nanoparticles supported on carbon, has recently attracted significant interest.[36,37] With a consistent control of size and composition, the approach makes it possible to produce an even angstrom-scale species on a substrate surface, even on highly corrugated, porous three-dimensional materials.[38] ALD could be more easily applied for introducing second metal/metal oxides compared to wet processes or other vapor deposition techniques. Due to the plentiful oxygen vacancies and the readily transition between $Ce^{3+}$ and $Ce^{4+}$ during the catalytic process, cerium oxide has demonstrated strong synergistic effect with other cations for OER performance. Pyrolysis of ZIF structure with thin layer of ALD-treated ceria will create a dual-metal-doped carbon structure, which is beneficial to achieve bifunctional catalytic activity towards both ORR and OER.

### *2.1.2 Facile fabrication of LDH core-shell structure derived from MOF for efficient OER*

Transition metal-based LDHs have been considered as one of the most advanced electrocatalysts toward OER performances due to their unique structural property, flexible structural composition, facile synthesis method, high specific capacitance, and low cost.[39,40] It can be represented by the general formula as $[M_{1-x}^{2+}M_x^{3+}(OH)_2]^{x+}(A^{n-})_{x/n}\cdot mH_2O$, where $M^{2+}$ and $M^{3+}$ represent bivalent (e.g. Co, Ni, Mg, Cu) metal cations, $A^{n-}$ represents for the charge balancing anion, and $mH_2O$ is the interlayer water molecules, respectively. Previous reports have extensively employed a variety of cutting-edge approaches, such as the hydrothermal/solvothermal method, chemical bath deposition,

electrodeposition, microwave-assisted synthesis, and ion-exchange approach, to the synthesis of LDHs, accomplishing a great deal of progress.[3,41,42] However, some of the drawbacks, such as their low intrinsic conductivity and low degree of active site exposure, are limiting future advancements in OER performance.

To address these issues of LDH, an MOF structure can be used as a template for the growth of LDH. Through this approach, one can synthesize hierarchical nanostructures by tuning the interlayer spacing, and introducing more defects, especially oxygen vacancies. In this study, a simple and effective strategy was developed for the preparation high-performance 3D core-shell LDHs electrocatalysts. The hierarchical BDC@CoNi-LDH electrocatalysts with a highly dispersed 3D core (Co-BDC MOF)-shell (CoNi-LDH) structure were prepared via one-step hydrothermal method at 120 °C, using Ni foam as the substrate due to its high porosity and the resultant high active surface area. The higher activity of CoNi-BDC@LDH, compared to Co-BDC@LDH and Ni-BDC@LDH, is ascribed to the richness of BDC and LDH interfaces where the synergistic OER between neighboring Ni and Co sites occurs. At the bimetallic active sites, Co acts as a Lewis acid while Ni serves as the oxygen carrying species, by which its neighboring lattice oxygen is activated to form a Ni-O-O-M bridge for an efficient OER. It is also noted that the BDC-LDH interfaces are highly exposed to the surface in CoNi-BDC@LDH, unlike those in the other two samples as electron microscopy images indicated. For the same reason (i.e., the main active sites residing at the BDC-LDH interface), CoNi-BDC@LDH should exhibit a significantly higher performance than CoNi-LDH. Additionally, CoNi-BDC@LDH has a higher ECSA, and more of catalytically active CoOOH and $Ni(OH)_2$ species, and oxygen vacancies, all of which should further contribute to the activity.

### *2.1.3 Atomically dispersed ceria/titania by ALD on Co-based LDH for enhanced OER*

By leveraging the output from the above two projects, ALD-based LDH structures are subsequently studied. Benefiting from the structure nature of a large amount of OH groups on the surface of LDH, ALD precursor can be easily deposited since the regular oxidants applied during ALD process is $H_2O$. A uniform and wholly covered thin film on LDH surface can be achieved by adjusting the temperature and cycle number of ALD.

For this study, Co- and Ni- based LDHs grown on nickel foam are chosen as the substrate for an additional surface process. Thin layer of $CeO_2/TiO_2$ will be further deposited on the surface of the LDH substrate via ALD to create active sites as the result of synergistic effect between metal atoms and the redox properties of Ti and Ce cations. The as-prepared samples exhibit excellent electrochemical catalytic performance towards OER. The enhanced activity may be attributed to the improved electronic conductivity from the atomic dispersed film and synergistic effect between structural and ALD introduced metal atoms.

# CHAPTER 3. Materials Synthesis and Characterization

## 3.1 Materials synthesis

Nanoparticles are of interest to scientists due to their function as a link between bulk materials and atomic or molecular structures. A bulk material's physical characteristics are independent of its size, but the size-dependent characteristics can be observed within nanomaterials. The large surface area of nanoparticles, which predominates the contributions provided by the modest mass of the materials, is thought to be responsible for their unique and surprising features. Crystalline nanostructures are commonly used as electrocatalytic materials because of their organized structure, which can offer improved electric conductivity and optimized dispersion of catalytically active sites. Additionally, these materials are easier to characterize than amorphous structures, which facilitates further performance optimization. There are several methods for the synthesis of nanoparticles, including chemical route: chemical vapor deposition, epitaxial growth, colloidal dispersion, polymer route, hydrothermal synthesis, inert gas condensation, ion sputtering scattering, microwave, pulse laser ablation, sol-gel, template synthesis, biological synthesis; and physical route: mechanical grinding, high-energy ball milling, mechanical alloying (MA), and reactive milling. This study will be mainly focus on three major synthesis approaches: ultrasound, solvothermal and ALD.

### *3.1.1 Ultrasound method*

The ultrasound method was applied to the first project (Chapter 4) for the synthesis of ZIF-67 octahedral nano structures. The ultrasonic irradiation of a liquid can causes effects over a large range of size scales, from the mixing and heating of the bulk liquid to the concentration of energy in microscopic hot spots intense enough to produce high-energy chemical reactions. The ultrasonic cavitation will be formed once the liquids are irradiated with ultrasonication. Ultrasonic cavitation generates a wide range of physical and chemical effects, including high temperature, pressure, and cooling rate, which creates a special environment for chemical reactions in the face of harsh circumstances. The creation of

nanostructured materials has made use of both the physical and chemical effects of ultrasound. Ultrasound is a fine method for the preparation of nanoparticles with controllable morphologies.[43]

There are a lot of advantages of using ultrasound method for the synthesis of nanomaterials. For example, the whole synthesis process could be conducted under room temperature; the process is very simple since all the solvents and solutions are put together into a container such as beaker, vessel; the reaction rate is very fast, which result in a fast synthesis process. However, it also facing some drawbacks like heat sensitive materials cannot afford acoustic cavitation, and it is difficult to synthesis enough materials at once.

### *3.1.2 Solvothermal method*

The solvothermal method was applied in our second and third project (Chapter 4 & 5) to synthesis the LDH based structure. The process of forming a molecule directly from a solution through a chemical reaction or breakdown of the precursor components is known as a "solvothermal synthesis pathway", and it takes place in a closed system under conditions of high pressure and temperature. The solvothermal approach is based on heating a solvent and its precursors in a closed system to a temperature above the solvent's boiling point. Under extreme circumstances, the precursors are subjected to various effects that result in the production of the desired substance. These influences include a rise in pressure, a high temperature, and the solvent's peculiar behavior. The recommended solvents for this procedure are water, ethanol, methanol, ammonia, carbon dioxide, hydrochloric acid, and hydrofluoric acid.

The overall material synthesis with solvothermal method can be modified by adjusting different parameters including: different solvent, precursor concentration, temperature, reaction time, and pressure. Materials such as metal organic frameworks, layered double hydroxide, microporous crystals, and other hybrid materials are synthesized using this method. The advantage of this method is that most materials can be made soluble in a proper solvent. Moreover, the material size, particle morphology, surface chemistry can be easily controlled though adjustment of the reaction parameters. The disadvantages of

solvothermal synthesis are: 1) The autoclaves are expensive; 2) problems with reaction process safety; 3) It is hard to observing the reaction process.

### *3.1.3 Atomic layer deposition*

Atomic layer deposition (ALD) is a vapor phase technique used as thin film deposition where chemical precursors are sequentially introduced to the surface of a substrate. The surface of a substrate is exposed to alternate precursors during the ALD process; these precursors do not overlap; rather, they are introduced sequentially. The steps of a single cycle deposition process are as follows: 1) expose the precursor to the substrate inside the chamber for a certain amount of time; 2) the chamber is purged with an inert gas to remove the excess precursor and by-products; 3) pulse the second precursor into the chamber; 4) repeat step 2. Depending on the need, the ALD cycle can be run more than once to add extra thin film layers.

ALD relies on self-limiting surface reactions and therefore generally provides very low pin-hole and particle levels, which can benefit a wide range of applications. ALD has been applied to many related electrochemistry applications including batteries, fuel cell, photovoltaics, catalysis and electronic devices. The advantages of ALD are mainly derived from the self-limiting properties. First, conformality of high aspect ratio from ALD deposited films. Second, high quality films grown with ultimate thickness accuracy. Third, low damage and low temperature process. Fourth, a large variety of materials, including oxides, metals, sulfides, and fluorides, can be deposited via ALD. ALD suffers from poor deposition rates even though it has many promising qualities. Most ALD speeds range from 100 to 300 nm/h due to the lengthy cycle periods required for pulsing and purging precursors as well as the layer-by-layer nature of the deposition. [44]

## 3.2 Materials characterization

Studying the morphological and functional characteristics of certain substances is achieved through the application of characterization of materials. The objective enables researchers to know important information about certain materials, such as identifying the

composition of the materials,  oobserving the crystalline morphology of the material. As electrochemical catalysts require the modify and investigate the intrinsic properties of the materials to understand the process-property-performance correlations, it is of vital important to acquire materials characterization analysis. In this section, I will discuss some of the main characterization methods applied on my project.

### *3.2.1 Microscopy techniques*

#### 3.2.1.1 Scanning electron microscopy (SEM)

The scanning electron microscope (SEM) produces a variety of signals at the surface of solid objects using a focussed beam of high-energy electrons. The signal corrected from reflected or knocked-off electrons through electro-sample interactions reveal the morphology, chemical composition, and crystalline structure of the sample. The electron beam may accelerate at voltages as low as 0.1 kV and as high as 30 kV. There are several distinct signal types that are produced at various depths during SEM process, including auger electrons, secondary electrons (SE), characteristic x-rays, backscattered electrons (BSE), and Bremssarahung x-rays. In the majority of applications, measurements are gathered across a chosen region of the sample's surface, and a 2-dimensional picture is created to show spatial changes in these qualities. Three different could be used for observing the samples, including in-lens detector, secondary detector, and backscatter detector. A photo of the prepared SEM sample with the magnification ranging from 1X to approximately 300,000X will appeared on the screen, with the spatial resolution of 10 to 100 nm.

Compared to conventional microscopes, the scanning electron microscope offers numerous benefits. The SEM's broad depth of field makes it possible to focus on more of a specimen at once. Since the SEM has a significantly better resolution, small specimens may be enlarged much more effectively. The SEM gives the researcher far greater control over the level of magnification because it doesn't utilize lenses but rather electromagnets. There are several disadvantages of SEM. Even though it's a great test for chemical analysis and surface typography, certain materials are not suitable for SEM. SEMs can only be used

on solid, inorganic materials that are small enough to fit within a vacuum chamber and can withstand a modest vacuum pressure. Strong insulator samples must be coated with gold or carbon prior to testing. Moreover, the X-rays generated during the procedure as well as the electrons that are backscattered from the sample are the sources of the radiation safety issues while using SEM.

#### 3.2.1.2 Transmission electron microscopy (TEM)

Transmission electron microscopy (TEM) is another useful technique of characterization of nanomaterials. TEM offers effective methods for comprehending a wide range of information about materials with extremely high spatial resolution, such as morphology, size distribution, crystal structure, strain, defects, chemical information down to the atomic level, and so on. A high energy beam of electrons that pass through a very thin sample while the electrons either scatter or hit a fluorescent screen at the bottom of the microscopy, thus generate a highly-magnified image. The extremely short wavelength of the transmitted electrons allows TEM to achieve resolution levels that are unmatched. The resolution of TEM is simply constrained by the wavelength of each individual electron and the caliber of the electron optics, as opposed to scanning electron microscopy (SEM), which collects the net intensity of secondary electrons at each point of the scan. As a result, transmission electron microscopes may constantly acquire pictures with a resolution of less than an atom. There are many techniques used in TEM to acquire different information of the samples, including selected-area electron diffraction (SAED), bright filed (BF) TEM, dark field (DF) TEM, high-resolution TEM (HRTEM), high angle annually dark field (HAASF)-STEM imagine, electron energy loss spectroscopy (EELS), energy-filtered TEM (EFTEM) and 3D electron tomography, etc.

TEM are very powerful in material analysis with various advantages: 1) TEM provide information on element and materials crystalline structure. 2) TEM offers the most powerful magnification, much higher than that of SEM. 3) TEM provide excellent resolution of the structure information of the specimens. Some cons of TEM include: 1) As same as SEM, TEM also requires that specimens be put inside a vacuum chamber. 2)

Tedious and time-consuming sample preparation. 3) Requirement of transparent and tolerate sample. 4) Black and white images.

#### 3.2.1.3 Energy dispersive spectroscopy (EDS)

Energy Dispersive Spectroscopy (EDS) is mostly used for identifying and quantifying elemental composition of sample within an area of a micron or less. EDS usually equipped into either SEM or TEM which has an energy source. By ejecting a core-shell electron, a sample that has been activated by an energy source releases part of the energy that has been absorbed. The difference in energy is subsequently released as an X-ray with a distinctive spectrum depending on its parent atom when a higher energy outer-shell electron moves in to take its place.

Strengths of EDS include rapid elemental analysis of small features; elemental coverage for almost all elements; easy to use; semi-quantitative mode to determine chemical composition by peak-height ratio relative to standard. The main drawbacks are EDS is not a particularly sensitive technique; it does not work for low atomic number elements; and it mainly works for the detection of element on surface layers rather than the bulk of the samples.

#### 3.2.1.4 X-ray diffraction (XRD)

X-ray diffraction is an important characterization technique used for identification of the structural information on unit cell dimensions such as interatomic distances, bond angles, crystallinity, unit cell lattice parameter, crystallite size, etc. Constructive interference between monochromatic X-rays and a crystalline sample is the foundation of X-ray diffraction. A straightforward concept known as Bragg's law could be utilized to comprehend the requirements for diffraction when x-rays interact with crystal lattice. The Bragg's law is expressed as $n\lambda = 2d\sin\theta$, where $\lambda$ is the wavelength of the electromagnetic radiation, $\theta$ is the diffraction angle between incident X-ray beam and scattering plane, d is the lattice spacing in a crystalline sample, and n is integer. By scanning the sample through a range of $2\theta$ angles, the diffracted lattice will be detected as sharp peaks if the atoms are arranged in a periodic in the material. The International Centre for Diffraction Data (ICDD)

database can be further used as a reference to determine the details of material structures once the data has been collected.

XRD is a powerful and quick technique for identifying the structure information of a material, even if the material is unknow. The sample preparation process is quite straightforward and simple. Moreover, it will produce clear, unambiguous results that can be analyzed directly. However, the standard reference database needs to be authorized and the sample needs to be homogeneous and in a single phase if the material is unknow. The peak overlay problem would also occur.

#### 3.2.1.5 X-ray Photoelectron Spectroscopy (XPS)

XPS is a surface technique used for material characterization, especially for the elemental analysis including chemical states, valence state, element composition, etc. The specimen's surface is penetrated by X-rays to a depth of a few micrometres, but only electrons close to the surface can be released without losing energy from collisions with other atoms. The binding energy can be determined according to the equation: $E_{binding} = E_{photon} - E_{kinetic} + \Phi$; where $E_{binding}$ is the energy of an electron attracted to a nucleus, $\Phi$ is the spectrometer work function, photon energy is the x-ray energy, and the kinetic energy is the energy of the ejected electrons from the sample. Different element will be identified by scanning the kinetic energy within the range of 0 eV to the incident x-ray energy. The corresponding peak for a certain element could be further deconvoluted into subpeaks to reveal the bonding environment or valence state. In addition, XPS could also use for determining the chemical shift since the binding energy doesn't only depend on the shell of the electron but also depends on the atom next to it.

XPS is an efficient testing technique which is effective for identifying all elements except for H and He. The straightforward quantitative analysis from XPS data will further provide information about the chemical state and oxidation state between different samples. Furthermore, the analysis process is simple. Nevertheless, it could only characterize the surface exposed element and it requires the sample to be solid and vacuum compatible. XPS spectra also requires a long time to obtain with a pretty low scan rate.

## 3.3 Electrochemical Measurements

### *3.3.1 Cyclic voltammetry*

Cyclic voltammetry (CV) is the most widely used electrochemical analysis technique for acquiring the current response of a redox active solution to a cycled potential sweep, providing the information of the redox process and the kinetics of electronic transfer reactions. A working electrode, reference electrode, and counter electrode comprise three electrode system for use in cyclic voltammetry. The potential between the working and reference electrodes is then linearly swept using a potentiostat until it hits a predetermined limit, at which time it is swept back in the opposite way. Depending on the direction of the sweeping potential, the chemical either loses an electron (oxidation) or acquires an electron (reduction) during a scan.

### *3.3.2 Linear sweep voltammetry*

Linear sweep voltammetry (LSV) is similar to CV measurement, which requires only one single way linear sweep between two potential windows rather than cycling over the potential range. This measurement involves linearly sweeping the voltage supplied to a three-electrode electrochemical cell over time. The sweep rate should be slow enough to collect reliable readings but not being so slow as to cause the current to start to decline as the redox reaction's available reactants are being used. As the voltage is swept, the current in the electrochemical cell is measured. The current vs. voltage data is then shown on a graph. In order to diagnose the thermodynamic reversibility of a material, linear sweep voltammetry allows the analysis of a number of important characteristics, including the peak current, the potential at the peak current, and the potential at half the peak current just before the peak is attained.

### *3.3.3 Tafel plot*

A Tafel plot is a visual representation of the connection between an electrode potential for a particular metal and the current produced in an electrochemical cell. Typically, Tafel

plot is generated based on the LSV data using Tafel equation, which reveals the relation in electrochemical kinetics between electrochemical reaction and overpotential. The Tafel equation is simplified from the Butler-Volmer equation and can be represented as $\eta = A*\log(j/j_0)$, where $\eta$ is the overpotential, A is the Tafel slope, j is the current density and $j_0$ is the exchange current density. The Tafel slope is an indicator of the kinetics of the electrochemical reaction while a lower slope indicates faster kinetics.

### *3.3.4 Electrochemical impedance spectroscopy*

Electrochemical Impedance Spectroscopy (EIS) is a frequency domain measurement made by applying a voltage to a system. It is a very sensitive characterisation method to determine the electrical response of chemical systems. EIS is a technique where a potentiostate applies a sinusoidal potential or a sinusoidal current to an electrochemical system, and we measure the corresponding sinusoidal current or a sinusoidal potential from the system. A complete EIS experiment will consist of applying a sinusoidal potential cantered around a potential set point at multiple frequencies. And we are measuring the output sinusoidal current at all these different frequencies to create an EIS spectrum. The interactions include charge transfer, mass transfer and diffusion between the bulk electrolyte and the electrode surface in a conventional electrochemical system can be described by an electrical circuit made up of capacitors or resistances interconnected in parallel or series to create an equivalent circuit. Thus, the EIS could be used to explore mass-transfer, charge-transfer, and diffusion processes.

# CHAPTER 4. Trace Amount of Ceria Incorporation by ALD in $Co/Co_x$-embedded N-doped Carbon for Efficient Bifunctional Oxygen Electrocatalysis

## 4.1 Introduction

The kinetics of oxygen reduction reaction (ORR) and oxygen evolution reaction (OER) is critical to the performance of fuel cells [45], metal-air batteries [46] and water electrolysis [47]. Noble metals have been regarded as the standard electrocatalysts for these reactions, but their high cost, lack of stability and scarcity prevent them from being widely used in commercial applications [48]. Moreover, noble metals work for either ORR (Pt) or OER (Ru and Ir), not for both, thus not applicable for metal-air batteries or unified regenerative fuel cells. The conditions for ORR and OER are very different, especially in terms of the electrical potential of the reactions, making the development of efficient bifunctional oxygen electrocatalysts with low cost and high durability very challenging [11].

As a promising class, transition metal (TM)/transition metal oxide (TMO) nanoparticles (NP) have been extensively explored for bifunctional ORR/OER catalysis due to their advantageous attributes such as low cost, abundance and decent intrinsic catalytic activity and stability [49,50]. These NPs are often embedded in porous 3D carbon structures to provide electronic pathways, suppress their agglomerations and maximally expose them to reactants [51,52]. These carbon structures can be doped with heteroatoms (most notably, nitrogen) to further enhance electrocatalytic activity by tuning localized electronic landscape [52,53]. Optimized NP/carbon hybrids render high oxygen electrocatalytic activities, which is often ascribed to a synergistic effect among TM, N and C as well as the intrinsic catalytic capabilities of each component [51,54]. While the exact origin of the synergy has not been clearly understood, it is largely accepted that the strong bonding between the TM and N-doped carbon, driven by the high affinity of N to the TM, promotes interfacial electron transfer between the active site and oxygen intermediates and enhances electrocatalytic activities [55]. However, single TM/TMO-embedded N-C systems barely provide a catalytic activity and stability sufficient for wide commercial use, leaving room

for further engineering [56,57]. The introduction of a second metal/metal oxide into a single TM/TMO-based hybrid can induce additional catalytically active sites such as metal-N-C moieties [58,59], oxygen vacancies [60,61], redox couples [62,63], and new crystalline phases of high activity [58] and/or tune electronic structure to further enhance catalytic activity [57,64].

Recently, metal organic frameworks (MOFs) have been widely used as a precursor structure for the synthesis of 3D carbon-based electrocatalysts due to their ordered high-surface-area geometry and facile dispersion of catalytically active sites in the structure [32]. The zeolitic imidazolate framework (ZIF) is a class of MOFs where metal cations are bridged by imidazole-based ligands [33]. In particular, the ZIF-67, which is made of $Co^{2+}$ ions and 2-methylimidazole, can be used as a precursor to synthesize Co-containing N-doped porous 3D carbon structures via pyrolysis, which renders high oxygen electrocatalytic activity due to its abundant N species, Co-$N_x$ moieties, high graphitization degree and high surface area [26,34,35]. In addition, the polyhedron structure of ZIF-67 can be maintained even after pyrolysis at elevated temperatures, offering a highly porous and stable support for further enhancement of catalytic activity [33].

In this study, we demonstrate a facile synthesis of ZIF-67-derived Co/$CoO_x$-embedded porous N-doped carbon (N–C) structure onto which a trace amount of $CeO_x$ species is uniformly introduced for an efficient bifunctional oxygen catalysis. To maximize possible synergistic effects between Co-based species and $CeO_x$, we aim to make the Co/$CoO_x$–$CeO_x$–reactant triple junction maximized by introducing ceria in a highly dispersed manner by leveraging the characteristics of atomic layer deposition (ALD). ALD is an emerging low-temperature material deposition scheme that relies on sequential self-limiting reactions occurring between gaseous precursor and substrate surface in a discrete fashion [36,37]. This unique process enables to form angstrom-scale species on a substrate surface uniformly even on highly corrugated, porous high-aspect-ratio 3D structures with a reliable control of size and composition [38], making ALD advantageous in introducing second metal/metal oxides compared to wet processes or other vapor deposition techniques. The resultant hybrid catalyst prepared in an optimized ALD and pyrolysis condition (Co/NC@Ce15-700) shows a uniform yet porous structure inheriting the rhombic dodecahedral morphology of ZIF-67 and demonstrates an excellent bifunctional ORR and

OER performance and durability in alkaline media. A discussion based on a series of *quasi-operando* X-ray photoelectron spectroscopy (XPS) and X-ray diffraction (XRD)-based analyses is also provided to better understand the higher activity for ORR and OER in this system.

## 4.2 Experimental section

### *4.2.1 Synthesis of ZIF-67*

$Co(NO_3)_2 \cdot H_2O$ (7 g; 99.8%, Sigma Aldrich) was dissolved in a mixed solution of 80 mL ethanol and 80 mL methanol. 2-methylimidazole (8 g; $C_4H_6N_2$, 99.0%, Sigma Aldrich) was dissolved in another mixture solution of 80 mL ethanol and 80 mL methanol. The latter solution was rapidly added to the former solution and stirred for 10 s, then the final solution was kept at room temperature for 24 h. The resulting purple precipitates collected by centrifugation were washed with ethanol and DI water for 3 times, and finally dried at 80 °C for 12 h to form ZIF-67.

### *4.2.2 Synthesis of ZIF-CeX series*

ALD was performed to incorporate $CeO_x$ species in the ZIF-67. For ALD, as-prepared ZIF-67 was evenly distributed in a handmade aluminum foil boat, which was covered with a copper mesh and placed in a customized thermal ALD chamber. $CeO_2$ ALD was performed at 250 °C using $Ce(iPrCp)_3$ (Strem Chemicals) and distilled $H_2O$ as the cerium precursor and co-reactant, respectively. The cerium precursor was heated to 145 °C, and the precursor and co-reactant were carried by $N_2$ flow. A complete ALD cycle is comprised of $H_2O$ pulsing for 0.4 s and cerium pulsing for 2.5 s. The ZIF-CeX (X: number of ALD cycles) were obtained by 5, 15 and 25 ALD cycles, each being named as ZIF-Ce5, ZIF-Ce15 and ZIF-Ce25, respectively. The nominal growth rate of ALD ceria using the $Ce(iPrCp)_3$-$H_2O$ chemistry in our ALD setup is expected to be roughly 0.2 – 0.5 Å per cycle although the rate is highly dependent upon the surface chemistry of substrate [65].

### *4.2.3 Preparation of Co/NC@CeX-Y and Co/NC-Y series*

The as-prepared ZIF-CeX samples were placed in a ceramic boat and heated up to a target temperature (700, 800 or 900 °C) in a tube furnace at 4 °C $min^{-1}$ and annealed at the target temperature for 3 h under a continuous $N_2$ flow. The black powers obtained after 700 °C pyrolysis are denoted as Co/NC@Ce5-700, Co/NC@Ce15-700 and Co/NC@Ce25-700, respectively. ZIF-Ce15 composite was pyrolyzed at two additional temperatures (800 °C and 900 °C) to obtain Co/NC@Ce15-800 and Co/NC@Ce15-900. On the other hand, the sample pyrolyzed at 700 °C without performing an ALD process are named Co/NC-700.

### *4.2.4 Physical characterization*

The morphology and microstructure were characterized by scanning electron microscopy (SEM; Zeiss Gemini SEM 500, 3 kV) and transmission electron microscopy (TEM; Philips CM300 FEG system 200 kV). The energy dispersive X-ray spectroscopy (EDS) (Oxford X-max mm2 SDD 127eV at 50k cps) was performed on a Talos F200C G2 TEM system; X-FEG electron source, 0.18 lattice resolution and 0.30 nm point to point resolution was set to the tip. XRD patterns were recorded using PANalytical X'Pert PRO with Co Kα radiation (λ = 1.78897 Å) at the step size of 0.02° and scan rate of 0.04° $s^{-1}$, and the resulting data was converted to Co Kα radiation (λ = 1.5418 Å) based spectra for facile comparison with other reports. Fourier transform infrared spectroscopy (FT-IR) were recorded on a Nicolet 380 FT-IR Spectrometer with the wave numbers from 400 to 4000 $cm^{-1}$ by dispersing samples onto a crystal attenuated total reflectance (ATR) accessory. Raman spectra were obtained on an iXR Raman spectrometer (Thermo Scientific). XPS was performed on a PHI Quantum 2000 system using a focused, monochromatic Al Kα X-ray (1486.6 eV) source for excitation and a spherical section analyzer (200 μm diameter X-ray beam incident to the surface normal; detector set at 45°). Brauner Emmett Teller (BET) nitrogen adsorption tests were performed on a Gemini VII 2390a. Degassing was done by FlowPrep 060 for 2 h with $N_2$ at 250 °C.

### *4.2.5 Electrochemical Characterization*

The ORR and OER characterization was performed in a standard three-electrode glass cell by a potentiostat (SP-200, Bio-Logic SAS) at room temperature. Glassy carbon

electrodes (GCE) with the as-prepared products were used as the working electrode while a graphite rod and an Ag/AgCl (3.5 M KCl) electrode were used as the counter and reference electrodes, respectively. All potentials were expressed with respect to reversible hydrogen electrode ($E_{RHE} = E_{Ag/AgCl} + 0.95$ V). The catalyst ink was prepared by dissolving 5 mg of catalyst into 200 μL of ethanol, 250 μL of DI water and 50 μL of 5 wt% Nafion (Nafion D-521, Alfa Aesar), followed by a sonication for 40 min. 5 μL of the mixture was dropped onto a GCE (4 mm diameter) and rotated until fully dried. $N_2$ or $O_2$ flow was fed into the electrolyte (0.1 M KOH for ORR; 1 M KOH for OER) for > 30 min to have the solution saturated with each gas before testing. Linear sweep voltammetry (LSV) tests were performed with a scan rate of 1 mV $s^{-1}$ from 0.5 V to 1 V (vs RHE) for ORR and from 1.2 V to 1.8 V for OER under various rotation speeds ranging from 400 rpm to 2,000 rpm. The cyclic stability was additionally tested for 2,000 cycles between 0.1 V and 1.0 V for ORR in $O_2$ and between 1.5 to 1.85 V for OER in $N_2$, both at 100 mV $s^{-1}$ and 1600 rpm rotation. Quasi-operando XPS and XRD electrochemical operation were carried out under different electrochemical potential for 10 min to obtain the surface chemical states and structural information of the samples. For the sample preparation for quasi-operando measurements, the catalysts (5 mg) were first dissolved into 500 μL ethanol and DI water, followed by a sonication for 40 min. 10 μL of the prepared solution was dropped onto a carbon fiber paper (AvCarb P75T, FuelCell Store) and dried under 60 °C. 0.1 M/1 M KOH electrolyte was used for ORR/OER while $O_2$ flow was fed during the operation. Before all the LSV tests, the electrodes were cycled at 100 mV $s^{-1}$ until reproducible cyclic voltammograms (CVs) were obtained. LSV measurement was then performed and stayed under 0.5 V, 0.85 V, 1.4 V and 1.6 V for 10 min. The electrode was dried and used directly for the XPS and XRD analysis. To assess the catalytic activity and stability of our new hybrid catalyst, a Zn-air battery test was performed by using a polished Zn plate as the anode, as-prepared catalyst as the air electrode (cathode) and 6 M KOH as the electrolyte, respectively. For the preparation of a cathode, the catalysts (5 mg) and 50 μL Nafion were dispersed into 450 μL ethanol by sonication, and the resulting ink was drop-casted onto a hydrophobic carbon paper (5 $cm^{-2}$) to obtain the mass loading of 1 mg $cm^{-2}$ and dried at 60 °C for 2 h.

For a comparison, a benchmark air electrode was additionally prepared in the same procedure by using a mixture of Pt/C (2.5 mg) and $IrO_2$ (2.5 mg) instead of 5 mg catalyst.

### *4.2.6 Quantification of particle size from XRD*

The size of nanoparticles was calculated from the following Debye-Scherrer Equation:[66]

$$B(2\theta) = \frac{K\lambda}{Lcos\theta}$$

where $L$ is the average size of the ordered crystalline domains, $K$ the dimensionless shape factor (0.9), $\lambda$ the wavelength of the X-ray and $B$ the full width at half maximum (FWHM).

### *4.2.7 Deconvolution of XPS spectra*

***Ce 3d***: By taking the method detailed by Maslakov et al.[67] the mole fraction of $Ce^{3+}$ and $Ce^{4+}$ were quantified from Ce $3d_{5/2}$ peaks using the following equation.

$$f(Ce^{3+}) = \frac{1-a_0 \cdot \frac{3}{2} \cdot \frac{I(u''')}{I(v)+I(v')+I(v'')}}{1-\frac{3}{2} \cdot \frac{I(u''')}{I(v)+I(v')+I(v'')}} \text{ and } f(Ce^{4+}) = 1 - f(Ce^{3+})$$

$$\text{where } a_0 = \frac{I(v)+I(v'')}{\frac{3}{2}I(u''')}.$$

$I$ value (unit: a.u.) are obtained by taking the area under each spectrum.

***O 1s***: $I$ values (unit: a.u.) are obtained by taking the area under each spectrum and tabulated below. The fraction of each bonding was quantified simply by:

$$f(\text{O-Ce}^{3+}) = \frac{I(O-Ce^{3+})}{I(O-Ce^{4+})+I(O-Ce^{3+})} \text{ and } f(\text{O-Ce}^{4+}) = 1 - f(\text{O-Ce}^{4+})$$

### *4.2.8 Calculation of mass activity and turnover frequency (TOF)*

Mass activity ($j_m$, A $g^{-1}$) and turnover frequency for both ORR and OER are calculated at an overpotential of $\eta$ = 350 mV. The mass activity was calculated from the catalyst loading (0.40 mg $cm^{-2}$):

$$j_m = j/m$$

And TOF is calculated by the following equation:

$$TOF = (j \times A)/(4 \times F \times n)$$

where $j$ is the measured current density at the overpotential of 350 mV, $F$ is Faraday's constant (96485 C/mol), $n$ is the number of moles of the active metal atoms (2.26 x$10^{-7}$ mol) drop-cast on the electrode (In our case, the active metal atoms are considered as Co only since the amount of Ce is negligible compared to Co).

### *4.2.9 Quantification of electron transfer number*

The electron transfer number ($n$) was calculated using Koutecky-Levich equation:

$$\frac{1}{J} = \frac{1}{J_d} + \frac{1}{J_k} = \frac{1}{B\omega^{\frac{1}{2}}} + \frac{1}{J_k}$$

$$B = 0.2nFC_0(D_0)^{2/3}\nu^{-1/6}$$

$$J_{\mathrm{k}} = nFk\mathrm{C}_0$$

where $J$ is the measured current density; $J_k$ and $J_d$ are the kinetic and diffusion limiting current density; ω is the electrode rotating rate; $n$ is the number of electrons transferred during ORR process; $F$ is the Faraday constant ($F$ = 96485 C $mol^{-1}$); $C_0$ is the bulk concentration of $O_2$ (1.2 × $10^{-6}$ $cm^2$ $s^{-1}$ in 0.1 M KOH); $D_0$ is the diffusion coefficient of $O_2$ ($D_0$ = 1.9 × $10^{-5}$ $cm^2$ $s^{-1}$ in 0.1 M KOH); $v$ is the kinetic viscosity (0.01 $cm^2$ $s^{-1}$ in 0.1 M KOH); $k$ is the electron transfer constant.

Rotating ring disk electrode (RRDE) measurement was also conducted in 0.1 M KOH solution with a scan rate of 1 mV $s^{-1}$ at different rotation speeds. The electron transfer number ($n$) and hydrogen peroxide yield ($H_2O_2$ %) were calculated by the following equations:[68]

$$\mathrm{n} = \frac{4I_D}{I_D + (I_R/N)}$$

$$H_2O_2\% = 200 \times \frac{I_R/N}{\frac{I_R}{N} + I_D}$$

where $I_D$ is the disk current, $I_R$ is the ring current, and $N$ is the current collection efficiency of Pt ring ($N = 0.28$).

## 4.3 Results

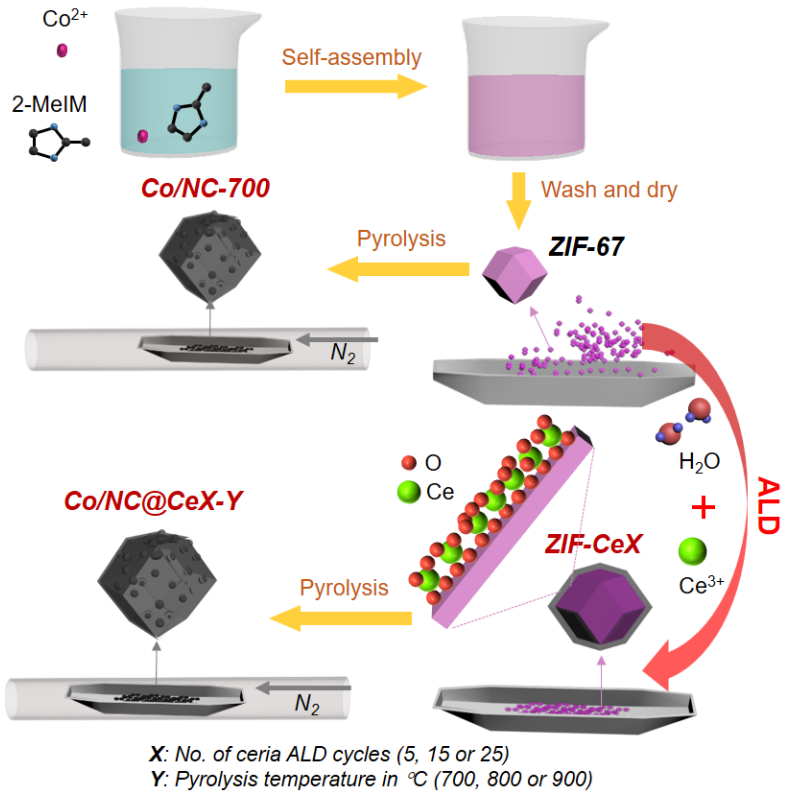


**Scheme 4.1** A schematic illustration of sample preparation process.

Four samples pyrolyzed at 700 °C are mainly discussed here: Co/NC-700 and Co/NC@CeX-700 series (X: 5, 15 and 25, representing the number of ceria ALD cycles). A simplified schematic diagram of their synthesis process is illustrated in Scheme 1.

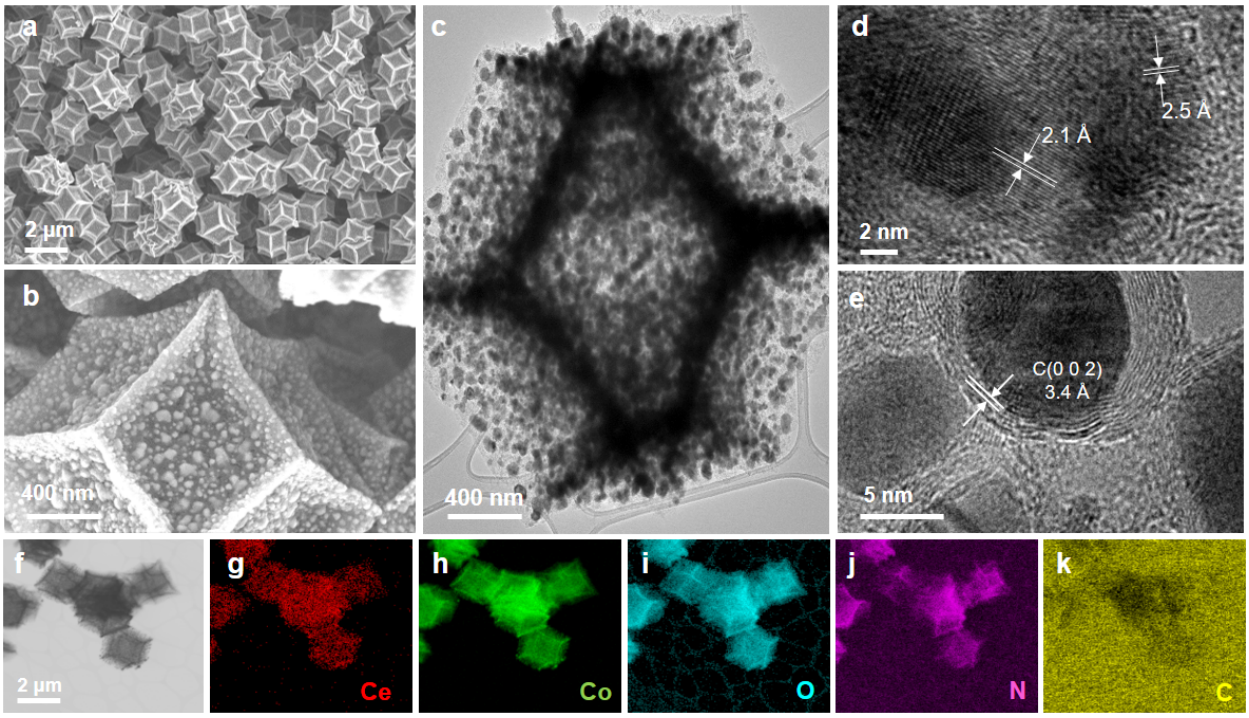


**Figure 4.1** Micrographs of Co/NC@Ce15-700: SEM (a,b), TEM (c) and HRTEM images (d,e). A low magnification TEM image (f) and corresponding EDS elemental mapping (g-k).

SEM micrographs show that the pyrolyzed samples inherit the typical morphology of rhombic dodecahedral structure of ZIF-67 (Fig. 4.1a and Fig. 4.2). The pyrolysis makes the facets of dodecahedral structure deformed into a concave shape, which becomes more significant with larger number of ALD cycles. The sample with 25 ALD cycles (Co/NC@Ce25-700) eventually exhibits a significant morphological deformation (Fig. 4.1d), which is ascribed to a significant blockage of Co species and organic ligands by ceria ALD performed before pyrolysis. It is also noted that the size of the $Co/CoO_x$ NPs appearing on the faces of dodecahedrons is also dependent

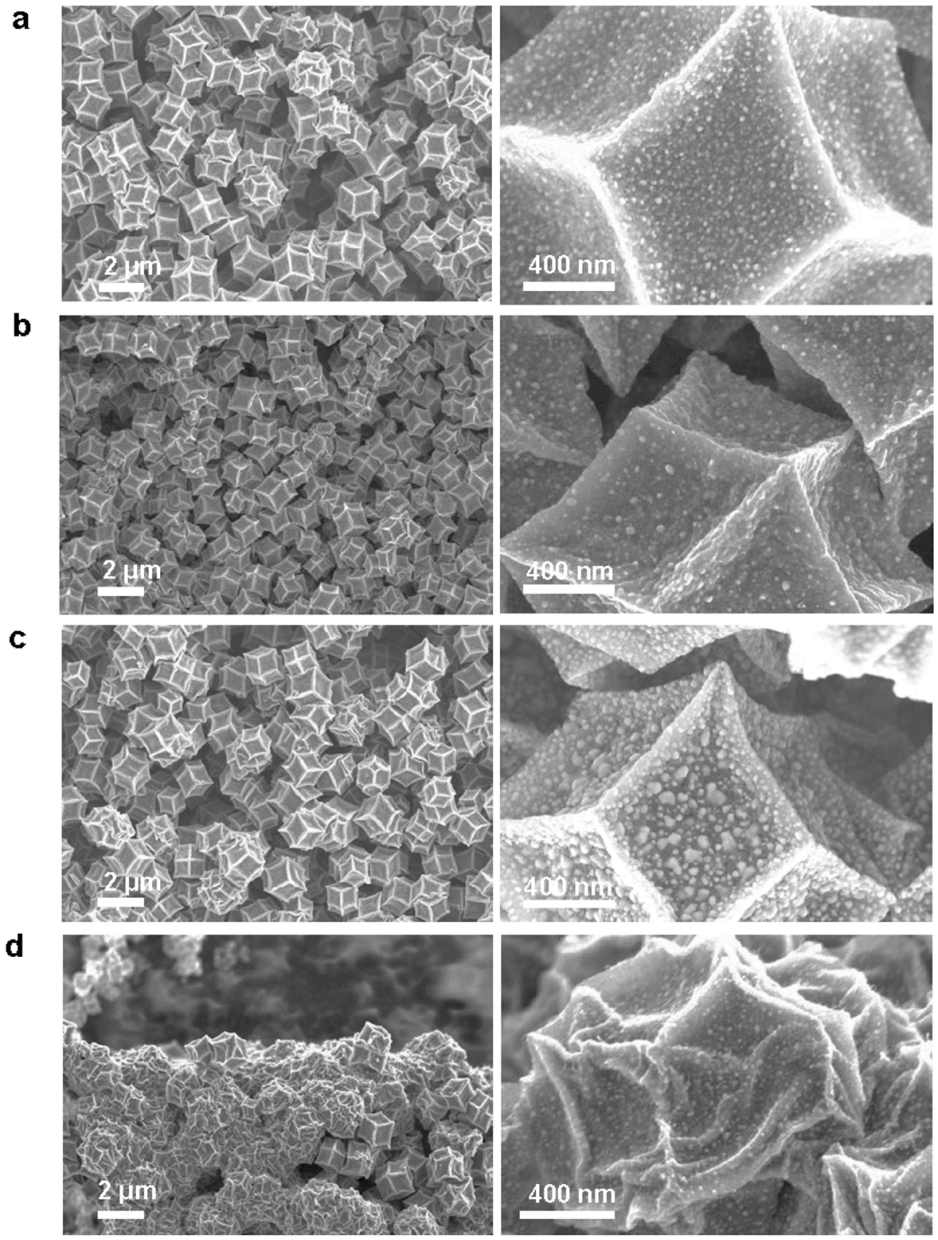


**Figure 4.2** SEM images of (a) Co/NC-700, (b) Co/NC@Ce5-700, (c) Co/NC@Ce15-700, and (d) Co/NC@Ce25-700.

on the ceria ALD cycles; the NPs on the Co/NC@Ce15-700 are larger (average size: ca. 58 nm as determined from SEM micrographs shown in Fig. 4.1b and Fig. 4.3) than those on Co/NC-700 (24 nm) and Co/NC@Ce5-700 (27 nm) and Co/NC@Ce25-700 (30 nm). In

addition, unlike the other samples, Co/NC@Ce15-700 shows distinct pores of several nanometers in diameter formed

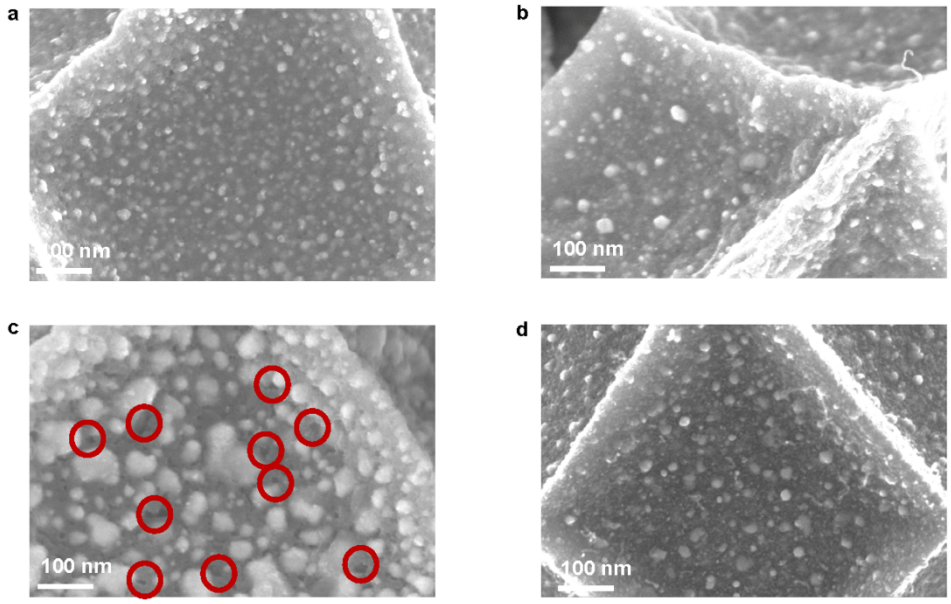


**Figure 4.3** High magnification SEM images of (a) Co/NC-700, (b) Co/NC@Ce5-700, (c) Co/NC@Ce15-700, and (d) Co/NC@Ce25-700. The red circles in (c) indicate distinct nanoscale pores.

randomly on the surface of polyhedrons (see Fig. 4.3c), which may enable the access of reactants to a wider surface of the catalyst [23]. The TEM image in Fig. 4.1c shows that Co/NC@Ce15-700 has a polyhedron crystal structure in which NPs of ca. 58 nm on average are uniformly embedded. High-resolution TEM image (Fig. 4.1d) shows lattice fringes of the NPs encapsulated inside carbon structure revealing Co(111) and $Co_3O_4$(311) planes with *d*-spacing of ca. 2.1 Å and 2.5 Å, respectively while only Co(111) planes are visible in Co/NC@Ce5-700 and Co/NC@Ce25-700 (Fig. 4.4).

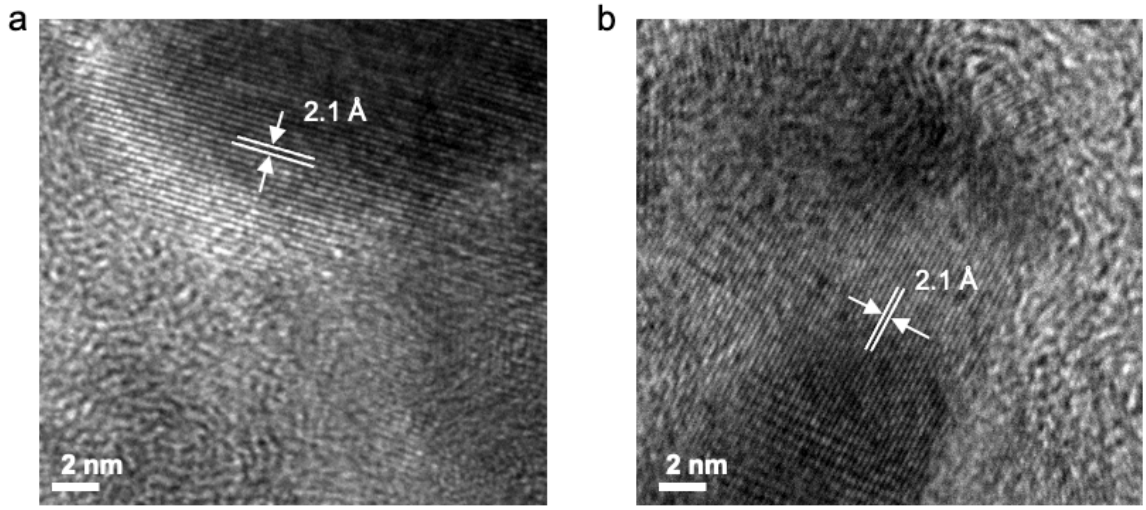


**Figure 4.4** HRTEM images of Co/NC@Ce5-700 (a) and Co/NC@Ce25-700 (b) showing the lattice fringes of Co(111).

Graphitized carbon (002) planes with spacing of ca. 3.4 Å encapsulating the Co NPs are also observed (Fig. 4.1e). The EDS elemental mapping of the Co/NC@Ce15-700 sample (Figs. 1g-k; a spectrum in Fig. 4.5) verifies that Co, Ce, C, N and O species are uniformly dispersed throughout the polyhedral structure. It is also stressed that the ALD process successfully achieves a homogeneous and dense distribution of ceria throughout the ZIF-67 structure.

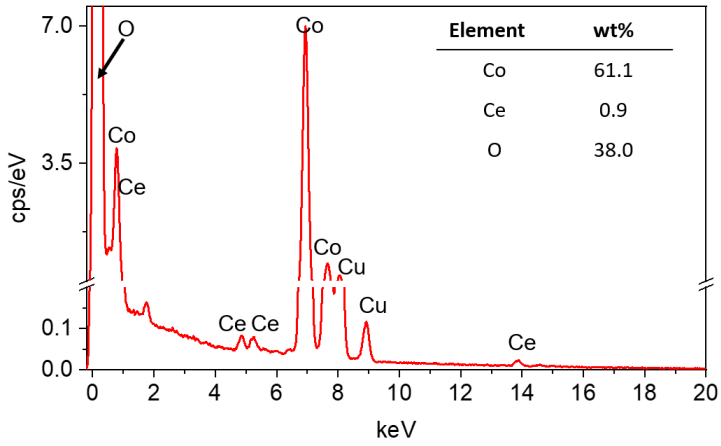


**Figure 4.5** TEM-EDS spectrum of Co/NC@Ce15-700. Ce/Co weight ratio of 0.9:61.1 corresponds to 0.0062:1 in atomic ratio.

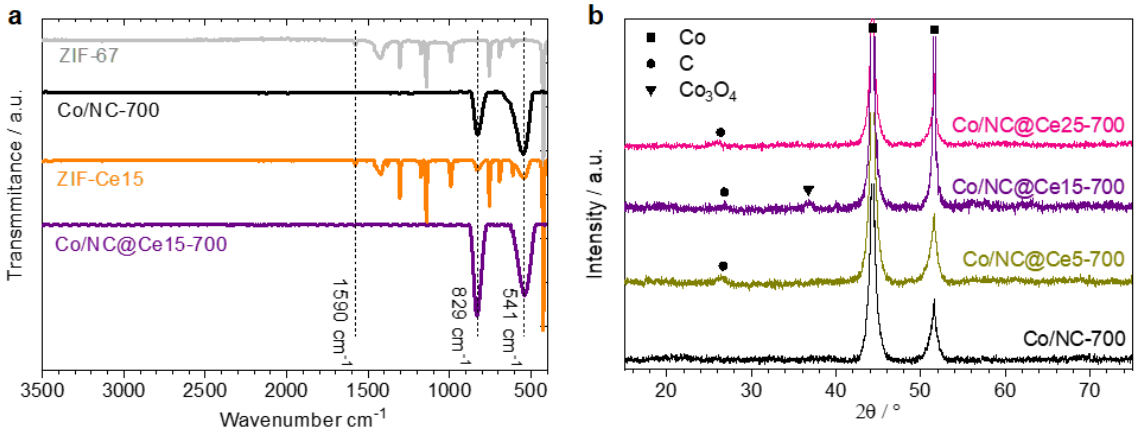


**Figure 4.6** (a) FT-IR spectra and (b) XRD patterns of hybrid samples before/after pyrolysis process

In the FT-IR spectra (Fig. 4.6a), the samples before pyrolysis (ZIF-67 and ZIF-Ce15) show stretching vibrations typical of ZIF-67 structures including Co-N stretching (420 $cm^{-1}$), C=N stretching (1590 $cm^{-1}$) and out-of-plane bending (600 – 800 $cm^{-1}$) and in-plane bending (1000 – 1350 $cm^{-1}$) of the imidazole ring [69–71]. There are newly emerged broad peaks at around 541 and 829 $cm^{-1}$ for ZIF-Ce15 sample, which can be attribute to the Ce-O stretching mode, confirms the existence of $CeO_2$ [72–74]. After pyrolysis, the greatly increased intensity at around 829 $cm^{-1}$ could be related with the cerium-peroxo species ($Ce-O_2^{2-}$ , characteristic region between 883 $cm^{-1}$ – 831 $cm^{-1}$ ) respectively.

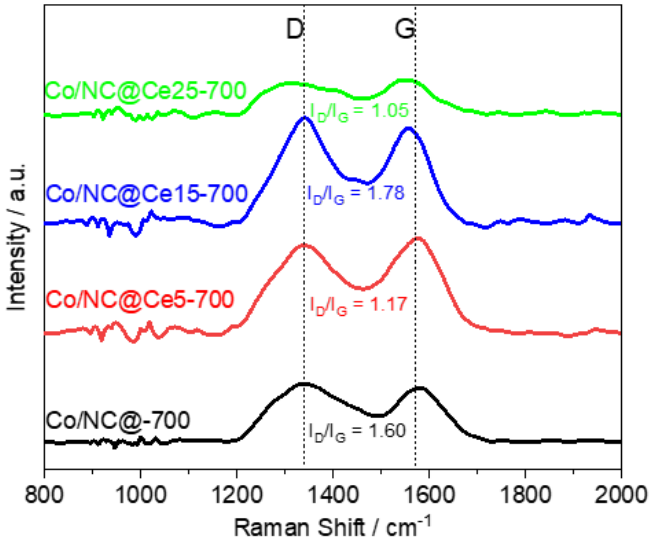


**Figure 4.7** Raman spectra for Co/NC-700 and Co/NC@CeX-700 series.

Raman spectra in Fig. 4.7 indicate similar carbon structures for all samples with dominant D-band (1340 $cm^{-1}$) for disordered carbons and G-band (1580 $cm^{-1}$) for $sp^2$ hybridized carbon. Particularly, Co/NC@Ce15-700 exhibits a relative higher $I_D/I_G$ ratio of 1.78, suggesting more defects site were created with a proper Ce doping. From the XRD spectra in Fig. 4.6b, all four samples show strong peaks corresponding to metallic Co, well aligned with the HRTEM image in Fig. 4.1d; the peaks at 44.3° and 51.8° are assigned to the (111) and (200) planes, respectively (ICDD no. 00-015-0806). The average size of Co NPs in Co/NC@Ce15-700 (51.0 nm) quantified by the Scherrer equation[66] is larger than those of Co/NC-700 (19.1), Co/NC@Ce5-700 (30.6) and Co/NC@Ce25-700 (43.7), consistent with the SEM images in Fig. 4.2. In addition to the cubic Co peaks, Co/NC@Ce15-700 exhibits small peaks at 36.6° and 42.5° corresponding to spinel $Co_3O_4$ (311) plane (ICDD no. 01-080-1543), further supporting the HRTEM result (Fig. 4.1d). The average $Co_3O_4$ NP size determined by the Scherrer equation is 5.2 nm. Unlike Co/NC@Ce15-700, both Co/NC@Ce5-700 and Co/NC@Co25-700 did not show the $Co_3O_4$ diffraction peaks (Fig. 4.6b). As for Co/NC@Ce5-700, the ALD-deposited ceria may not be enough to oxidize Co and form a detectable amount of $Co_3O_4$. The absence of $Co_3O_4$ peak from Co/NC@Ce25-700, on the other hand, is tentatively ascribed to the

amorphization of $CoO_x$ as a Ce doping can induce a significant variation in the crystal structure of $CoO_x$ from crystalline to amorphous one [75]. In addition to the Co and $Co_3O_4$ phases, all three samples in the Co/NC@CeX-700 series exhibit graphitic (002) plane at 26.1°, again aligned with the HRTEM image (Fig. 4.1e). On the other hand, no trace of ALD ceria is detected by XRD from any sample in the Co/NC@CeX-700 series, which can be ascribed to the tiny amount of ceria incorporated by ALD.

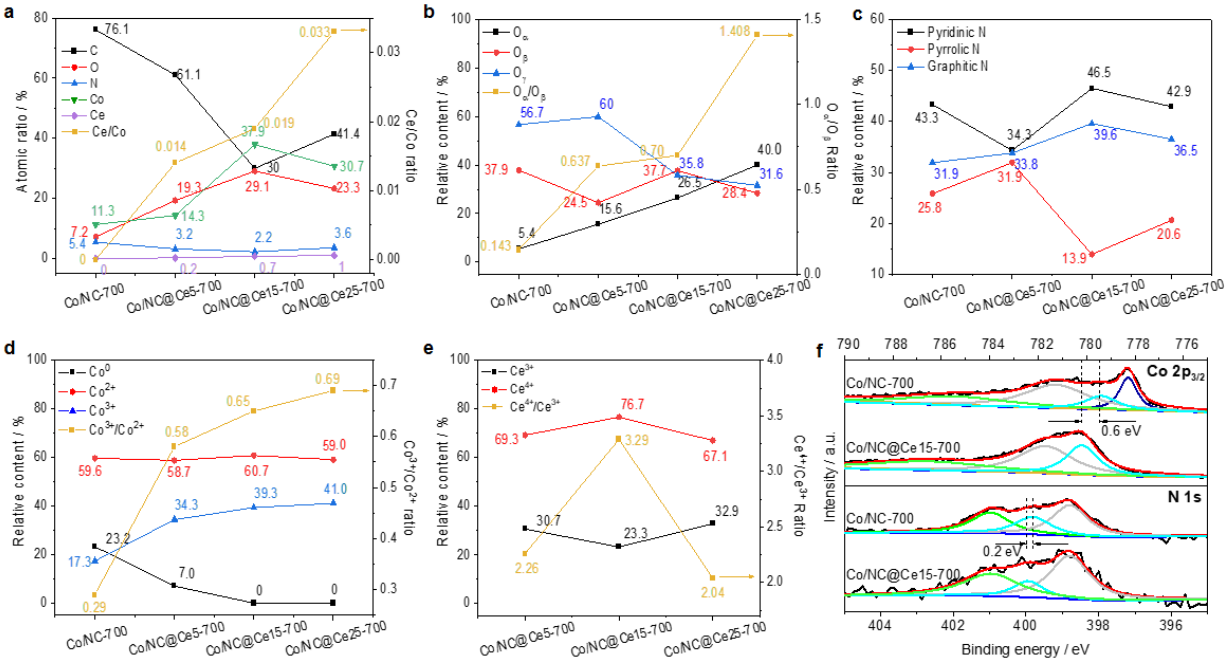


**Figure 4.8** (a) Atomic ratios determined from a wide scan XPS spectrum. (b-e) relative contents of species determined by O 1s (b), N 1s (c), Co 2p (d) and Ce 3d (e). (f) Co 2p and N 1s spectra exhibiting BE shifts. All the corresponding XPS spectra and tables are provided in Fig. 4.9 and Tables 4.1-4.5.

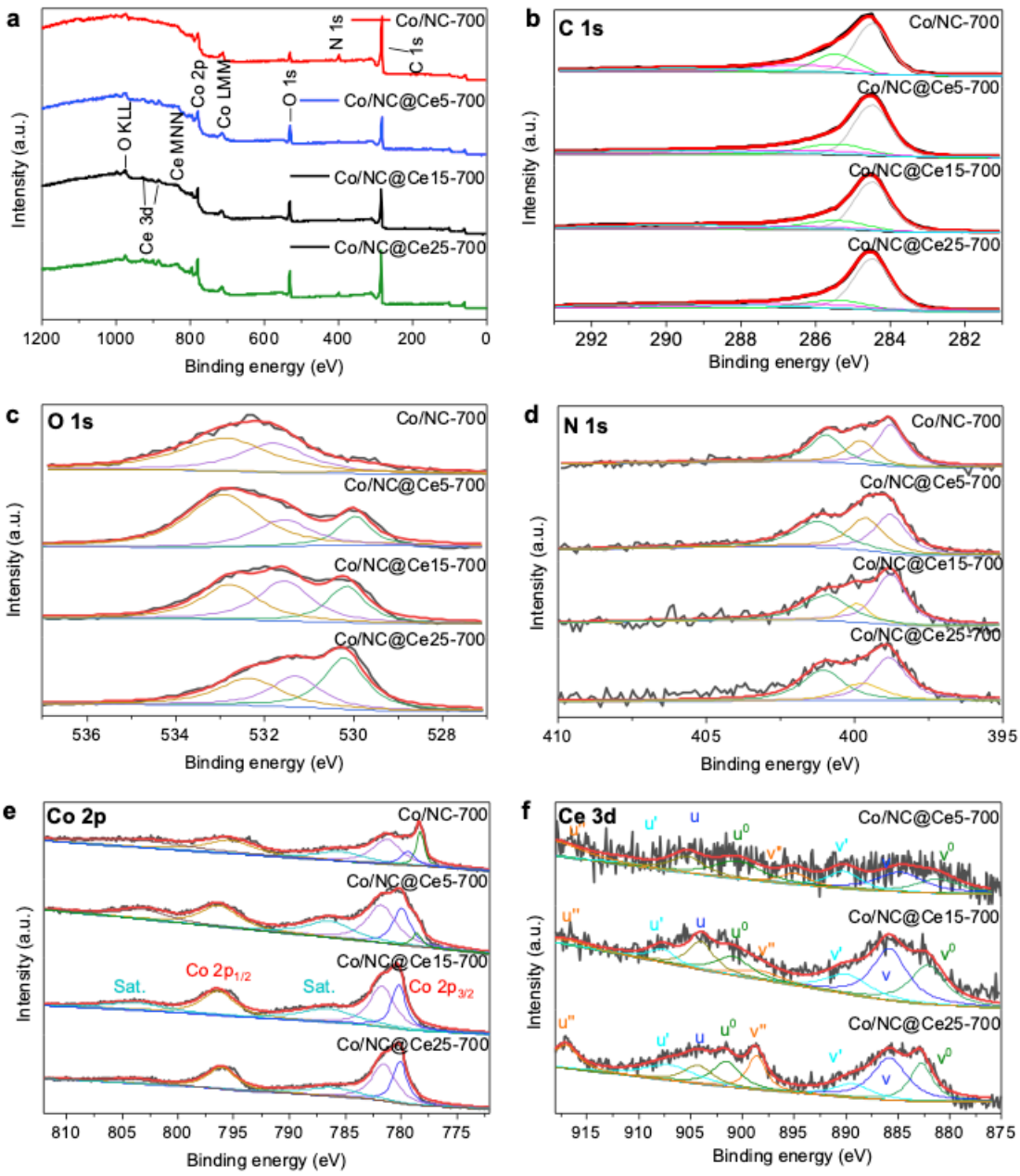


**Figure 4.9** XPS spectra for Co/NC-700 and Co/NC@CeX-700 series. (a) Wide scan spectrum and (b-f) high resolution spectra of C 1s, O 1s, N 1s, Co 2p and Ce 3d.

XPS is performed to identify the chemical composition and valence states of the samples. The survey spectrum reveals the presence of C, N, O and Co for Co/NC-700 while Ce peaks are additionally detected from the samples with ceria ALD (Fig. 4.8a and Fig. 4.9a).

The Ce content in each hybrid catalyst is very small; in Co/NC@Ce15-700, the relative Ce/Co atomic ratio is calculated to be 0.019 (Fig. 4.8a). Considering XPS is a highly surface sensitive technique, the actual Ce content is expected to be much smaller than Co content. When quantified by a TEM-EDS spectrum, the ratio is only 0.0062 (Fig. 4.5). The C 1s peak (Fig. 4.9b) can be deconvoluted into three peaks, corresponding to $sp^2$ C-C (284.3 eV), C-O/C-N (285.5) and C=O/C=N (286.3) [15,76]. With more ALD cycles, the C-O/C-N peak becomes smaller, indicating the loss of oxygen-containing groups from the carbon surface due to the reducing environment of ALD process (i.e., mild vacuum at 250 °C). Therefore, the increase in the overall O 1s peak intensity by ALD (Fig. 4.8a) can be mainly ascribed to the oxygen of ceria NPs introduced by ALD, not to carbon oxidation. The O 1s spectrum (Fig. 4.9c) are deconvoluted into $O_\alpha$ (529.7 eV), $O_\beta$ (531.8 eV) and $O_\gamma$ (532.9 eV), each corresponding to lattice oxygen in M–O (M: Co or Ce), surface oxygen defect (i.e., oxygen vacancy) and surface adsorbed oxygen-containing species, respectively [77,78]. The larger $O_\alpha$ peaks with ALD cycles further supports a successful ceria deposition (Fig. 4.8b). The Co $2p_{3/2}$ spectra (Fig. 4.9e) show peaks corresponding to $Co^0$ (778.3 eV), $Co^{3+}$ (779.4 eV) and $Co^{2+}$ (781.3 eV)[79,80]. The negligible $O_\alpha$ peak and prominent $Co^0$ peak of Co/NC-700 indicates that its Co is mostly in the metallic state while the presence of $Co^{2+}$ and $Co^{3+}$ peaks is ascribed to surface Co ions attached to oxygen adsorbates. The $Co^0$ content decreases significantly from 23.2% to 7.0% with only 5 cycles of ceria ALD, and no more $Co^0$ is detected with larger ALD cycles (Fig. 4.8d), which shows an oxidation of Co species by ALD-introduced oxygen. With ALD cycles, Co 2p peaks also progressively shift to higher binding energies (BEs) as shown in Fig. 4.8f and Fig. 4.9e, suggesting a strong electronic interaction between pre-existing Co species and ALD-derived species. With an optimum amount of ceria ALD, $Co_3O_4$ phase is formed in Co/NC@Ce15-700 as detected by XRD. Notably, Co/NC@Ce15-700 shows the strongest $O_\beta$ peak (Fig. 4.8b; Fig. 4.9c) that corresponds to oxygen vacancies, a widely accepted active site for oxygen electrocatalysis[54,81,82]. Simultaneously, Co/NC@Ce15-700 shows the highest $Ce^{4+}/Ce^{3+}$ ratio (Fig. 4.8e), suggesting that ceria attracts oxygen from $CoO_x$ leaving oxygen vacancies in $CoO_x$ (including $Co_3O_4$) [60]. However, the sample still has a large fraction of $Ce^{3+}$ (23.3%), hence a good amount of oxygen vacancies on ceria for the activation of reactants

as discussed below. On the other hand, three deconvoluted peaks of N 1s at 398.6, 399.8 and 400.3 eV (Fig. 4.9d) can be assigned to pyridinic, pyrrolic and graphitic N, respectively. The pyridinic and graphitic N are known to play an important role as an active site for oxygen electrocatalysis; while the former is reported as an active sites for both ORR and OER as well as enhancing the surface wettability and onset potential, the latter facilitates diffusion-limited processes [83–85]. As shown in Fig. 4.8c, the Co/NC@Ce15-700 has higher pyridinic (46.5%) and graphitic N (39.6%) than the other samples, which further makes Co/NC@Ce15-700 advantageous for ORR and OER performance. In addition, the continuous BE shift of graphitic N and pyrrolic N with ALD cycles (Fig. 4.8f) hints the possible formation of graphitic-N-Ce and pyrrolic-N-Ce bonding. Little change in the pyridinic N peak location may be due to preoccupation of pyridinic-N-Co bonding [86].

**Table 4.1** Atom ratios (%) determined from XPS survey spectrum

| | **Co/NC-700** | **Co/NC@Ce5-700** | **Co/NC@Ce15-700** | **Co/NC@Ce25-700** |
|---|---|---|---|---|
| C (%) | 76.1 | 61.1 | 30.0 | 41.4 |
| O (%) | 7.2 | 19.3 | 29.1 | 23.3 |
| N (%) | 5.4 | 3.2 | 2.2 | 3.6 |
| Co (%) | 11.3 | 14.3 | 37.9 | 30.7 |
| Ce (%) | 0 | 0.2 | 0.7 | 1.0 |

**Table 4.2** Relative contents of O species determined by O 1s XPS.

| | **Co/NC-700** | **Co/NC@Ce5-700** | **Co/NC@Ce15-700** | **Co/NC@Ce25-700** |
|---|---|---|---|---|
| $O_\alpha$ (%) | 5.4 | 15.6 | 26.5 | 40.0 |
| $O_\beta$ (%) | 37.9 | 24.5 | 37.7 | 28.4 |
| $O_\gamma$ (%) | 56.7 | 60.0 | 35.8 | 31.6 |

**Table 4.3** Relative contents of N species determined by N 1s XPS.

| | **Co/NC-700** | **Co/NC@Ce5-700** | **Co/NC@Ce15-700** | **Co/NC@Ce25-700** |
|---|---|---|---|---|
| Pyridinic (%) | 43.3 | 34.3 | 46.5 | 42.9 |
| Pyrrolic (%) | 25.8 | 31.9 | 13.9 | 20.6 |
| Graphitic (%) | 31.9 | 33.8 | 39.6 | 36.5 |

**Table 4.4** Relative contents of Co species determined by Co 2p XPS.

| | **Co/NC-700** | **Co/NC@Ce5-700** | **Co/NC@Ce15-700** | **Co/NC@Ce25-700** |
|---|---|---|---|---|
| $Co^0$ (%) | 23.2 | 7.0 | 0 | 0 |
| $Co^{2+}$ (%) | 59.6 | 58.7 | 60.7 | 59.0 |
| $Co^{3+}$ (%) | 17.3 | 34.3 | 39.3 | 41.0 |

**Table 4.5** Relative contents of Ce species determined by Ce 3d XPS.

| | Co/NC@Ce5-700 | Co/NC@Ce15-700 | Co/NC@Ce25-700 |
|---|---|---|---|
| $Ce^{3+}$ (%) | 30.7 | 23.3 | 32.9 |
| $Ce^{4+}$ (%) | 69.3 | 76.7 | 67.1 |
| $Ce^{4+}/Ce^{3+}$ | 2.25 | 3.29 | 2.04 |

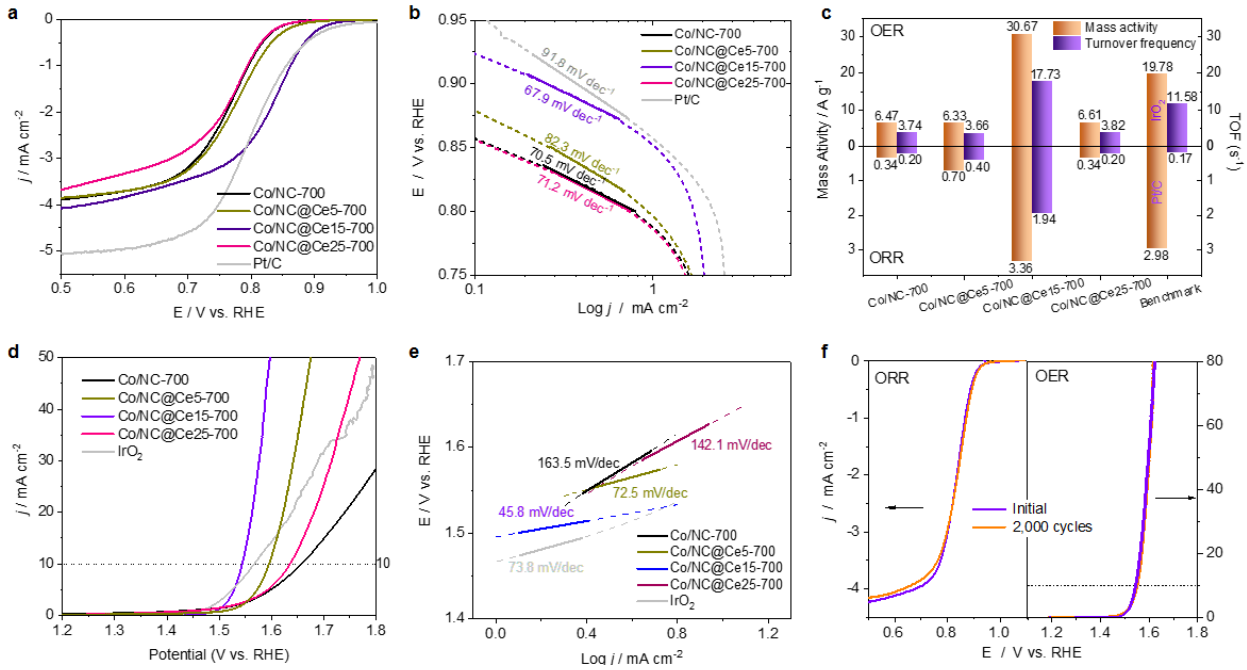


**Figure 4.10** Electrochemical measurement of Co/NC-700, Co/NC@CeX-700 series and noble metal benchmarks. (a, b) LSV curves obtained in 0.1 M KOH for ORR (a), and their corresponding Tafel slopes (b). (d, e) LSV curves obtained in 1 M KOH for OER (d), and their corresponding Tafel slopes (e). (c) Mass activity and turnover frequencies. (f) Cyclic durability measurements; LSV obtained before and after 2,000 cycles between 0.1 V – 1.0 V for ORR and 1.5 V – 1.85 V for OER, both at 100 mV s-1. All LSV curves are obtained on a glassy carbon-based rotating electrode at 1,600 rpm and presented after IR correction.

The electrochemical performance of the hybrid samples, along with noble metal benchmark catalysts for comparison, is characterized. For ORR, Co/NC@Ce15-700 shows the best performance among the hybrid variants (Fig. 4.10a) with the onset ($E_{on}$) and half-wave potentials ($E_{1/2}$) of 0.95 V and 0.84 V (vs. RHE hereafter), respectively, significantly higher than those of Co/NC-700 ($E_{on}$ = 0.89 V and $E_{1/2}$ = 0.77 V). Compared to the commercial Pt/C catalysts, Co/NC@Ce15-700 exhibits a slightly lower $E_{on}$ by 20 mV but a higher $E_{1/2}$ by 30 mV, demonstrating a promising ORR activity. The other two ALD treated samples (Co/NC@Ce5-700 and Co/NC@Ce25-700) show little improvement in ORR performance compared to Co/NC-700.

Co/NC@Ce15-700 also exhibits a Tafel slope of 67.9 mV $dec^{-1}$, smaller than that of Pt/C (91.8 mV $dec^{-1}$; Fig. 4.10b), confirming its fast ORR kinetics. In a RRDE setup, the electron transfer number ($n$) of Co/NC@Ce15-700 is quantified to be 3.84 on average over the potential range of 0.5 – 0.8 V exhibiting mostly four-electron ORR pathway whereas Co/NC@Ce5-700 and Co/NC@Ce25-700 render lower values of 3.64 and 3.66, respectively (Fig. 4.11).

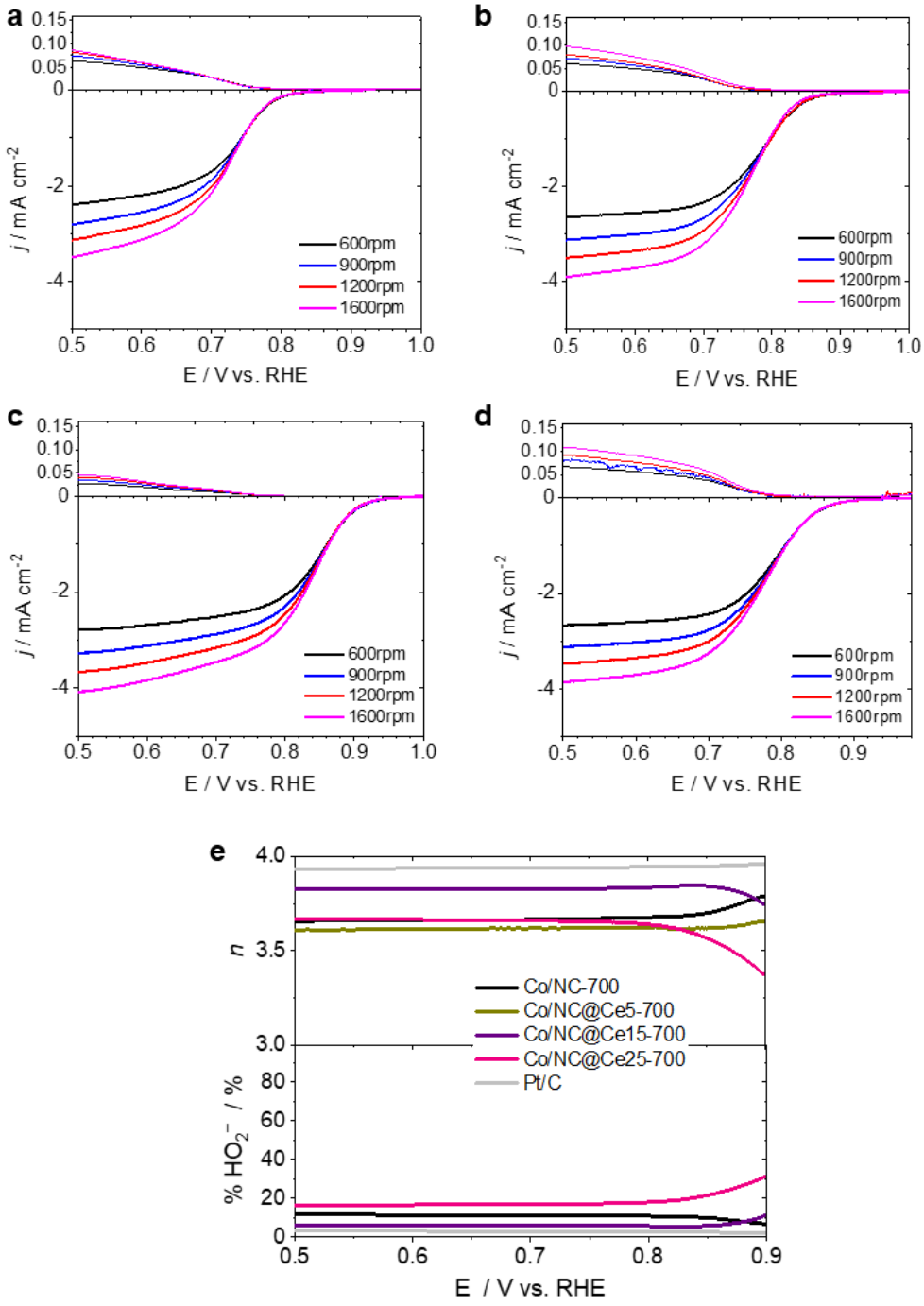


**Figure 4.11** RRDE curves of (a) Co/NC-700. (b) Co/NC@Ce5-700. (c) Co/NC@Ce15-700. (d) Co/NC@Ce25-700. Upper: ring current. Lower: disk current. (e) ORR electron transfer number (n) and peroxide yield derived from the RRDE voltammograms.

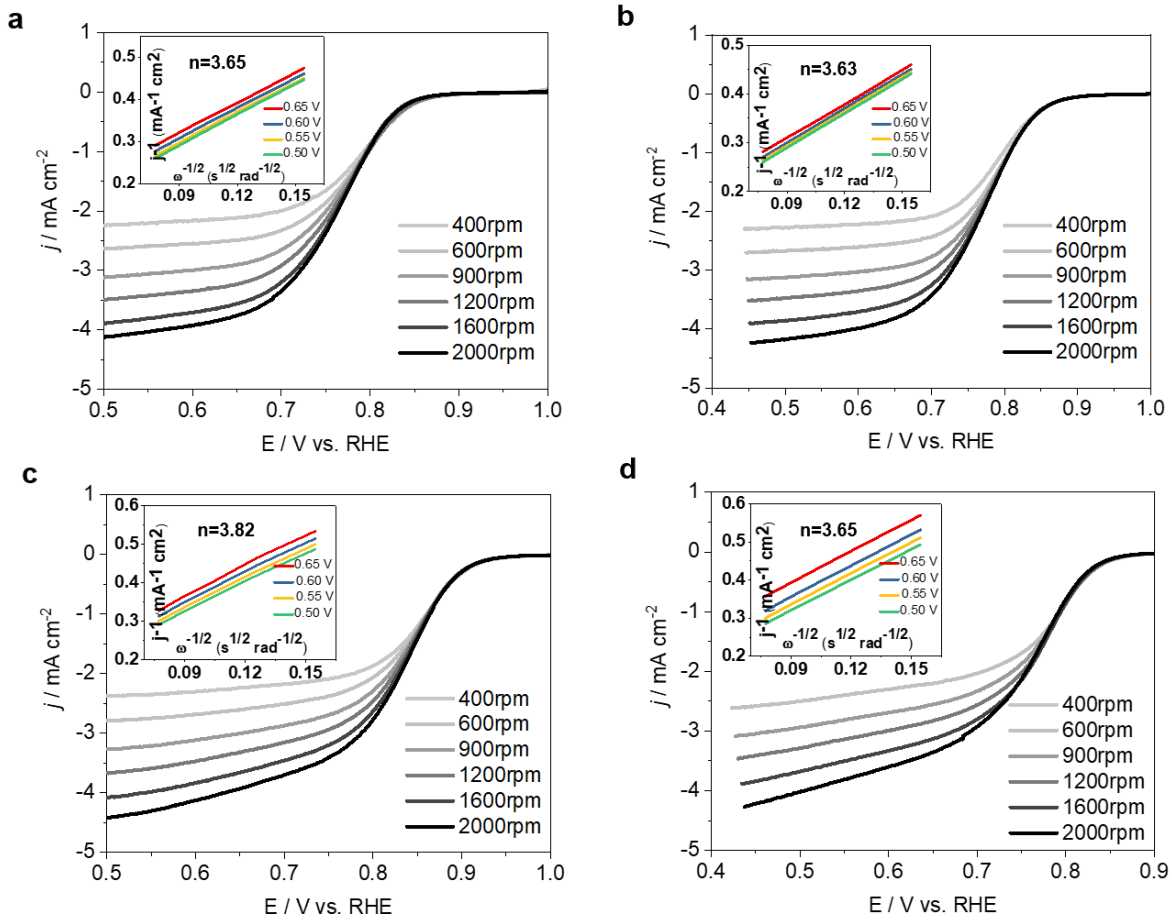


**Figure 4.12** LSV curves at various electrode rotating speeds. (a) Co/NC-700, (b) Co/NC@Ce5-700, (c) Co/NC@Ce15-700 and (d) Co/NC@Ce25-700. Inset: The corresponding Koutechy-Levich plot at various disk potentials; *n* is the electron transfer number quantified at 0.5 V.

These are consistent with the result from Koutecky-Levich analysis; *n* = 3.63, 3.82 and 3.65 at 0.55 V for Co/NC@Ce5-700, Co/NC@Ce15-700 and Co/NC@Ce25-700, respectively (Fig. 4.12). Even for OER, Co/NC@Ce15-700 exhibits the best performance. It reaches 10 mA $cm^{-2}$ at 1.53 V (namely, $E_{10}$ = 1.53 V; Fig. 4.10d), lower than all the other samples: Co/NC-700 (1.65 V), Co/NC@Ce5-700 (1.59 V), Co/NC@Ce25-700 (1.63 V) and $IrO_2$ (1.56 V); a summary of OER $E_{10}$ and ORR $E_{1/2}$ is provided in Fig. 4.13. The

Co/NC@Ce15-700 also shows the lowest Tafel slope (45.8 mV $dec^{-1}$), significantly lower than $IrO_2$ (73.8 mV $dec^{-1}$), again indicating its fast kinetics for OER.

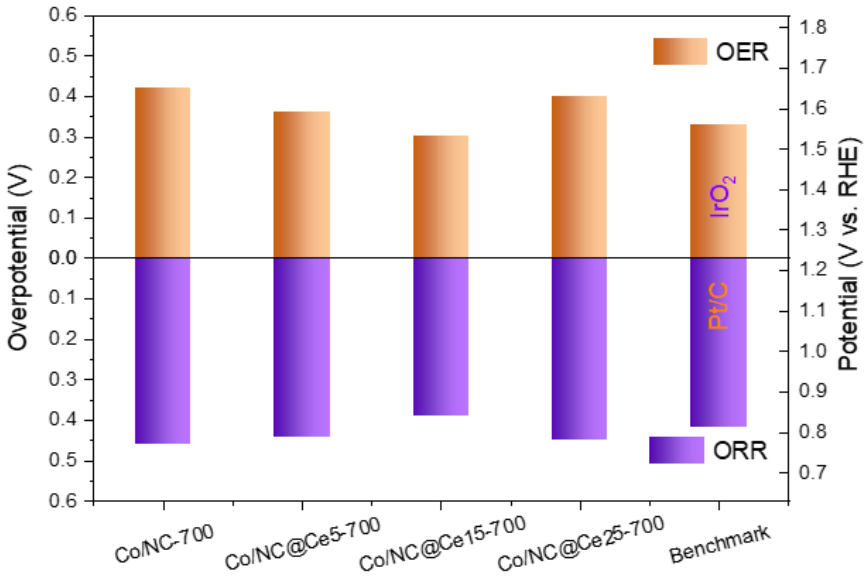


**Figure 4.13** ORR half-wave potentials and OER $E_{10}$ values of Co/NC-700, Co/NC@CeX-700 series and benchmark catalyst.

To gauge the intrinsic activity of the samples, the mass activity and turnover frequency (TOF) are quantified at the overpotential of 0.35 V for both ORR and OER. As shown in Fig. 4.10c, Co/NC@Ce15-700 shows the highest mass activity (30.7 A $g^{-1}$ for OER; 3.36 A $g^{-1}$ for ORR) and TOF (17.7 $s^{-1}$ for OER; 1.94 $s^{-1}$ for ORR), indicating the highest atom use efficiency and largest intrinsic active sites toward both ORR and OER.

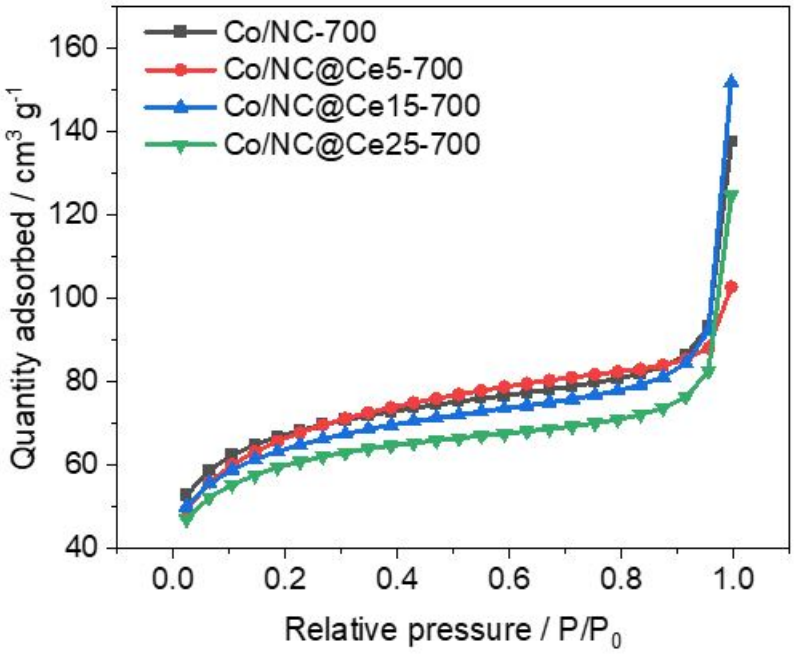


**Figure 4.14** Nitrogen adsorption isotherm curves of Co/NC-700, Co/NC@Ce5-700, Co/NC@Ce15-700 and Co/NC@Ce25-700.

As displayed in Fig. 4.14, the BET surface area of Co/NC-700, Co/NC@Ce5-700, Co/NC@Ce15-700 and Co/NC@Ce25-700 are 248.8, 238.6, 234.6 and 220.5 $m^2$ $g^{-1}$, respectively. The specific surface area tends to decrease slightly with more ALD cycles. Since the BET surface area represents only the total surface area of the catalysts regardless of catalytic activity, the similar BET surface areas among samples indicate that the improved electrochemical performance by ALD is caused by an increased amount of catalytically active sites.

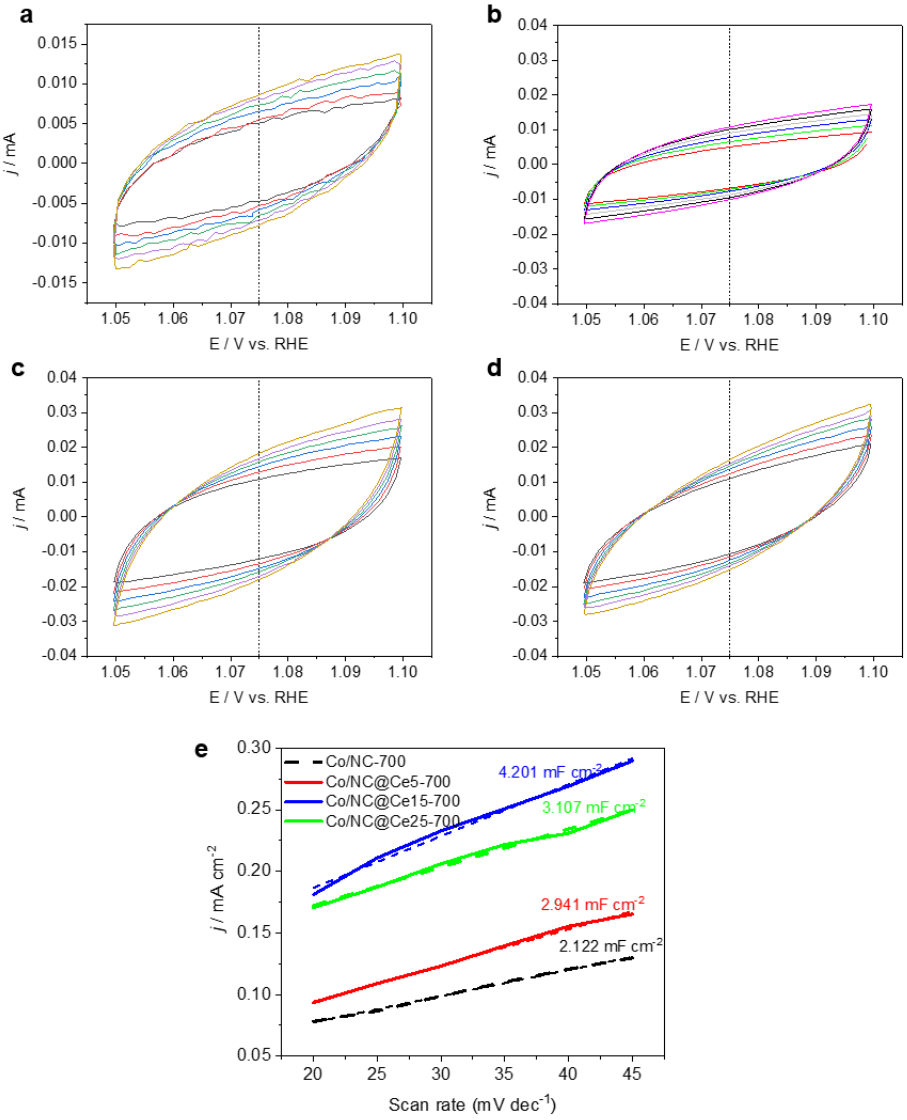


**Figure 4.15** ECSA measurement of (a) Co/NC-700, (b) Co/NC@Ce5-700, (c) Co/NC@Ce15-700 and (d) Co/NC@Ce25-700. (e) Quantification of double layer capacitance based upon the CVs.

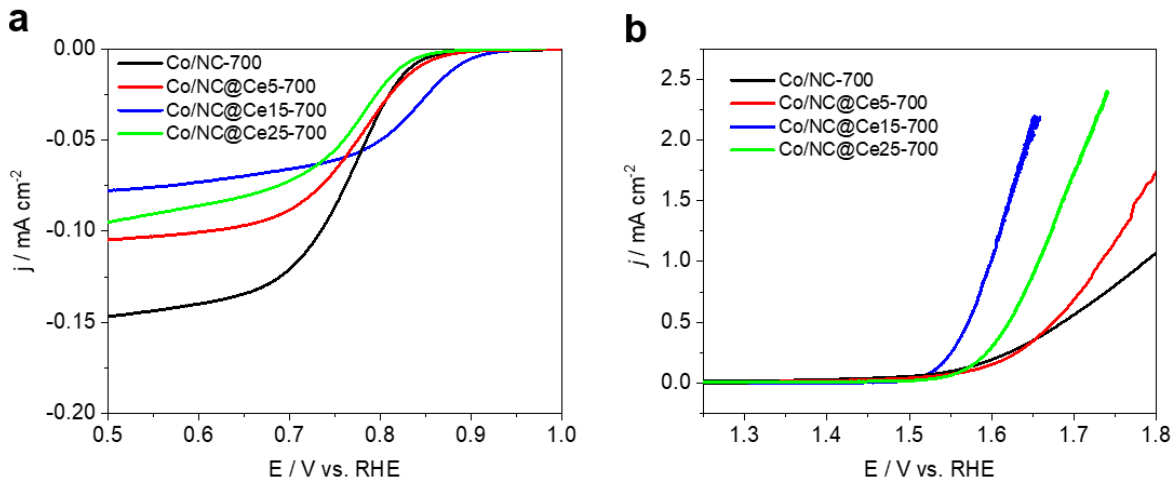


**Figure 4.16** ECSA-normalized polarization curves for ORR (a) and OER (b).

To further investigate the catalytically active surface area of the as prepared samples, the ECSA of Co/NC-700 and Co/NC@CeX-700 series are also quantified by the CV method (Fig. 4.15). The resulting double layer capacitances ($C_{dl}$) of Co/NC@Ce15-700 is 4.20 mF $cm^{-2}$, larger than those of Co/NC-700 (2.12 mF $cm^{-2}$), Co/NC@Ce5-700 (2.94 mF $cm^{-2}$) and Co/NC@Ce25-700 (3.11 mF $cm^{-2}$). The high ECSA is partially ascribed to the aforementioned nanopores formed in the carbon matrix. In terms of ECSA normalized current, Co/NC@Ce15-700 still exhibits the lowest overpotential for the whole OER current range, further confirming its higher intrinsic activity for OER while it shows a rather lower normalized current for ORR compared to the other samples in the mass transport-limited region (Fig. 4.16). The roughness factor for sample Co/NC-700, Co/NC@Ce5-700, Co/NC@Ce15-700 and Co/NC@Ce25-700 is 26.5, 36.8, 52.5 and 38.7, respectively.

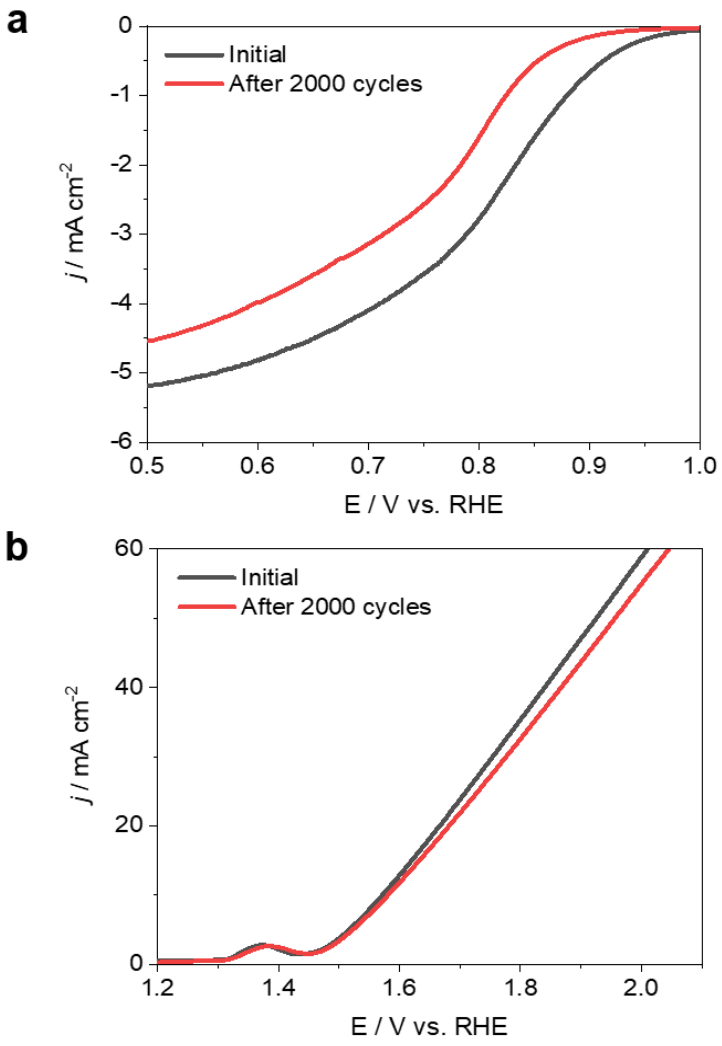


**Figure 4.17** (a) ORR cyclic durability test of Pt/C in 0.1 M KOH in the potential window of 0.5 – 1.0 V. (b) OER cyclic durability test of $IrO_2$ in 1 M KOH in the potential window of 1.2 – 1.8 V.

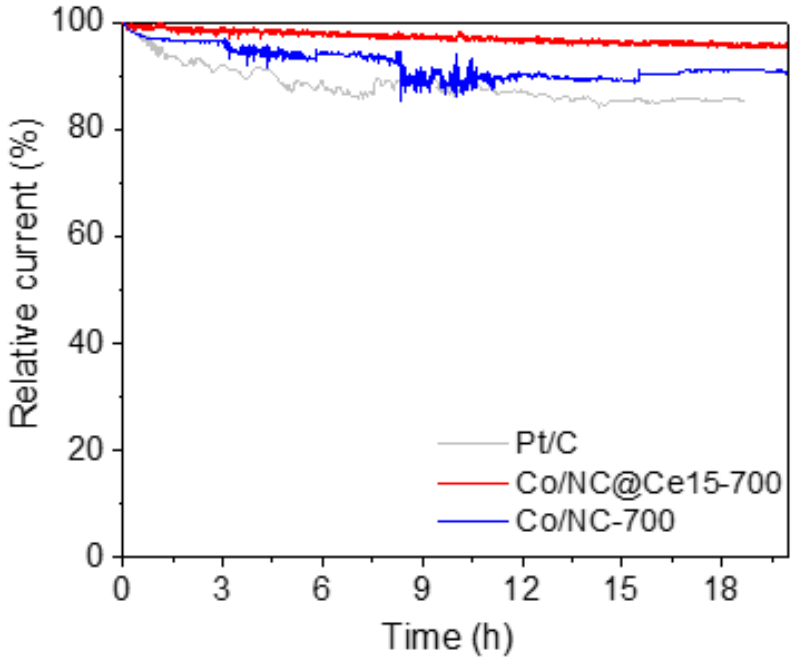


**Figure 4.18** Chronoamperometric stability evaluation for ORR in comparison with Pt/C in 0.1 M KOH at 0.4 V versus RHE.

In addition, Co/NC@Ce15-700 shows an excellent cyclic stability for both ORR and OER. There is little noticeable change in ORR $E_{on}$ and $E_{1/2}$ after 2,000 cycles (Fig. 4.10f) while $E_{on}$ and $E_{1/2}$ of Pt/C decrease by 50 mV and 60 mV, respectively (Fig. 4.17a). In a chronoamperometric measurement, Co/NC@Ce15-700 maintains 97% of the initial current density after 10 h at 0.4 V whereas both Pt/C and Co/NC-700 catalysts retain only 86% (Fig. 4.18), further revealing the superior stability of Co/NC@Ce15-700. Likewise, Co/NC@Ce15-700 shows no observable change in the OER voltammogram between the initial and 2,000 cycles (Fig. 4.10f). On the other hand, the $IrO_2$ benchmark barely reaches 60 mA $cm^{-2}$ at 2.0 V, and an additional overpotential of 30 mV is needed to reach 60 mA $cm^{-2}$ after 2,000 cycles (Fig. 4.17b).

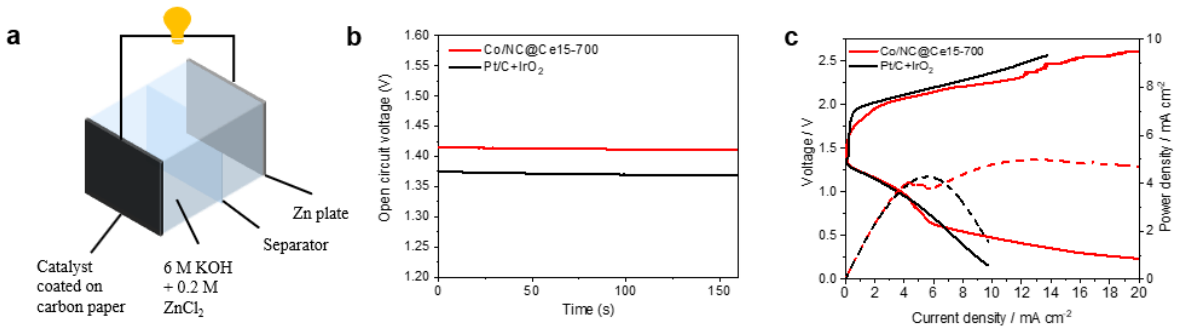


**Figure 4.19** Zn-air battery tests on Co/NC@Ce15-700 and Pt/C + $IrO_2$ mixtures. (a) Schematic of primary Zn-air battery assembly. (b) Open-circuit voltage for the as-prepared Zn-air battery. (c) Charge/discharge polarization and power density curves.

Motivated by the superior electrocatalytic performance of Co/NC@Ce15-700 toward both ORR and OER, we demonstrate a primary Zn-air battery with the hybrid catalyst. The cell is prepared by using a catalyst-coated carbon cloth as the air cathode, a polished Zn plate as the anode and 0.2 M $ZnCl_2$ in 6 M KOH as the electrolyte (Fig. 4.19a). A reference cell with a mixture of Pt/C and $IrO_2$ is also characterized for comparison. As shown in Fig. 4.19b, the assembled Zn-air battery displays an open-circuit voltage of 1.42 V, enhanced compared to the mixture of Pt/C and $IrO_2$ (1.37 V). The charge-discharge polarization curves of the Zn-air batteries (Fig. 4.19c) show that Co/NC@Ce15-700 clearly exhibits a considerably better performance than that of the noble metal mixture. Moreover, Co/NC@Ce15-700 delivers a peak power density of 5.0 mW $cm^{-2}$ at a current density of 12.8 mA $cm^{-2}$, outperforming the noble metal mixture catalysts (4.28 mW $cm^{-2}$ at 5.53 mA $cm^{-2}$).

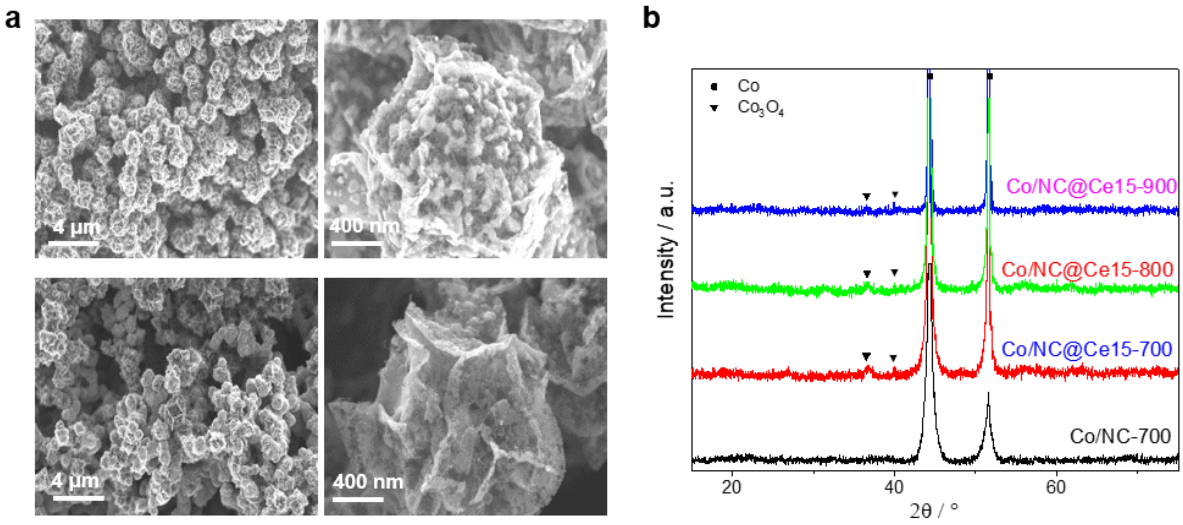


**Figure 4.20** (a) SEM image of Co/NC@Ce15-800 (upper) and Co/NC@Ce15-900 (lower). (b) XRD patterns of Co/NC@Ce15-Y series.

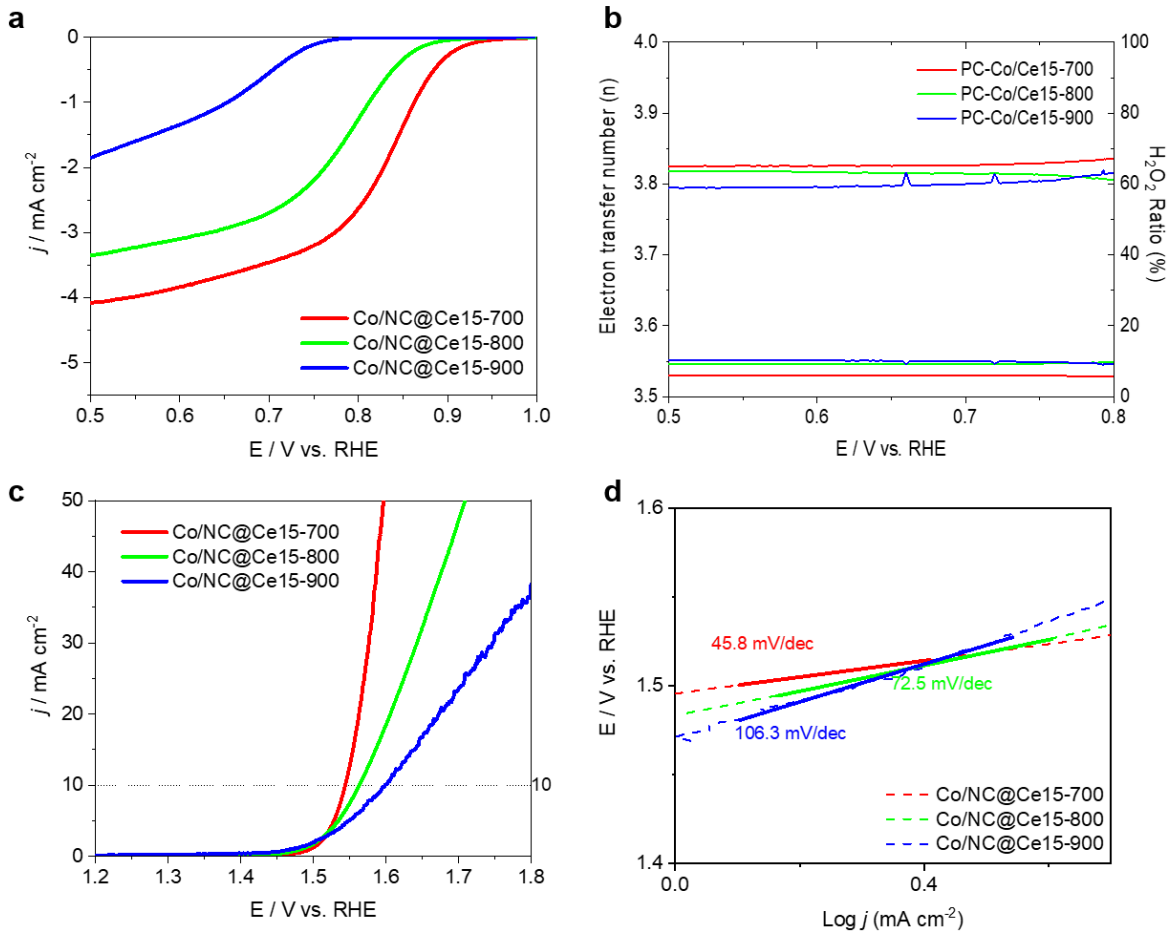


**Figure 4.21** Electrochemical characterization of Co/NC@Ce15-Y series samples pyrolyzed at different temperatures (700, 800 and 900 °C). (a) ORR LSV curves, (b) electron transfer numbers ($n$) and $HO_2^-$ production ratios, and (c) OER LSV curves at 1600 rpm. (d) Tafel slopes for OER in 1 M KOH.

The dependency of catalytic performance on pyrolysis temperature is briefly presented here. When pyrolyzed at a temperature higher than 700 °C, the samples show significant differences in morphology due to a severe aggregation during pyrolysis (Fig. 4.20a) while they all show similar Co crystal dominant XRD spectra (Fig. 4.20b). Pyrolysis at higher temperatures results in a compromised ORR performance with much lower onset and half-wave potentials (Fig. 4.21): Co/NC@Ce15-800 ($E_{on}$ = 0.89 V, $E_{1/2}$ = 0.79 V) and Co/NC@Ce15-900 ($E_{on}$ = 0.79 V and $E_{1/2}$ = 0.68 V). The same trend persists for OER (Fig.

4.21c); Co/NC@Ce15-800 and Co/NC@Ce15-900 show $E_{10}$ values of 1.56 V and 1.60 V, respectively, significantly larger than those prepared at 700 °C.

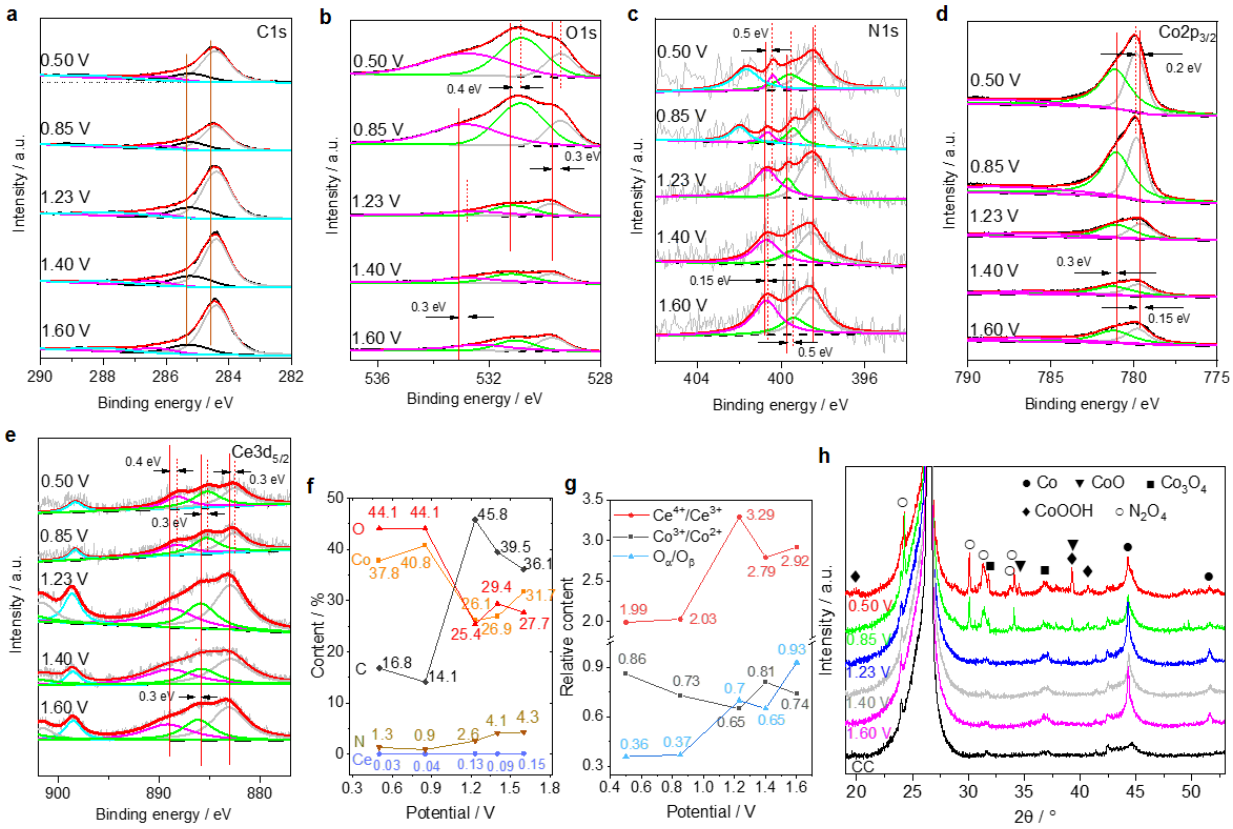


**Figure 4.22** (a-e) XPS spectra of Co/NC@Ce15-700 at different potentials. (f) Relative atomic ratios of each content quantified from a survey spectrum. (g) Relative contents quantified from Ce 3d, Co 2p and O 1s spectra. (h) XRD spectra after exposing Co/NC@Ce15-700 at different potentials.

To better reveal the active sites of the best performing Co/NC@Ce15-700 for ORR and OER, *quasi-operando* XPS and XRD analyses is additionally performed after exposing the sample to different potentials for 10 min (see Methods section for details in sample preparation): 1.23 V for

open circuit potential (OCP), 0.85 V and 0.50 V for ORR and 1.40 V and 1.60 V for OER (Fig. 4.22 and Tables 4.6 – 4.11). After ORR, the overall O 1s signal is highly intensified (25.4% at OCP → 44.1% at 0.50 V; Fig. 4.22f). This can be partially ascribed to more

populated molecular adsorbates (corresponding to the $O_\gamma$ peak in O 1s) but the rather mild increase in $O_\gamma$ peak (35.8% at OCP → 41.4% at 0.50 V; Fig. 4.22g and Table 4.9) does not fully justify the surge in the overall O 1s intensity. We ascribe the O 1s intensification additionally to the formation of CoOOH during ORR [87–89] as revealed by the XRD spectrum (Fig. 4.22h); the CoOOH peaks (ICDD no. 00-014-0673), which are absent at OCP, appear at 0.50V. Compared to $Co_3O_4$, CoOOH is expected to exhibit a much higher $O_\beta$ intensity of O 1s spectra with a concomitant suppression in $O_\alpha$ peak [90], which is well reflected in Fig. 4.22b and Fig. 4.22g ($O_\alpha/O_\beta$ = 0.703 at OCP → 0.356 at 0.50 V).

The decrease in $O_\alpha/O_\beta$ ratio during ORR also suggests the formation of oxygen vacancies, but the change in the valence states of Ce (decrease) and Co (increase) as shown in Fig. 4.22g implies that the oxygen vacancies are mainly formed in ceria rather than in cobalt oxide during ORR. On the other hand, the increase of $Co^{3+}/Co^{2+}$ ratio (0.65 at OCP → 0.86 at 0.50 V) is mainly ascribed to CoOOH formation; $Co_3O_4$ is expected to have a $Co^{3+}/Co^{2+}$ ratio of 2, and CoOOH has mostly $Co^{3+}$ valence. These observations can be interpreted that ceria serves as an oxygen buffer while cobalt oxide advances ORR by changing its valence and phase. The higher $Ce^{3+}$ content found at ORR potentials indicates a facile transfer of oxygen species ($OO^{2-}$ or $O^{-}$) from $CeO_x$ to $CoO_x$, readily restoring $Ce^{3+}$ valence state during continuous ORR. For a continuous adsorption and dissociation of $O_2$, preserving higher $Ce^{3+}$ concentration should be advantageous; $Ce^{3+}$ cations and oxygen vacancies lower oxygen adsorption energy and elongate O–O bonds facilitating oxygen dissociation [82]. The XRD spectra additionally reveal the formation of CoO (ICDD no. 01-075-0419) during ORR, which is also known to be highly active for ORR [89,91]. It is important to note that the binding energies of Co $2p_{3/2}$ peaks shift positively (Fig. 4.22d) while those of Ce $3d_{5/2}$ peak shift negatively (Fig. 4.22e) during ORR, suggesting a strong electronic coupling between the two cationic species and their synergistic contribution toward ORR. On the other hand, the peak at ca. 402 eV in N 1s spectra, which is absent at OCP, become prominent during ORR (0% at OCP → 19.8% at 0.85 V → 34.4% at 0.50 V) while the peak for graphitic N (i.e., quaternary N) diminishes significantly (41.8% at OCP → 10.3% at 0.85 V → 7.3% at 0.50 V). Combined with the fact that 402 eV peak can correspond to adsorbed O at the basal site of graphitic N [92], the changes in N 1s spectra

suggests an important role of graphitic N in ORR. However, we do not exclude the possible contribution of pyridinic N to the activity because the peak at 402 eV can also be ascribed to pyridinic N–$O^+$. In accordance with the emergence of N–O bond at ca. 402 eV, the XRD spectra (Fig. 4.22f) also suggest nitrogen oxide formation (IDCC no. 01-074-2264) during ORR, supporting that N sites serve as another active site for ORR. The significant BE shift in the graphitic N peak also signals a strong electronic interaction between graphitic N and cations (Co and/or Ce) possibly for a synergistic effect toward ORR.

**Table 4.6** Atomic ratios of each element determined by survey spectra at different potentials.

| Potential (V) | Co (%) | Ce (%) | O (%) | N (%) | C (%) |
|---|---|---|---|---|---|
| 0.50 | 37.8 | 0.03 | 44.0 | 1.34 | 16.75 |
| 0.85 | 40.8 | 0.04 | 44.0 | 0.90 | 14.14 |
| 1.23 | 26.1 | 0.13 | 25.4 | 2.55 | 45.78 |
| 1.40 | 26.9 | 0.09 | 29.4 | 4.05 | 39.58 |
| 1.60 | 31.7 | 0.15 | 27.7 | 4.26 | 36.11 |

**Table 4.7** Relative contents of Co species determined by Co 2p spectra at different potentials.

| Potential (V) | $Co^{3+}$ (%) | $Co^{2+}$ (%) | $Co^{3+}/Co^{2+}$ |
|---|---|---|---|
| 0.50 | 46.1 | 53.9 | 0.855 |
| 0.85 | 42.1 | 57.9 | 0.727 |
| 1.23 | 39.3 | 60.7 | 0.647 |
| 1.40 | 44.7 | 55.3 | 0.808 |

| | | | |
|---|---|---|---|
| 1.60 | 42.4 | 57.6 | 0.736 |

**Table 4.8** Relative contents of Ce species determined by Ce 3d spectra at different potentials.

| **Potential (V)** | **$Ce^{4+}$ (%)** | **$Ce^{3+}$ (%)** | **$Ce^{4+}/Ce^{3+}$** |
|---|---|---|---|
| 0.50 | 67.2 | 33.8 | 1.99 |
| 0.85 | 67.7 | 33.3 | 2.03 |
| 1.23 | 76.7 | 23.3 | 3.29 |
| 1.40 | 73.6 | 26.4 | 2.79 |
| 1.60 | 74.5 | 25.5 | 2.92 |

**Table 4.9** Relative contents of O species determined by O 1s spectra at different potentials.

| **Potential (V)** | **$O_\alpha$ (%)** | **$O_\beta$ (%)** | **$O_\gamma$ (%)** | $O_\alpha/O_\beta$ |
|---|---|---|---|---|
| 0.50 | 15.4 | 43.2 | 41.4 | 0.356 |
| 0.85 | 16.7 | 44.8 | 38.5 | 0.372 |
| 1.23 | 26.5 | 37.7 | 35.8 | 0.703 |
| 1.40 | 23.0 | 35.6 | 41.4 | 0.646 |
| 1.60 | 29.0 | 31.2 | 39.8 | 0.929 |

**Table 4.10** Relative contents of N species determined by N 1s XPS under different potential.

| Potential (V) | pyridinic (%) | pyrrolic (%) | graphitic (%) | N-O (%) |
|---|---|---|---|---|
| 0.50 | 42.6 | 15.7 | 7.3 | 34.4 |
| 0.85 | 53.5 | 16.4 | 10.3 | 19.8 |
| 1.23 | 46.5 | 13.9 | 39.6 | 0 |
| 1.40 | 45.1 | 20.2 | 34.7 | 0 |
| 1.60 | 38.8 | 20.1 | 41.1 | 0 |

**Table 4.11** Relative contents of C species determined by C 1s XPS under different potential.

| Potential (V) | C=C (%) | C-C/C-H (%) | C-N/C-O (%) | C=N/C=O (%) |
|---|---|---|---|---|
| 0.50 | 63.6 | 19.6 | 9.6 | 9.2 |
| 0.85 | 60.1 | 23.3 | 10.3 | 6.2 |
| 1.23 | 66.4 | 18.6 | 5.6 | 9.4 |
| 1.40 | 68.0 | 19.0 | 7.4 | 5.7 |
| 1.60 | 69.3 | 15.8 | 8.1 | 6.7 |

On the other hand, a clearly different trend is observed during OER. First, the XRD spectra exhibit little change after OER (Fig. 4.22f), indicating that the reaction occurs mostly on defect sites without changing the crystal structures of cobalt oxide. This is unlike other Co-based OER studies that report the appearance of other phases such as CoOOH and $CoO_2$ during OER [87,93–95]. Although the only prominent $CoO_x$ phase revealed by XRD after OER is $Co_3O_4$ (Fig. 4.22f), the $Co^{3+}/Co^{2+}$ ratio ranging between 0.65 (at OCP) and 0.81 (at 1.40 V) strongly suggests that a significant portion of surface $CoO_x$ resides as an amorphous phase and/or other crystalline phases with a high concentration of $Co^{2+}$ valence because pure $Co_3O_4$ is expected to render $Co^{3+}/Co^{2+}$ ratio of 2. The Co $2p_{3/2}$ and Ce 3d peaks are shifted positively after OER while the graphitic-N and pyrrolic-N peaks shows a negative shift, implying that Co and Ce species interact with N-C through a strong electronic coupling during OER. In addition, the C-O/C-N peak (286.3 eV) in C 1s, which can be attributed to C-adsorbate bonding (C-OH, C-O or C-OOH), increases after OER (5.6% at OCP → 8.1% at 1.60 V), demonstrating an accumulation of oxygen intermediates on the carbon matrix [96]. This is corroborated by the decrease in C=O/C=N peak (287.7 eV; 9.4% at OCP → 6.7% at 1.60 V) in that C atoms of C=O group readily accept electrons from $OH^-$, forming surface adsorbed OH. On the other hand, the $O_\alpha/O_\beta$ ratio, which should be inversely proportional to oxygen vacancy concentration, decreases from 0.70 at OCP to

0.65 at 1.40 V and then increases to 0.92 at 1.60 V (Fig. 4.22g). Combined with the trend of $Ce^{4+}/Ce^{3+}$ (decrease → increase; Table S8) and $Co^{3+}/Co^{2+}$ ratios (increase → decrease; Table 4.7), the $O_\alpha/O_\beta$ trend indicates that the formation/annihilation of oxygen vacancies during OER occurs mostly on ceria, rather than on cobalt oxide, as is the case for ORR. This reassures the role of ceria as an oxygen buffer, making oxygen intermediates readily exchangeable for neighboring Co species to lead an efficient OER [57,59].

**Table 4.12** ORR and OER performance of Co/NC@Ce15-700 in comparison with other recently reported MOF-derived Co-based electrocatalysts. The OER overpotential is quantified by $E_{10} - E_{rev}$ in 1 M KOH and the ORR overpotential corresponds to $E_{rev} - E_{on}$ in 0.1 M KOH. Refs. [22,98–106]

| Electrocatalysts | Η for OER (V) | Η for ORR (V) | References |
|---|---|---|---|
| $Co_3O_4$@C-MWCNT | 0.34 | 0.32 | 5 |
| Co/$Co_3O_4$/NC | 0.38 | 0.33 | 6 |
| NCNTFs | 0.26 | 0.37 | 7 |
| N-$Co_3O_4$@NC | 0.34 | 0.27 | 8 |
| CoOHCat@NCF | 0.4 | 0.34 | 9 |
| Co@NC-0.75 | 0.22 | 0.36 | 10 |
| Pd@PdO-$Co_3O_4$ | 0.31 | 0.31 | 11 |
| $CoO_x$-N-C/$TiO_2$C | 0.21 | 0.35 | 12 |
| FeCo@MNC | 0.35 | 0.24 | 13 |
| Co-NC@$Al_2O_3$ | 0.32 | 0.41 | 14 |

The catalytic performance of the Co/NC@Ce15-700 catalyst for both ORR and OER compares favorably to recently reported MOF-derived Co-based bifunctional catalysts under the same electrochemical conditions (Table 4.12). The main reasons of the enhancement in electrocatalytic activity toward ORR and OER with a trace amount of ceria

incorporation can be summarized as follows. First, the retainment and fast restoration of a high concentration of trivalent Ce (hence oxygen vacancies) under ORR/OER conditions continuously activates reactant adsorbates and donates the activated oxygen intermediates to neighboring $CoO_x$ species to proceed with ORR/OER, affording a highly facilitated ORR/OER kinetics. In addition, the direct Co-Ce electronic coupling and indirect coupling through N-C, as revealed by XPS, is conjectured to have further enhanced electron transfer kinetics and catalytic activity. Moreover, density functional theory (DFT) calculations by H. Sun et al. [60] and J. Kim et al. [107] confirms that a Ce-Co-O bond causes a smaller OER overpotential than Co-O; the adsorption energy between active sites with intermediate ($OH^*$ and $O^*$) is reduced, which is beneficial for OER performance. Tiny $CeO_x$ species uniformly dispersed on $Co/CoO_x$ NPs, which is enabled by the unique capability of ALD, form a high concentration $Co/CoO_x$-$CeO_x$-reactant triple junctions for a maximized oxygen interchanges and electronic coupling between Co and Ce-based components. This, in addition to the nanopore formation, is believed to have partially contributed to the considerable enhancement of ECSA after a ceria ALD, further enhancing the overall ORR/OER activity of the hybrid catalyst.

## 4.4 Conclusion

We demonstrate a facile synthesis strategy to introduce a trace amount of $CeO_x$ by ALD into $Co/CoO_x$-embedded N-C nanostructure for a highly efficient and stable bifunctional oxygen electrocatalysis. We employ ALD to maximize heterogeneous catalytic sites by leveraging its unique nature of discrete and self-saturated reactions, which enables tiny $CeO_x$ species introduced throughout the porous precursor framework in a uniform and highly dispersed manner. The hybrid catalysts obtained after ceria ALD followed by pyrolysis at 700 °C nicely preserves the rhombic dodecahedral polyhedron structure of ZIF-67 precursor. The best performing catalyst (Co/NC@Ce15-700) exhibits an ORR onset potential of 0.95 V (0.1 M KOH) and an OER potential of 1.53 V at 10 mA $cm^{-2}$ (1 M KOH) and demonstrates an excellent cyclic and chronoamperometric stability. The remarkable performance and stability of the bifunctional oxygen electrocatalyst is attributed to the reaction-facilitating role of ceria, which activates reactant adsorbates and

transfers the activated intermediates to its immediately neighboring $CoO_x$ species and electronically couples with Co and N species for enhanced electron transfer and catalytic activity. It is additionally noted that a high concentration of trivalent Ce state is readily and continuously restored during ORR/OER for an uninterrupted activation of reactants, which should have not only facilitated reaction kinetics and but also enabled the undeteriorated reaction. The high-surface-area MOF-derived structure and metal-N moieties and oxygen vacancy sites on $CoO_x$ should have additionally contributed to the performance. This work suggests an effective strategy for the synthesis of mixed metal/metal oxide-integrated carbon nanostructures as an efficient bifunctional electrocatalysts.

# CHAPTER 5. Ni-O-O-M Bridge Formation for Efficient OER in NiCo LDH-Based Core-Shell Structures

## 5.1 Introduction

With ever increasing energy consumption and carbon emissions, there is an impending demand for highly efficient and economical renewable energy systems.[108] Hydrogen is considered a promising energy medium to address the unpredictable intermittency of renewable energies. Hydrogen is an efficient energy source with high heat value ($1.4\times10^6$ J/kg) and the production of harmless water as a reaction product, which makes it regarded as a promising substitution for the conventional energy resources.[109] Electrochemical water splitting, an effective approach to generate high purity of hydrogen, is composed of two half reactions: hydrogen evolution reaction (HER) and oxygen evolution reaction (OER).[110] OER is the main rate-limiting half-reaction; it exhibits a large overpotential and a slow anodic four-electron transfer process.[111,112] $IrO_2$ and $RuO_2$ have been accepted as the standard OER catalysts because of their excellent catalytic activity in both acidic and alkaline electrolytes.[113–115] However, their high cost, rarity, and unstable performance limit them from being widely deployed.[116]

Recently, transition metal-based 2D layered double hydroxides (LDHs) have attracted great attention for the enhancement of OER performances due to their remarkable tunability of morphology, high specific capacitance, facile synthesis process and low cost.[3,117,118] This material class can be represented by a general formula as $[M^{II}_{1-x}M^{III}_{x}(OH)_2]_{z+}(A^{n-})_{z/n}\cdot yH_2O$, where $M^{II}$ and $M^{III}$ are metallic divalent and trivalent cations, and $A^{n-}$ represents the interlayer anions. When used as electrode materials, the flexible choices of $M^{II}$, $M^{III}$ and $A^{n-}$ in the LDH structure and the variability of interlayer distances allow further improvement of OER performance.[119] However, the LDH family exhibits low electrical conductivity, usually in the range from $10^{-13}$ to $10^{-17}$ S $cm^{-1}$,[120] significantly limiting their OER performance. Moreover, the nanostructure may collapse and undergo a severe aggregation of active species due to the micropores and defects formed during the synthesis process.[121] Therefore, developing

a synthetic technique that can leverage the benefits of LDHs while avoiding the structural degradation is essential for enabling efficient and durable electrocatalysis.

A hierarchical three-dimensional (3D) carbon structures are considered as a promising framework to facilitate electrolyte ion transport, maximize the surface area, and provide efficient electronic and ionic transport through the electrode. In addition, the 3D structure is expected to deter the aggregation while providing more of catalytically active edge sites. Much efforts have been devoted to design 3D LDH configurations for efficient OER activity.[122–124] However, most of them require a tedious and costly synthesis process, limiting their commercial viability.

In this study, we present a simple and effective strategy for the preparation of high-performance 3D core-shell LDH electrocatalysts derived from a metal-organic framework (MOF) substrate. A hierarchical BDC@CoNi-LDH electrocatalyst with a highly dispersed 3D core (Co-BDC MOF)-shell (CoNi-LDH) structure is prepared via a one-step hydrothermal method at 120 °C, using Ni foam as the substrate. The dissolution of the inner core and the precipitation of cations caused by the release of hydroxide from urea during the hydrothermal process result in the formation of a shell made of numerous LDH nanoplates on the outer layer of Co-BDC MOF.[125] The resultant 3D tetragonal structure with numerous nanoplate cloths exhibits a low overpotential of 280 mV at 100 mA $cm^{-2}$ and an excellent cyclability for OER. A series of *quasi-operando* characterization by Raman, Fourier transform infrared spectroscopy and X-ray photoelectron spectroscopy along with *ex situ* X-ray absorption spectroscopy are further performed to reveal intrinsic active sites and provide a mechanistic interpretation of OER process in the 3D catalyst. This work suggests an effective and simple strategy for the development of template-directed core-shell electrocatalysts.

## 5.2 Experimental Section

### *5.2.1* Materials and reagents

Cobalt nitrate hexahydrate ($Co(NO_3)_2•6H_2O$, 99.8%), nickel nitrate hexahydrate ($Ni(NO_3)_2•6H_2O$, 99.8%), urea ($NH_2CONH_2$, 98.0%), N,N-Dimethylformamide (DMF, 99.8 %) and potassium hydroxide (KOH) were purchased from Sigma-Aldrich. Ethanol

($C_2H_5OH$, 99.5%), $IrO_2$ (99.9 %) and terephthalic acid ($C_8H_6O_4$, 98+ %) were supplied by Alfa Aesar. All chemicals were used as received without further purification.

### *5.2.2 Synthesis of BDC@CoNi-LDH based nanoparticles*

In a typical procedure, nickel foam (~ 1 cm × 2 cm) was soaked into 2 M HCl in an ultrasonic cleaner for 15 min to remove the surface oxidizer. Then it was washed with deionized water and ethanol for 10 min and dried under $N_2$ flow. 166 mg of terephthalic acid and 300 mg urea was first dissolved in 20 mL DMF and 20 mL deionized water. $Co(NO_3)_2$• $6H_2O$ (290 mg), $Ni(NO_3)_2$• $6H_2O$ (290 mg) was dissolved in turn into previous solution. The mixed aqueous solution together with the as-prepared nickel foam was transferred into a 40 mL Teflon-lined stainless-steel autoclave and heated in an oven at 120 °C for 12 h. After cooling down to room temperature, the resultant brown sample was washed with deionized water and ethanol with ultrasonic cleaner for 15 min to remove the residual reactants and dried at 80 °C for 12 h in the air.

### *5.2.3 Synthesis of Co-BDC@Ni-LDH nanoparticles*

290 mg of $Co(NO_3)_2$• $6H_2O$ was dissolved into 20 mL deionized water (solution A). 155 mg of terephthalic acid was dissolved into 20 mL DMF (solution B). Then, solution A and solution B was mixed and ultrasonic for 30 mins at room temperature (Solution C). Solution C together with cleaned Ni foam (1 cm × 2 cm) was transferred into Taflon-lined stainless-steel autoclave and heated in an oven at 120 °C for 12 h. The resultant samples were collected and rinsed with water for 30 minutes to get Co-BDC@Nickel foam. 290 mg of $Ni(NO_3)_2$• $6H_2O$, 300 mg of urea was dissolved into 40 mL DI water (solution D). At last, solution D and Co-BDC@Nickel foam was added into autoclave and heated in an oven at 120 °C for 12 h. The products were washed with DI water and ethanol and dried at 80 °C for 12 h in the air.

### *5.2.4 Synthesis of Ni-BDC@Co-LDH nanoparticles*

The synthesis procedure is the same as Co-BDC@Ni-LDH nanoparticles, switching the order of Co and Ni precursors for the making of the BDC and LDH structure instead.

### *5.2.5 Synthesis of CoNi-LDH nanoparticles*

$Co(NO_3)_2 \cdot H_2O$ (290 mg), $Ni(NO_3)_2 \cdot 6H_2O$ (290 mg) and urea (300 mg) was dissolved in 40 mL deionized water and sonicated for 30 min to get a homogeneous solution. The aqueous solution together with the as-prepared nickel foam was transferred into a 40 mL Teflon-lined stainless-steel autoclave and heated in an oven for 12 h at 120 ℃. After cooling down to room temperature, the resultant sample was washed with deionized water and ethanol for 15 min to remove the residual reactants and dried at 80 ℃ for 12 h in air.

### *5.2.6 Physical characterization*

The morphology and microstructure were characterized by SEM (Zeiss Gemini SEM 500, 3 kV) and TEM (Philips CM300 FEG system 200 kV). XRD patterns were recorded using PAN analytical X'Pert PRO with Co K$\alpha$ radiation ($\lambda$ = 1.78897 Å) at the step size of 0.02° and scan rate of 0.04° $s^{-1}$, and the resulting data was further converted to Co K$\alpha$ radiation ($\lambda$ = 1.5418 Å) for the analysis. FTIR were recorded on a Nicolet 380 FT-IR Spectrometer with the wave numbers from 400 to 4000 $cm^{-1}$ by dispersing samples onto a crystal attenuated total reflectance (ATR) accessory. XPS was performed on a PHI Quantum 2000 system using a focused, monochromatic Al K$\alpha$ X-ray (1486.6 eV) source for excitation and a spherical section analyzer (200 $\mu$m diameter X-ray beam incident to the surface normal; detector set at 45°). Raman spectra were obtained on an iXR Raman spectrometer (Thermo Scientific).

### *5.2.7 Electrochemical Characterization*

The OER characterization was performed in a standard three-electrode glass cell by a potentiostat (SP-200, Bio-Logic SAS) at room temperature. The as-prepared samples supported on nickel foam was used as the working electrode while a graphite rod and an Ag/AgCl (1 M KOH) electrode were used as the counter and reference electrodes, respectively. All potentials were expressed with respect to reversible hydrogen electrode according to the Nernst equation:

$$E^{\theta} = E_{Ag/AgCl} + 0.0591 \times pH + E^{\theta}_{Ag/AgCl}$$

where $E_{Ag/AgCl}$ and $E^{\theta}_{Ag/AgCl}$ are applied potential and the standard potential of the Ag/AgCl reference electrode, respectively. The overpotential ($\eta$) was calculated by $\eta$ (V) = E (RHE) - 1.23V. $O_2$ flow was fed into the 1 M KOH electrolyte for > 30 min to have the solution saturated with each gas before testing. The solution was put on a magnetic stirrer and stirred under 500 rpm $min^{-1}$ to remove the generated surface oxygen to avoid the surface exfoliation. All LSV polarization curves were corrected by eliminating iR drop with respect to the ohmic resistance of the solution. EIS measurement was tested by the potentiostat (SP-200, Bio-Logic SAS) with an AC amplitude applied of 10 mV at different overpotentials in the frequency range of 0.1 Hz – 100 kHz. XAS were taken in total electron yield mode at beamline 6.3.1 of the Advanced Light Source. Quasi-operando XRD, XPS, Raman and ATR FTIR electrochemical operation were carried out under different electrochemical potential for 15 min to obtain the surface chemical states and structural information of the samples. Before all the LSV tests, the electrodes were cycled at 100 mV $s^{-1}$ until reproducible cyclic voltammograms were obtained.

The Tafel slope was calculated by the following equation:

$$\eta = b \times logJ + a$$

where J was obtained with 100 % iR correction, $\eta$ is the overpotential and b is the Tafel slope. The ECSA was characterized by cyclic sweep with various scan rates (2 to 10 mV $s^{-1}$ at an interval of 2 mV $s^{-1}$) in a small range where no faradaic reaction occurs (1.13 –1.18 V). The ECSA was calculated according to the following equation:

$$ECSA = \frac{C_{area} \times A}{C_{ref}}$$

where $C_{area}$ is the slope of $J_{anodic}$ - $J_{cathodic}$ vs. scan rate graph, $A$ the geometric area of the electrode and $C_{ref}$ the areal capacitance of flat electrode. TOF is calculated by the following equation:

$$TOF = (j \times A)/(4 \times F \times n)$$

where $j$ is the measured current density at the overpotential of 350 mV, F is Faraday's constant (96485 C/mol), $n$ is the number of moles of the active metal atoms (0.002 mol) supported on the nickel foam.

## 5.3 Results and Discussion

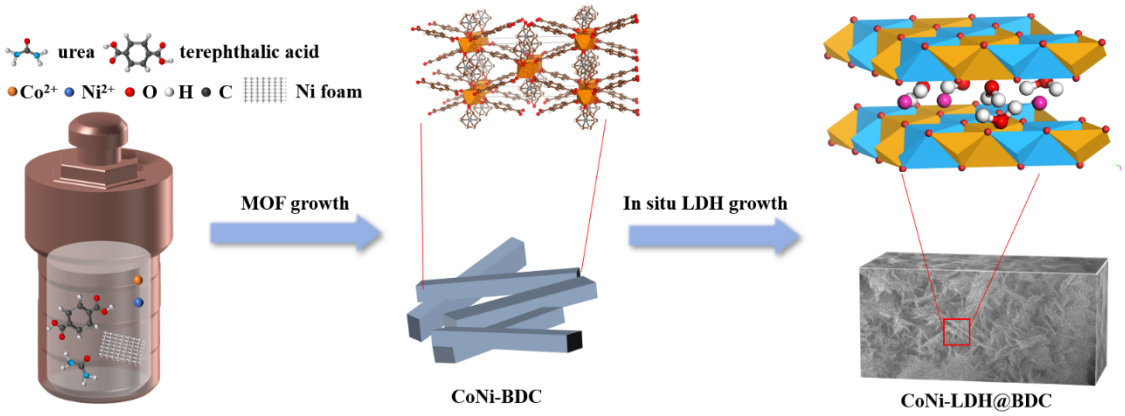


**Figure 5.1** Schematic illustration of the synthesis process for hierarchical BDC@CoNi-LDH core shell structure.

The schematic diagram of the fabrication process of BDC@CoNi-LDH is illustrated in **Figure 5.1**. The BDC@CoNi-LDH core-shell microstructures is synthesized directly via a one-step hydrothermal reaction. In brief, $Co(NO_3)_2$• $6H_2O$ and $Ni(NO_3)_2$• $6H_2O$ are dissolved in a solution of DMF and water containing terephthalic and urea. The mixed solution is then sealed in a hydrothermal vessel at 120 °C for 12 h. The LDH structure is finally obtained while the overall geometry of Co-BDC MOF is preserved as the inner (core) structure.[126] Two additional MOF-derived LDH structures are synthesized: One by growing Ni-LDH on Co-BDC MOF (namely, Co-BDC@Ni-LDH), and the other growing Co-LDH on Ni-BDC MOF (namely, Ni-BDC@Co-LDH). A detailed description of synthesis procedure is provided in the Experimental.

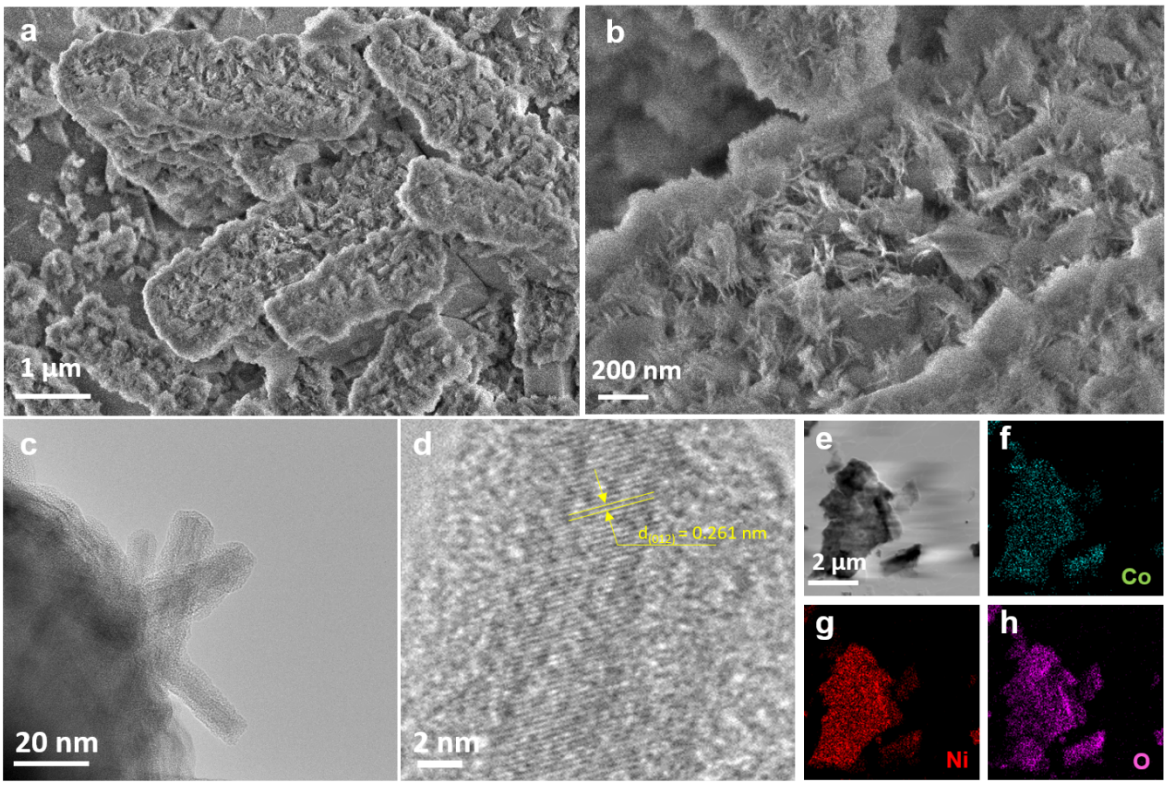


**Figure 5.2** (a,b) SEM image, (c) TEM image, (d) HR-TEM image, (e-h) EDS elemental mapping of BDC@CoNi-LDH.

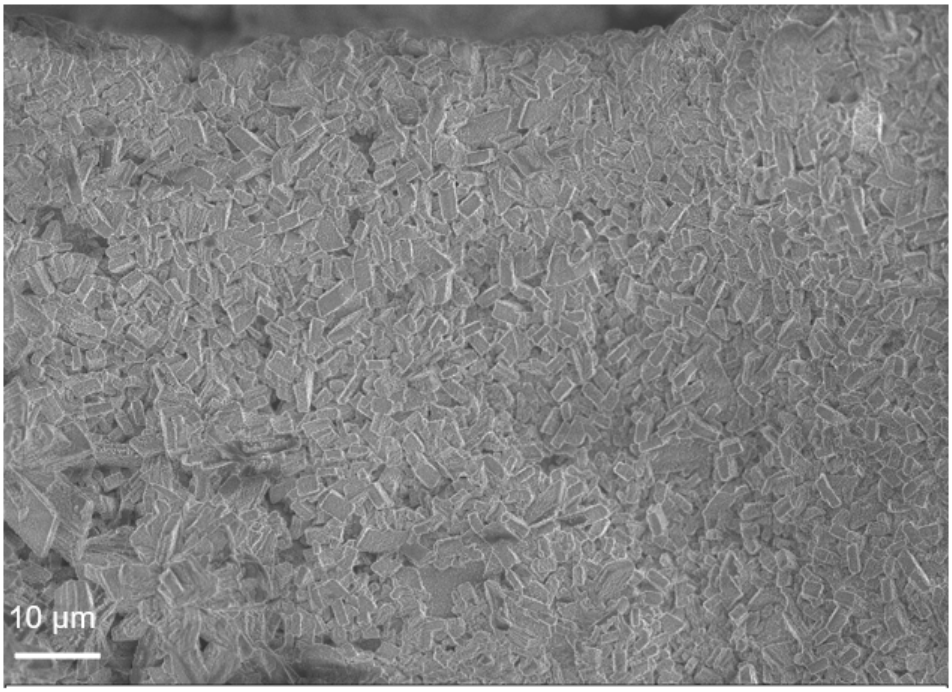


**Figure 5.3** SEM image of BDC@CoNi-LDH micro core-shell structures.

The morphology of BDC@CoNi-LDH imaged by scanning electron microscope (SEM) is shown in **Figure 5.2a** and 5.2b and Figure 5.3. The as-prepared samples clearly show 3D polyhedron configuration, inheriting the structure of Co-BDC MOF. A zoomed-in SEM image (Figure 5.2b) reveals that nanoplate arrays with the thickness of ~ 10 nm are formed on the surface of Co-BDC MOF substrate, resulting in an overall core-shell structure where the Co-BDC MOF structure is surrounded by LDH nanostructures.

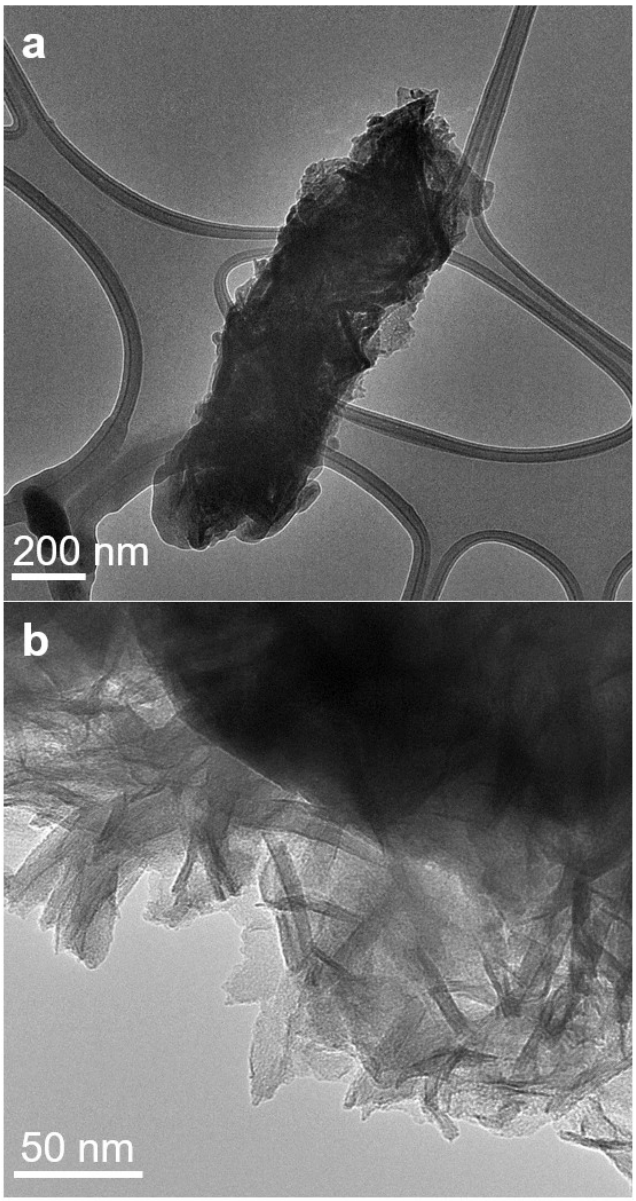


**Figure 5.4** TEM images of BDC@CoNi-LDH. (a) Fine LDH structures are surrounding a rod-like BDC structure. (b) A zoomed-in image focusing on LDH nanosheets.

The transmission electron microscopy (TEM) image in Figure 5.4a further reveals that nanoplates of LDH are formed on the surface of a rod-like BDC-based structure, forming a core-shell structure. The ultrathin nature of the nanoplates (~ 10 nm) shown in Figure 5.2c and Figure 5.4b are expected to be favorable for reactant diffusion during the

electrode reactions.[127] High-resolution TEM (HRTEM) image (Figure 5.2d) displays clear lattice fringes with an interplanar distance of 0.26 nm, corresponding to (0 1 2) planes of hexagonal CoNi-LDH.[41] Energy-dispersive X-ray spectroscopy (EDS) elemental maps in Figures 5.2e-h indicate that Co, Ni, and O species are uniformly dispersed throughout the structure; an EDS spectrum is also provided in Figure 5.5.

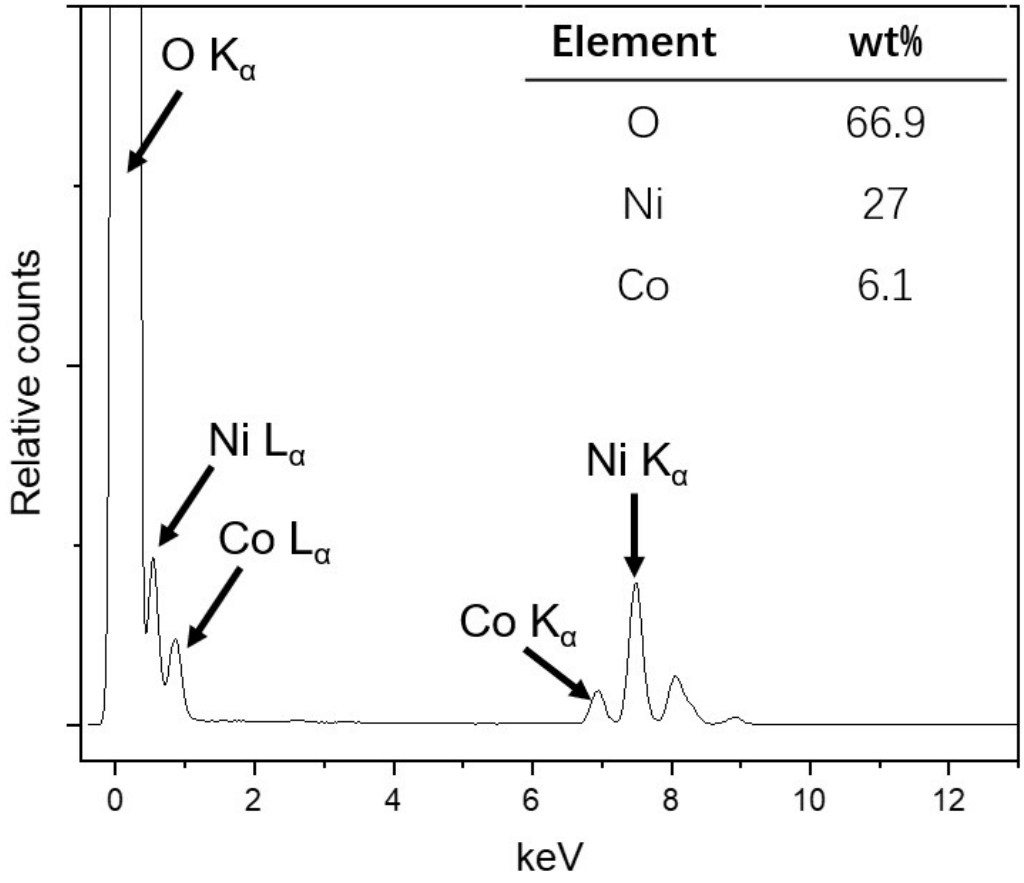


**Figure 5.5** A TEM-EDS mapping spectrum of BDC@CoNi-LDH.

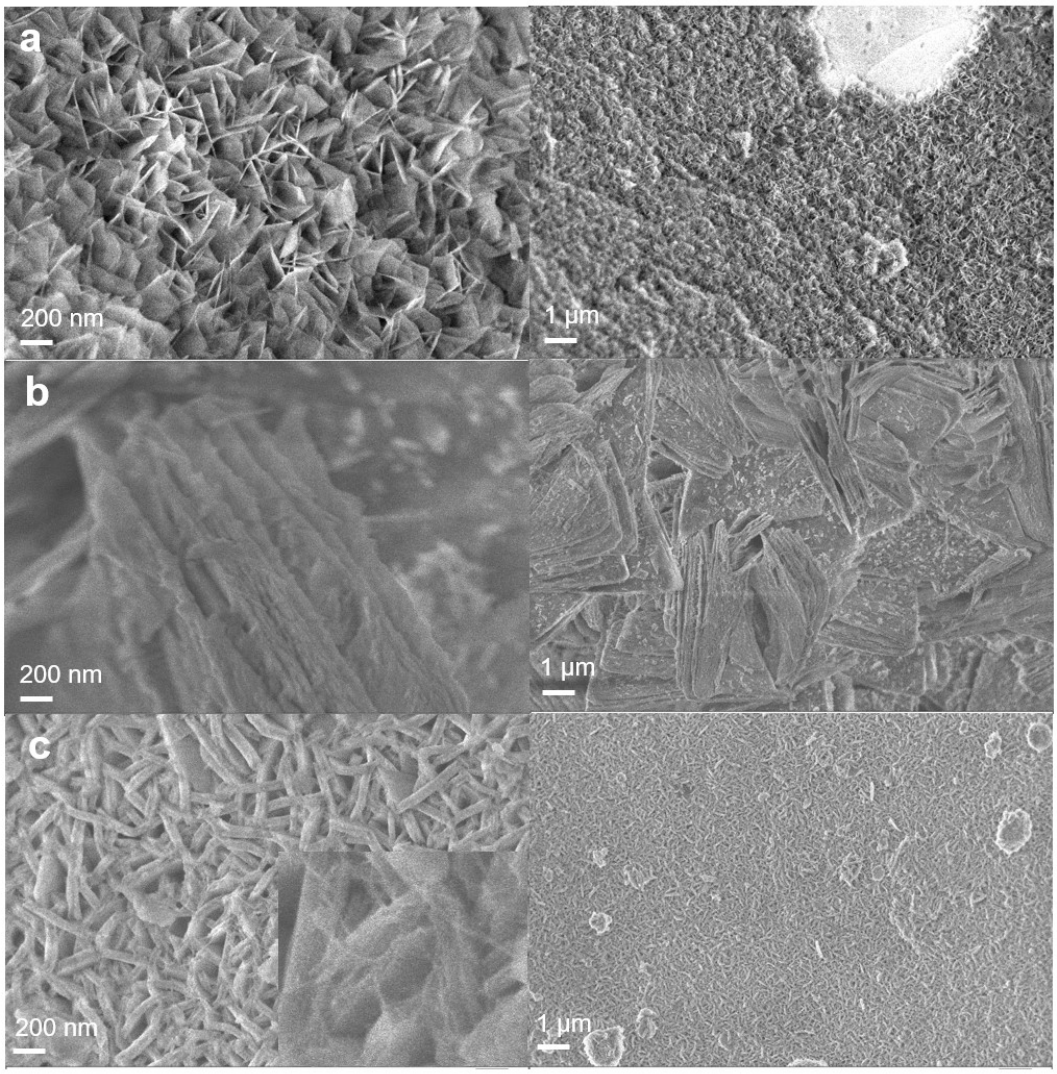


**Figure 5.6** SEM image of (a) CoNi-LDH, (b) Co-BDC@Ni-LDH and (c) Ni-BDC@Co-LDH (Inset: zoomed in image).

On the other hand, the other two BDC@LDH structures (i.e., Co-BDC@Ni-LDH and Ni-BDC@Co-LDH) do not show the fine LDHs on the BDC structure, which is visible in BDC@CoNi-LDH (Figure 5.6b-c). Instead, they reveal multilayer features in the structure (as opposed to a core-shell structure), suggesting a possible formation of LDHs *within* the BDC structure, rather than *onto* the structure.

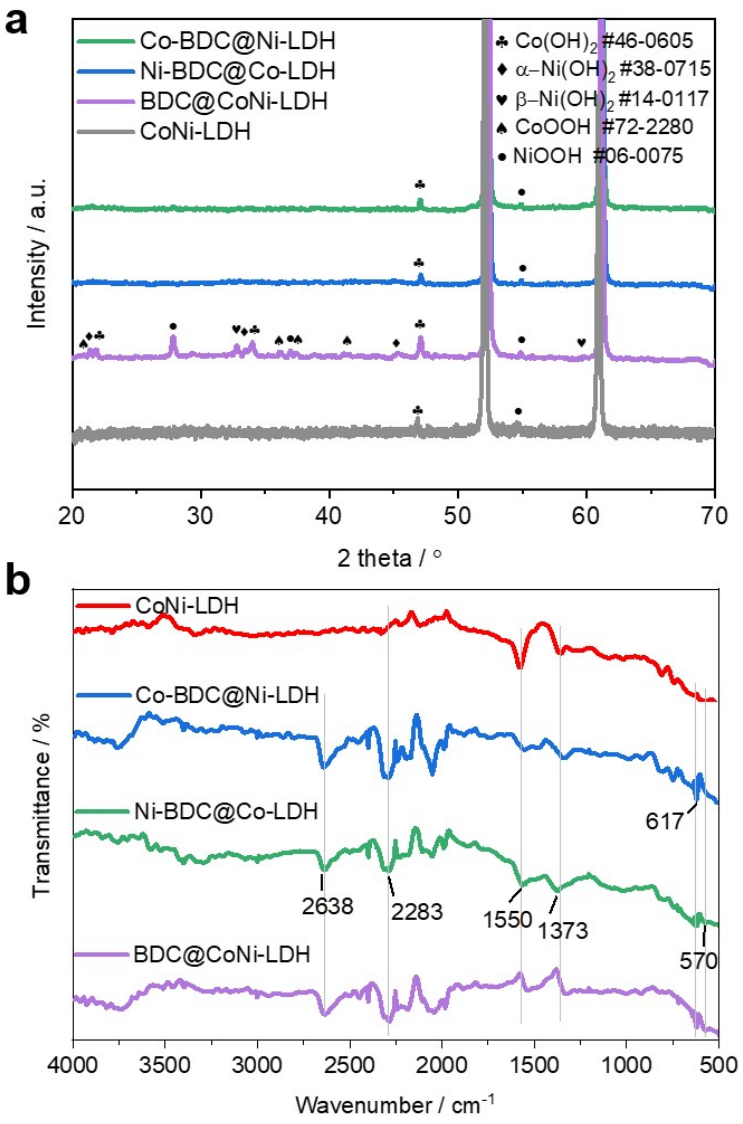


**Figure 5.7** (a) XRD patterns and (b) FT-IR spectra of as-prepared LDH@BDC series.

The structural information of as-prepared samples is obtained by X-ray diffraction (XRD). The peak located at 47.3° in Figure 5.7a can be found in all samples, corresponding to (0 0 12) crystal planes of $Co(OH)_2$ (JCPDS# 46-0605),[128] which originates from CoNi-LDH structure. The peak at 54° is attributed to the (1 0 8) plane of γ-NiOOH (JCPDS# 06-0075).[129] BDC@CoNi-LDH shows additional distinct peaks unlike the other samples. First, the peak located at 2θ = 27.2°, 32.8° and 45.2° can be

assigned to the characteristic peaks of (0 0 6), (0 1 2) and (0 1 5) planes of α-$Ni(OH)_2$, representing the typical hydrotalcite-type structure of LDH (JCPDS# 33-0426/38-0715) while the peak at 22.4° and 59° corresponds to the (0 0 1) and (1 0 2) plane of β-$Ni(OH)_2$ (JCPDS#14-0117).[130,131] $Co(OH)_2$ and $Ni(OH)_2$ are possible active sites for both adsorbing $OH^-$ and releasing $O_2$ molecules, facilitating OER.[132] Moreover, BDC@CoNi-LDH exhibits peaks at 20.7°, 36.1° 37.4° and 43°, which can be indexed to the (1 1 1), (1 0 0), (1 1 0) and (2 1 1) planes of CoOOH (JCPDS# 72-2280).

In the FT-IR spectra of BDC@CoNi-LDH shown in Figure 5.7b, all three BDC-based samples exhibit the peak located at 2638 $cm^{-1}$ and 2283 $cm^{-1}$, corresponding to C-H stretching from aldehyde and isocyanate (N=C=O) vibration stretching mode, respectively. The absence of isocyanate stretching mode in CoNi-LDH (from Figure 5.7b) or BDC structure (from the ref. [133]) suggests that appearance of the isocyanate peak in BDC@CoNi-LDH is caused by a chemical bonding between LDHs and the BDC structure with the help of urea. The peak at 1550 $cm^{-1}$ is assigned to the H-O-H bending vibration from LDH structure[122,134] while the one at ~ 1373 $cm^{-1}$ is associated with the ν3 vibration of $CO_3^{2-}$.[135] Additionally, the peaks at ~ 617 $cm^{-1}$ and 570 $cm^{-1}$ belong to Ni-O-H and Co-O-H bending vibration, respectively.[136,137]

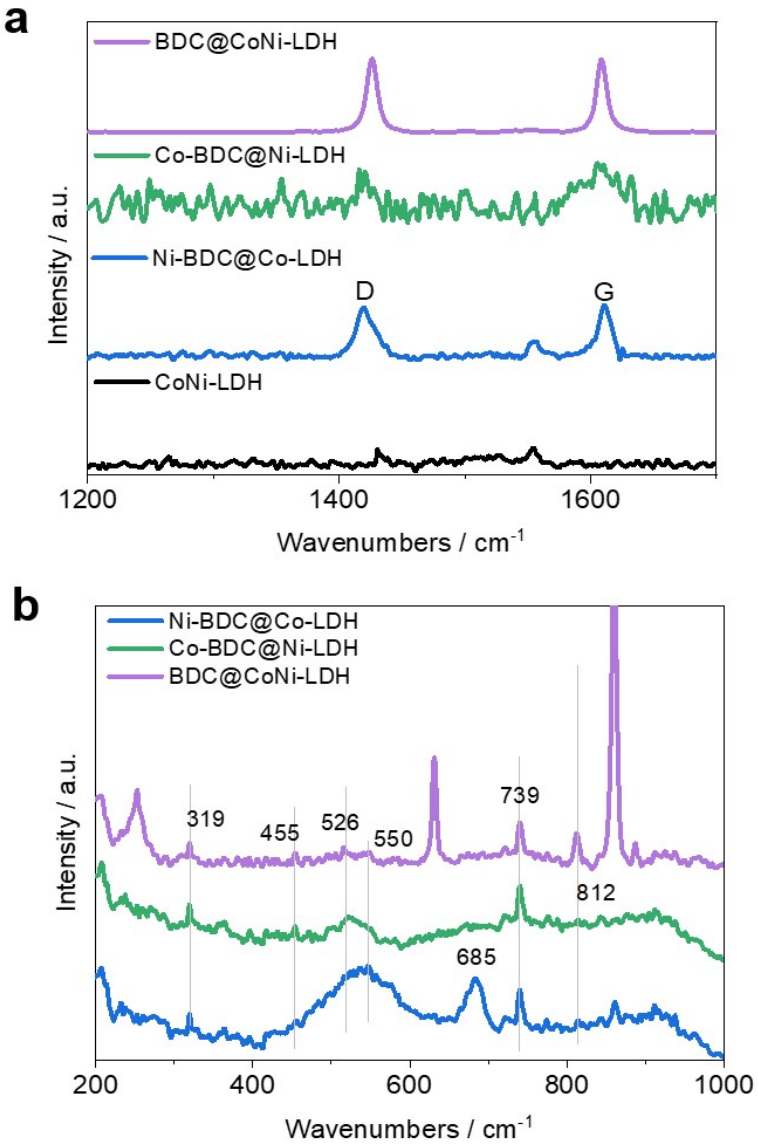


**Figure 5.8** Raman spectra of LDH@BDC series samples to show D and G band peaks (a) and low wavenumber region (b).

Raman spectroscopy is also performed. There is no obvious peak $I_D$ and $I_G$ band detected for CoNi-LDH sample (Figure 5.8a), consistent with the fact that carbon element mostly exists in the form of $CO_3^{2-}$ within the interlayers of LDH structure. On the contrary, both BDC-based samples exhibit certain $I_D$ and $I_G$ band located at ~ 1418 $cm^{-1}$ and 1618 $cm^{-1}$. Significant blue shifts of D and G band can be related with the strain

effect caused by the incorporation of BDC and LDH surface.[138] The $I_D/I_G$ ratio is calculated to be 1.01, 0.9 and 0.95 for BDC@CoNi-LDH, Ni-BDC@Co-LDH and Co-BDC@Ni-LDH, respectively. Their similarity in the $I_D/I_G$ ratio suggests they have a similar level of defect concentrations. Low frequency Raman spectra are additionally obtained (Figure 5.8b) to identify metal oxygen (M-O) vibration environment. The sharp peaks at ~ 631 and 860 $cm^{-1}$ are originated from photobleaching. The peaks at 319, 455 and 526 $cm^{-1}$ are attributed to the M-O vibrations of $Co(OH)_2$ and $Ni(OH)_2$, in accordance with the previously reported Co-Ni systems.[139,140] The 450 $cm^{-1}$ peak is attributed to NiOOH, and those at 739 and 812 $cm^{-1}$ correspond to the stretching mode of benzene ring from BDC substrate.[133,141]

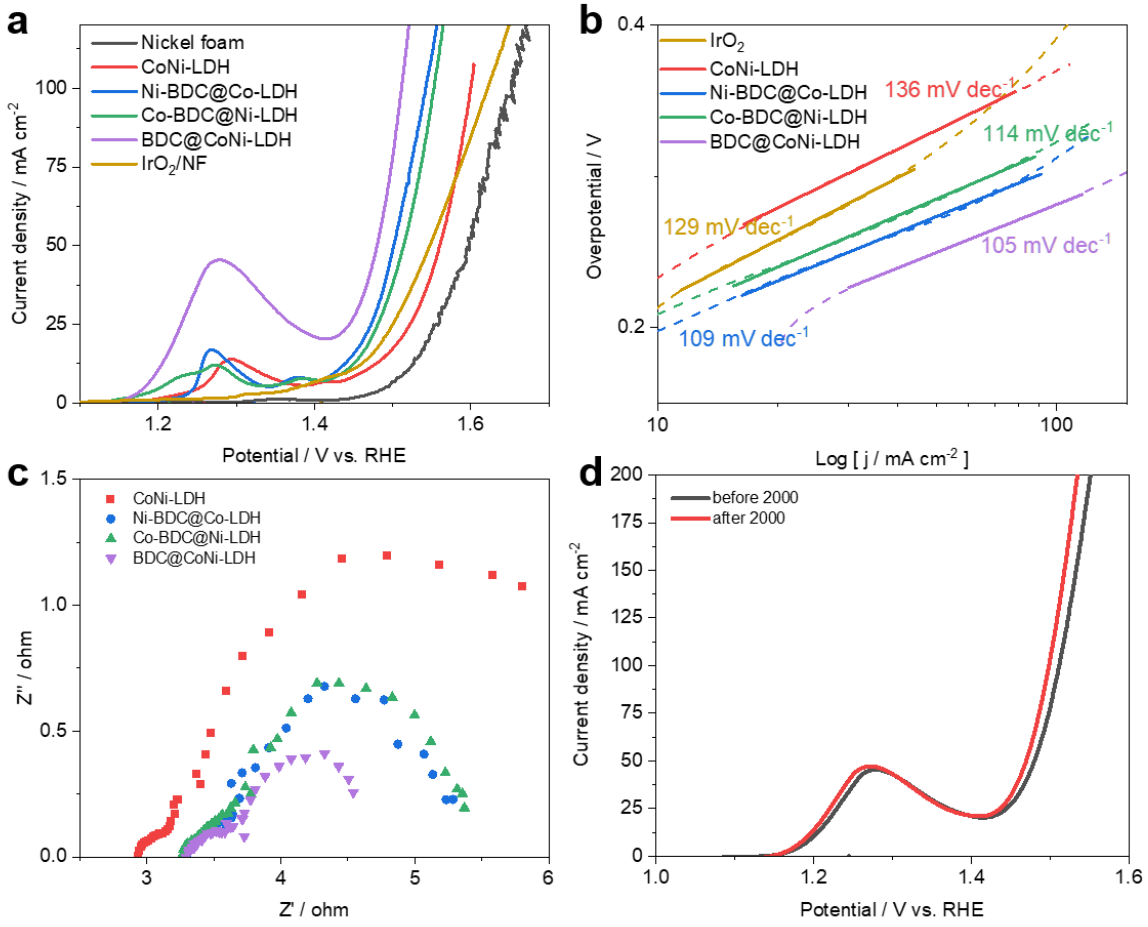

**Figure 5.9** Electrochemical characterization: (a) OER polarization curves, and (b) corresponding OER Tafel slopes of CoNi-LDH, Ni-BDC@Co-LDH, Co-BDC@Ni-LDH, BDC@CoNi-LDH, and IrO2 benchmark, (c) Nyquist plots (potential = 1.53 V vs. RHE) of as-prepared catalysts, (d) OER polarization curves for BDC@CoNi-LDH catalyst before and after 2000 cycles between 1.0 V and 1.8 V at 5 mV s-1.

The electrochemical OER performance of nickel foam, CoNi-LDH, Ni-BDC@Co-LDH, Co-BDC@Ni-LDH, and BDC@CoNi-LDH are examined in 1 M KOH with a standard three-electrode system. As shown in the linear sweep voltammetry (LSV) curve shown in **Figure 5.9a**, BDC@CoNi-LDH sample exhibits the best OER performance; it reaches 100 mA $cm^{-2}$ at a potential as low as 1.53 V vs. RHE, which corresponds to an overpotential of 280 mV.

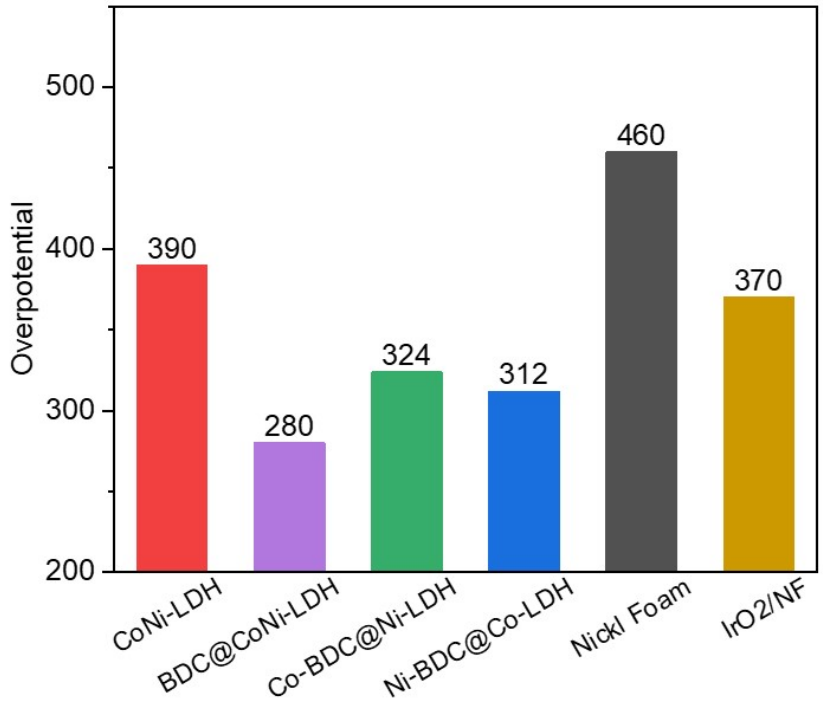


**Figure 5.10** The overpotential at 100 mA $cm^{-2}$ of as-prepared catalysts.

The benchmark $IrO_2$ necessitates an overpotential of 410 mV for the same current density (Figure 5.10). The peak appearing at ~ 1.25 – 1.3 V in the polarization curves is ascribed to the oxidation of Ni in the nickel form.[142] All the BDC@LDH variants exhibit an enhanced performance compared to the bare LDH sample (i.e., CoNi-LDH). The OER kinetics is also assessed by the Tafel plots in Figure 5.9b. BDC@CoNi-LDH possesses the lowest Tafel slope of 105 mV $dec^{-1}$, which is smaller than those of CoNi-LDH (136 mV $dec^{-1}$), Co-BDC@Ni-LDH (115 mV $dec^{-1}$) and Ni-BDC@Co-LDH (109 mV $dec^{-1}$), reflecting its fast OER kinetics. Another important indicator of intrinsic activity of a catalyst is turnover frequency (TOF); a greater TOF signifies a better atom consumption efficiency and faster kinetics per active site. Assuming Co and Ni atoms are all active during the OER process, TOFs are calculated for all

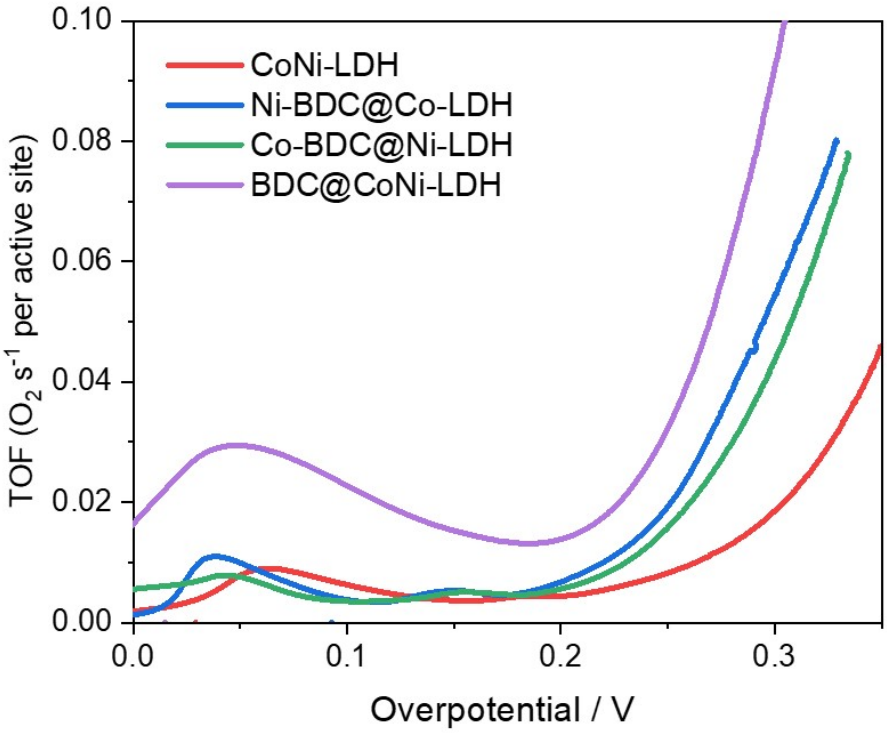


**Figure 5.11** Turnover frequency curves of different catalysts.

samples at an overpotential of 300 mV vs. RHE. As shown in Figure 5.11, BDC@CoNi-LDH shows the highest TOF (0.09 $s^{-1}$) among all samples, reflecting that the sample has faster kinetics toward OER. Additionally, electrochemical impendence spectroscopy (EIS) analysis is performed at 1.53 V vs. RHE in the frequency range of 100 kHz – 0.01 Hz, to understand the reaction kinetics of OER. The resulting Nyquist plots are provided in Figure 5.9c. BDC@CoNi-LDH shows the smallest arc size, again indicating a more efficient charge transfer during OER. It is noted that there are two small arcs, among which the smaller one at a higher frequency range is likely originated from electrolyte conduction since the size of the smaller arc is negligent of the overpotential provided during the measurement. The OER LSV curves of BDC@CoNi-LDH before and after 2,000 CV cycles (Figure 5.9d) indicates its excellent electrochemical stability. The overpotential becomes even slightly smaller after 2,000 cycles.

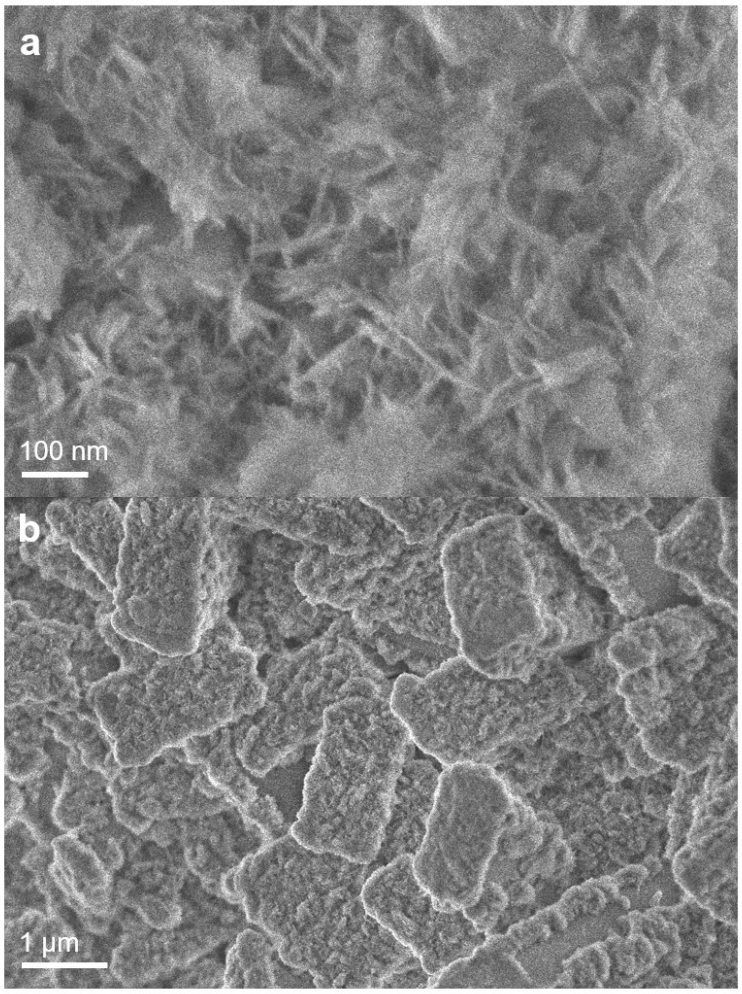


**Figure 5.12** SEM image of BDC@CoNi-LDH after 2,000 cycles between 1.2 – 1.8 V vs. RHE.

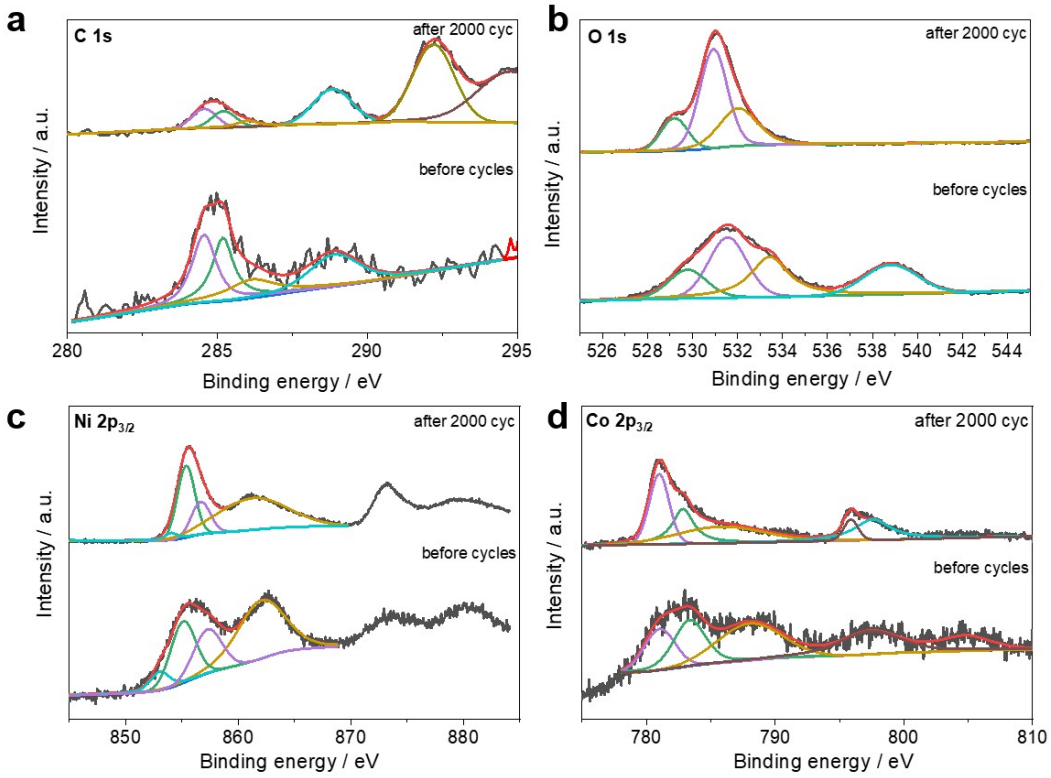


**Figure 5.13** XPS spectra of sample BDC@CoNi-LDH before and after cyclic durability measurement (a) C 1s, (b) O 1s, (c) Ni $2p_{3/2}$, (d) Co $2p_{3/2}$.

As shown in Figure 5.12, the morphology of the sample also remains virtually unchanged after 2,000 cycles. However, the samples show a change in surface chemistry as confirmed by XPS (Figure 5.13). The slightly enhanced OER performance after 2000 cycles is partially ascribed to the increase of oxygen defects, as indicated by the O 1s peak at ~531 eV.

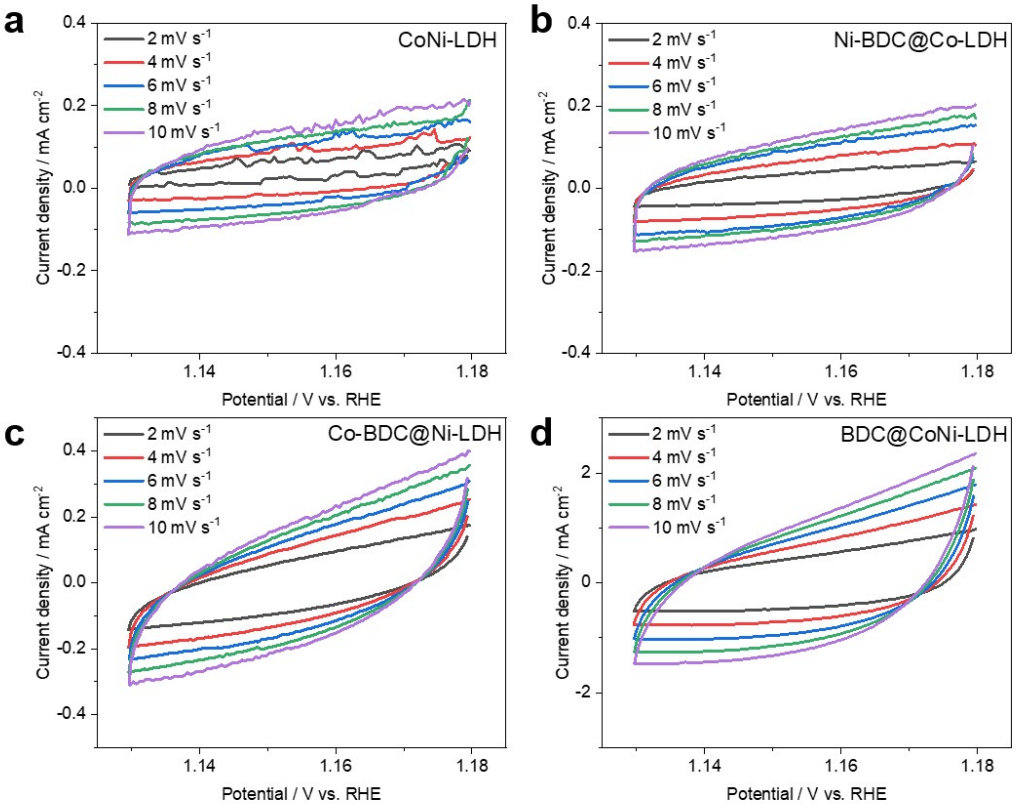


**Figure 5.14** ECSA measurement of (a) CoNi-LDH, (b) Ni-BDC@Co-LDH, (c) Co-BDC@Ni-LDH, and (d) BDC@CoNi-LDH.

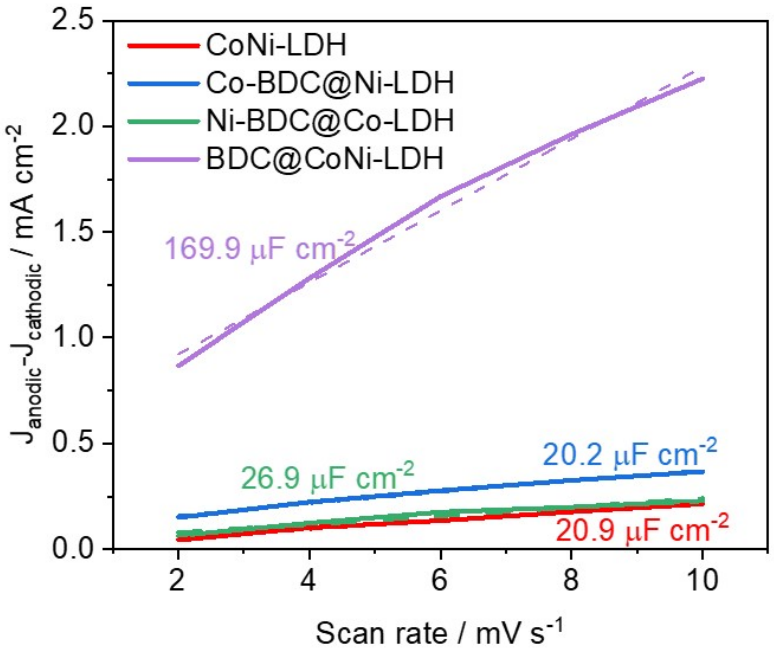


**Figure 5.15** Quantification of double layer capacitance based on the CVs.

**Table 5. 1** ECSA determined from $C_{dl}$.

| | **$C_{dl}$ (μF cm$^{-2}$)** | **ECSA (cm$^2$)** |
|---|---|---|
| CoNi-LDH | 20.9 | 0.131 |
| Co-BDC@Ni-LDH | 20.2 | 0.126 |
| Ni-BDC@Co-LDH | 26.9 | 0.168 |
| BDC@CoNi-LDH | 169.9 | 1.062 |

The electrochemically active surface areas (ECSA) are examined using the calculated double-layer capacitance ($C_{dl}$) to further explain the improved OER catalytic activity of as-prepared samples. As demonstrated in Figures 5.14 and 5.15, $C_{dl}$ of BDC@CoNi-LDH is determined to be 169.9 $\mu$F cm$^{-2}$, which is significantly higher than those of CoNi-LDH (20.9 $\mu$F cm$^{-2}$), Co-BDC@Ni-LDH (20.2 $\mu$F cm$^{-2}$) and Ni-BDC@Co-LDH (26.9 $\mu$F cm$^{-2}$). The quantified ECSA of BDC@CoNi-LDH is 1.062 cm$^2$ (Table 5.1); its high ESCA indicates that it possesses large exposed active area than the others, further making it favorable for OER.

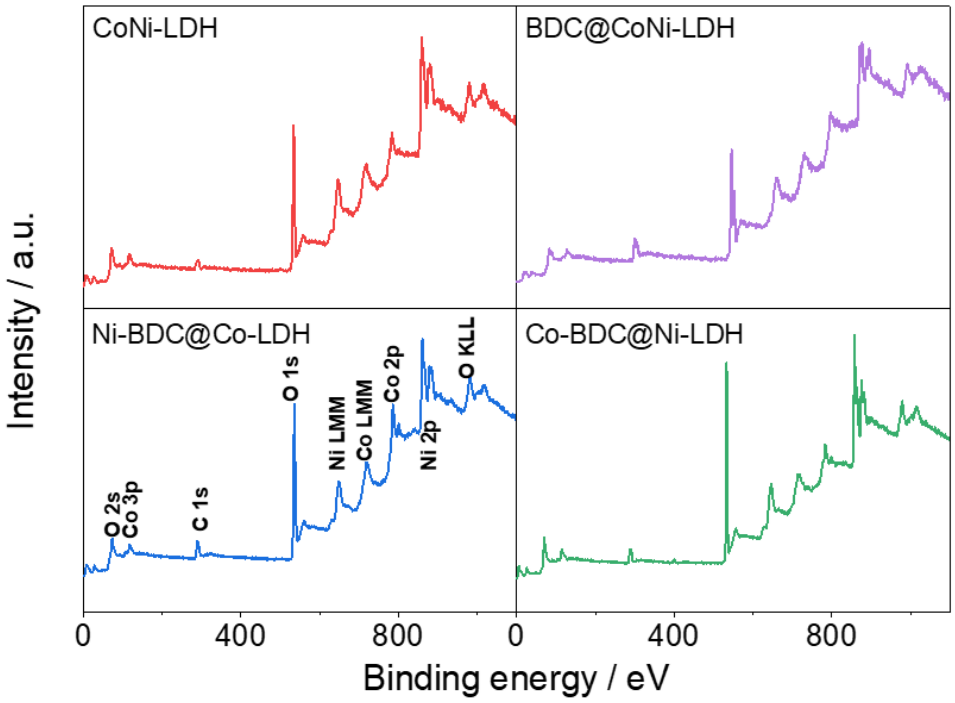


**Figure 5.16** XPS survey spectra of as-prepared samples.

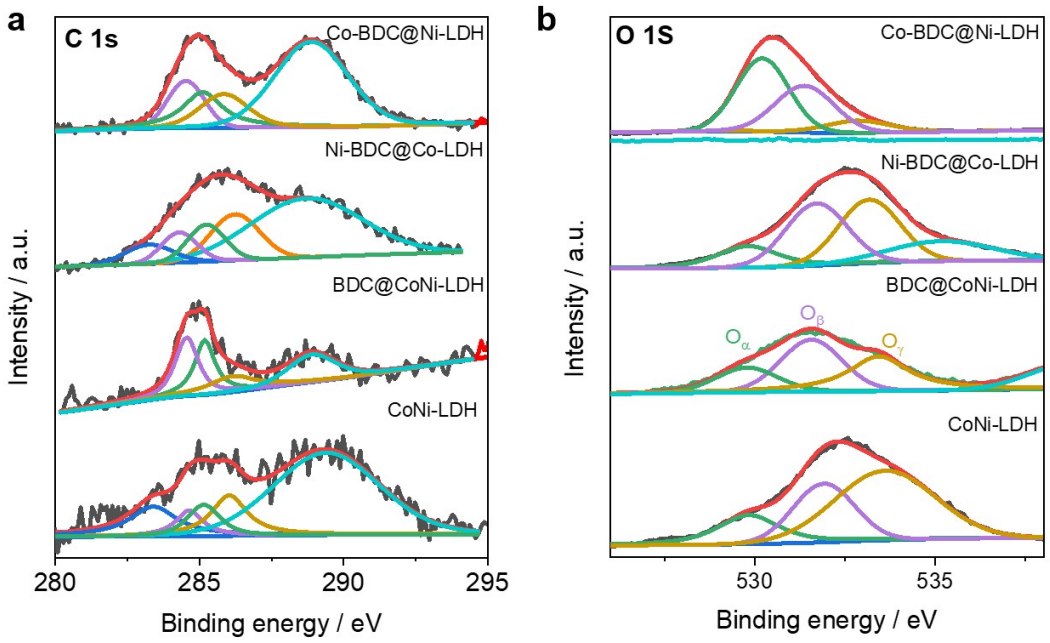


**Figure 5.17** High-resolution XPS spectra of as-synthesized samples. (a) C 1s, and (b) O 1s peaks.

X-ray photoelectron spectroscopy (XPS) analysis is performed to explore surface chemistry and possibly to reveal the electrocatalytically active sites. The survey spectra (Figure 5.16) confirm the existence of Co, Ni, O and C on the surface of all samples. The C 1s spectra (Figure 5.17a) are mainly deconvoluted into four peaks, representing C=C (284.7 eV), C-O (285.5 eV), C=O (286.3 eV) and O-C=O (288.5 eV), respectively.[143,144] Additionally, the extra peak located at ~ 283.0 eV from CoNi-LDH and Ni-BDC@Co-LDH can be related to C-Ni,[145,146] which originated from nickel foam and Ni-BDC. The greatly decreased C=O peak intensity for BDC@CoNi-LDH compared to other samples suggests that C=O acted as a nucleation center for the growth of LDH on the surface of BDCs. The O 1s spectra (Figure 5.17b) are deconvoluted into $O_\alpha$ (529.7 eV), $O_\beta$ (531.7 eV), and $O_\gamma$ (533.4 eV), corresponding to the lattice oxygen in M-O (M: Co or Ni), surface oxygen vacancies, and surface adsorbed oxygen containing species, respectively.[147] The peak located at 535.4 eV for Ni-BDC@Co-LDH belongs to the

molecular water. It is noted that the $O_\beta$ content of BDC@CoNi-LDH is 41.5%, higher than those of CoNi-LDH (27.8%), Ni-BDC@Co-LDH (36.8%), and Co-BDC@Ni-LDH (33.3%). This is well aligned with OER performance because oxygen vacancy is widely known to act as an active site for OER.

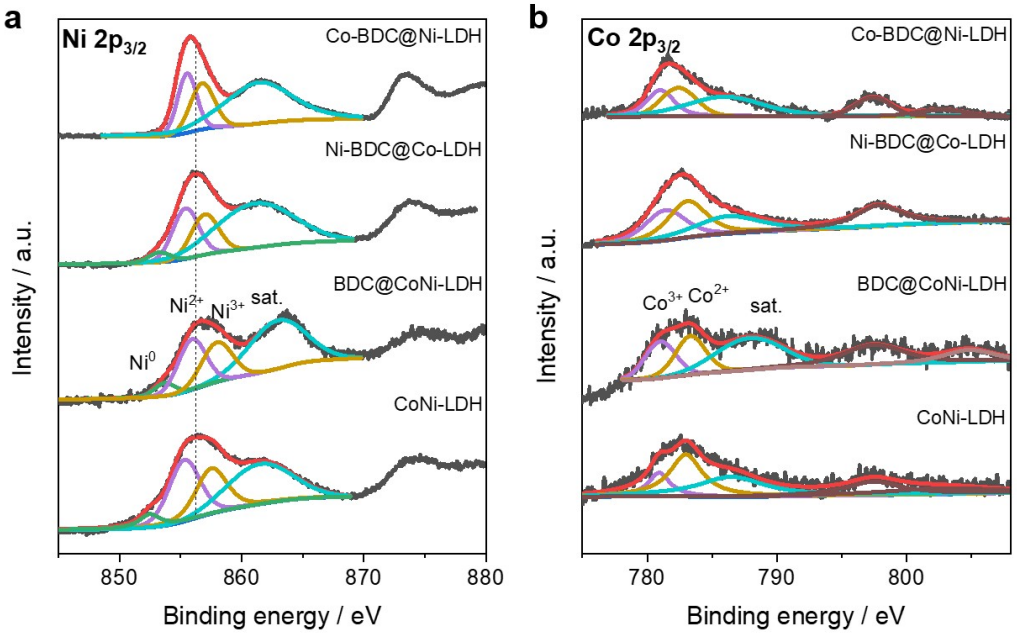


**Figure 5.18** High-resolution XPS spectrum of as-synthesized LDH based samples. (a) Ni 2p3/2, (b) Co 2p3/2.

The high-resolution Ni 2p spectra (Figure 5.18a) are split into three peaks at 852.8, 855.5, and 857.5 eV, being attributed to metallic Ni, $Ni^{2+}$ and $Ni^{3+}$ species, respectively.[109] The shakeup satellite peak centered at 862 eV is also identified. No significant difference is observed in the nickel valence states among the samples. The broader width of $Ni^{3+}$ peak for BDC@CoNi-LDH suggests the existence of $\gamma$-NiOOH, which is believed to be beneficial to the OER performance.[148] Noteworthy, the Ni 2p spectrum of BDC@CoNi-LDH shows a slight shift to the higher binding energy by 0.2 eV compared to that of CoNi-LDH, indicating the regulated local electronic interaction and the partial electron transfer from Ni to Co.[41,149,150] As shown in Figure 5.18b, the Co $2p_{3/2}$ peak can be deconvoluted into $Co^{3+}$ (781.0 eV) and $Co^{2+}$ (783.4 eV), accompanied by the satellite

peak at 787.5 and 803.2 eV, in accordance with literature.[79,80] The $Co^{3+}/Co^{2+}$ ratio for BDC@CoNi-LDH is calculated to be 0.87, while for CoNi-LDH, Ni-BDC@Co-LDH, and Co-BDC@Ni-LDH, it is 0.37, 0.82 and 0.86, respectively. The high valence state of Co could be additionally beneficial to the OER kinetics.[151]

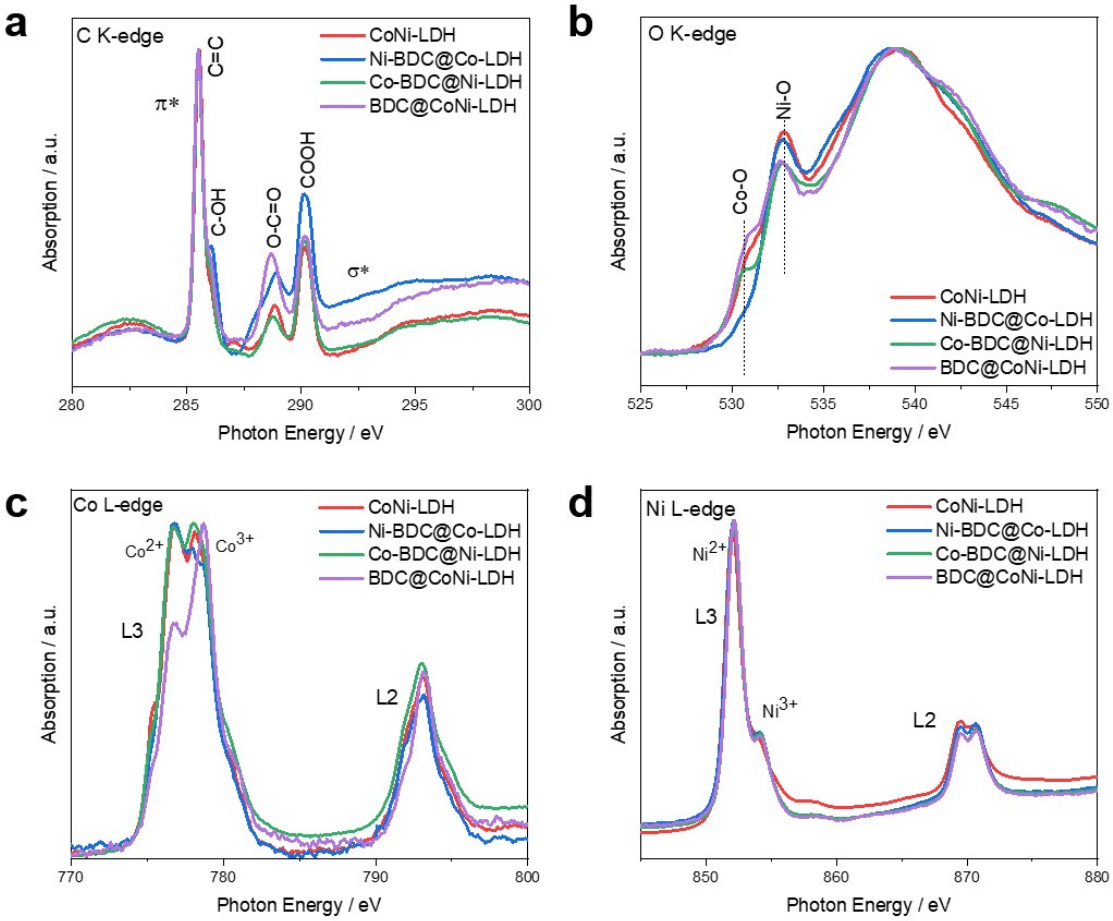


**Figure 5.19** Normalized XAS spectra of CoNi-LDH, Ni-LDH@Co-BDC, Co-LDH@Ni-BDC, and BDC@CoNi-LDH. (a) C K-edge, (b) O K-edge, (c) Co L-edge and (d) Ni L-edge.

To further study the effect of interatomic bonding and cationic valence states on OER activity, X-ray absorption spectroscopy (XAS) is additionally performed. **Figure 5.19a** shows the polarization-dependent C K-edge spectra of as-prepared samples. The spectra

exhibit a strong transition mode of C 1s → $\pi^*$ at ~ 285.5 eV and a broad 1s → $\sigma^*$ at ~ 292.0 eV.[152] The features at ~ 285.5 eV, 288.6 eV, and 290.0 eV are attributed to C=C, O-C=O, and C-OH bonding, respectively.[153] The O K-edge spectra are presented in Figure 5.19b. The features between ~ 529 and 535 eV reflect the structure of the empty electronic states from O 1s electronic level to O 2p orbitals that is hybridized strongly with the transition metal 3d orbitals.[154] The peak at ~530.6 eV (Co 3d/O 2p) for BDC@CoNi-LDH is stronger and exhibits a positive shift by ~0.2 eV compared to that of CoNi-LDH, indicating Co species are partially oxidized in BDC@CoNi-LDH. Meanwhile, a distinct drop in the peak intensity at 532.8 eV and a negative shift by ~ 0.2 eV from BDC@CoNi-LDH is generally attributed to the formation of oxygen vacancies and the weakening of Ni 3d and O 2p hybridization.[155,156] This will facilitate the adsorption of $OH^-$ to the active site (i.e., oxygen vacancies and Ni sites), thus increasing the interactions between surface metal ions and adsorbed intermediates. The L-edge spectra (Figures 4c and 4d) are useful for the analysis of transition metal d orbitals, as the 2p → 3d L-edge transition is a dipole-allowed excitation.[157] As a result of 2p spin-orbital coupling interaction, the Co L-edge (Figure 5.19c) split into two regions: one in a lower energy L3-edge ($2p_{3/2}$ → 3d) at ~ 778 eV and the other in a higher energy L2-edge ($2p_{1/2}$ → 3d) at ~ 793 eV. The L3 edge peak is further split into a mixture of tetrahedrally coordinated $Co^{2+}$ and octahedrally coordinated $Co^{3+}$.[158] BDC@CoNi-LDH shows a markedly intensified peak in the high energy region (779.6 eV), suggests an increase of $Co^{3+}/Co^{2+}$ ratio. Furthermore, the Ni L-edge X-ray absorption (Figure 5.19d) also indicates that BDC-based samples have a higher Ni valance state than that of CoNi-LDH. The XAS spectra are consistent with the electrochemical results that BDC@CoNi-LDH possesses a higher OER activity, which are mainly attributed to a larger amount of oxygen vacancies and higher valence states of Co and Ni. We also performed a post-OER XAS characterization on BDC@CoNi-LDH to identify the origin of the high OER electrocatalytic activity (Figure 5.20).

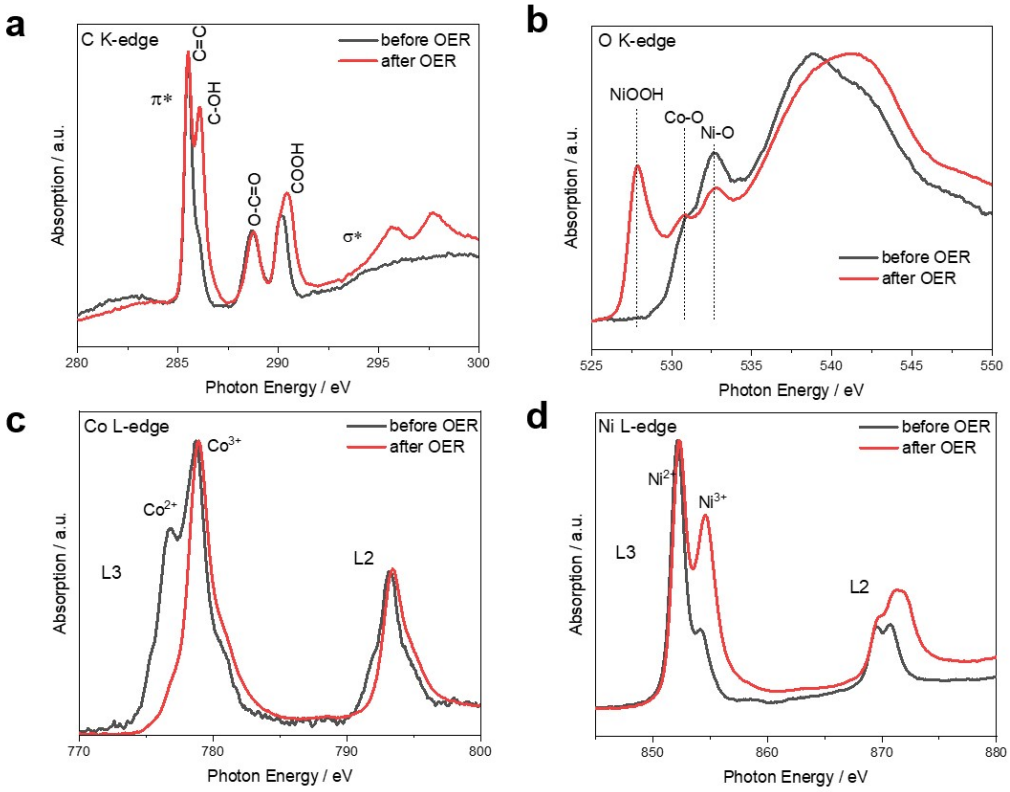


**Figure 5.20** Normalized XAS spectra of BDC@CoNi-LDH before and after OER process. (a) C K-edge, (b) O K-edge, (c) Co L-edge and (d) Ni L-edge. The post-OER samples are prepared by exposing the samples at 1.63 V for 15 min.

The O K-edge spectrum exhibits a newly emerged peak located at ~ 528 eV after OER, which can be attributed to NiOOH. The increase in hybridization between Ni 3d and O 2p states leads to the extraction of electrons from the oxygen in $NiO_6$ octahedra domains to the metal site ($Ni^{3+} - O^{2-} \rightarrow Ni^{(3-x)+} - O^{(2-x)-}$), in accordance with previous reports.[155,159] This phenomenon is also confirmed by the decreasing of Ni-O peak in the pre-peak region at 532.8 eV, suggestive of more oxygen vacancies formed onto Ni site,[160] which render a more efficient OER activity. In addition, after OER process, both Co and Ni ions are partially oxidized to a higher valence state of +3, which are known to be beneficial to OER.

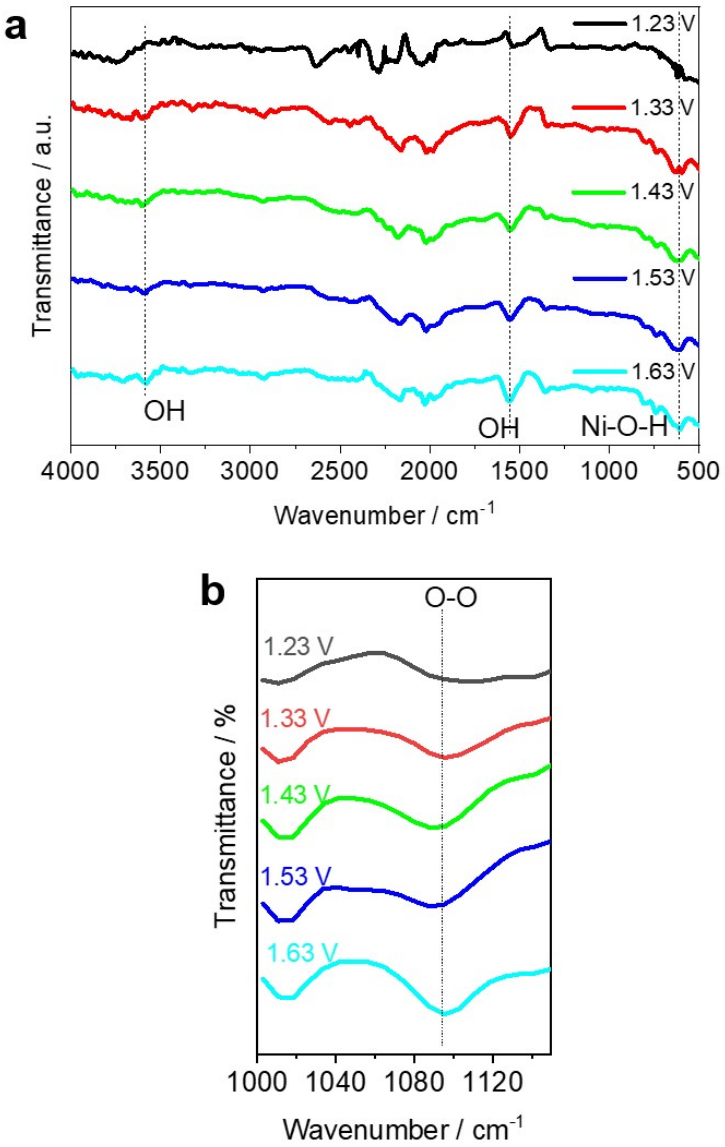


**Figure 5.21** Ex-situ ATR-FTIR spectra of BDC@CoNi-LDH under different potential (a) full wavenumber range from 500 to 4000 $cm^{-1}$, (b) O-O bond formation at 1090 $cm^{-1}$.

To further reveal the catalytically active sites of BDC@CoNi-LDH, the changes in local atomic environment and valence states are studied. BDC@CoNi-LDH is exposed under different potentials (1.23 V for OCP, 1.33 V, 1.43 V, 1.53 V and 1.63 V) for 15 min before an *ex-situ* characterization. Attenuated total reflection (ATR) FT-IR provides information of the functional groups near the surface, which allows its application to the

detection of surface alterations during OER process. The characteristic band at 3,590 and 1,560 $cm^{-1}$ (Figure 5.21a) correspond to the stretching and bending vibration of hydroxyl group on the surface.[161] The intensity of those two peaks is intensified as the overpotential increases, indicating the adsorption of $H_2O$ on the surface of the catalyst. The increased bending vibration of Ni-O-H (617 $cm^{-1}$) is ascribed to the formation of hydroxide species on the surface of $Ni(OH)_2$/NiOOH. Furthermore, the zoomed-in ATR-FTIR in Figure 5.21b shows the O-O bond (1,090 $cm^{-1}$) formation during OER process, which represents the establishment of oxygen bridge between multi-metal sites.[162] The multi-metal site mechanism could boost the kinetics of OER due to the direct O-O coupling and synergistic effect between metal atoms.[163]

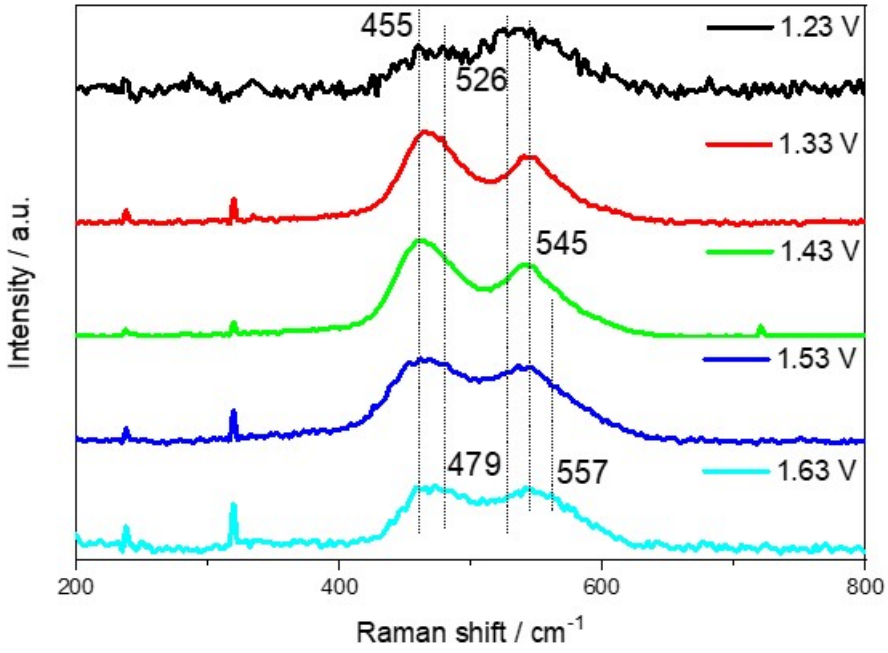


**Figure 5.22** Ex-situ Raman shift of BDC@CoNi-LDH under different potential.

The *ex-situ* Raman spectra are further obtained at different overpotentials and presented in Figure 5.22. At a potential of 1.43 V or less, there are only two distinct peaks at 455 and 526 $cm^{-1}$, which correspond to $Ni(OH)_2$. At a higher potential, however, signals from slightly higher Raman shift values (~ 479 and 557 $cm^{-1}$) start to emerge,

which are ascribed to the formation of γ-NiOOH.[164,165] The transformation of $Ni(OH)_2$ into γ-NiOOH, hence the effective oxidation of Ni (from $Ni^{2+}$ to $Ni^{3+}$) during OER process further demonstrates that the Ni cations effectively contributes to the enhanced performance toward OER.

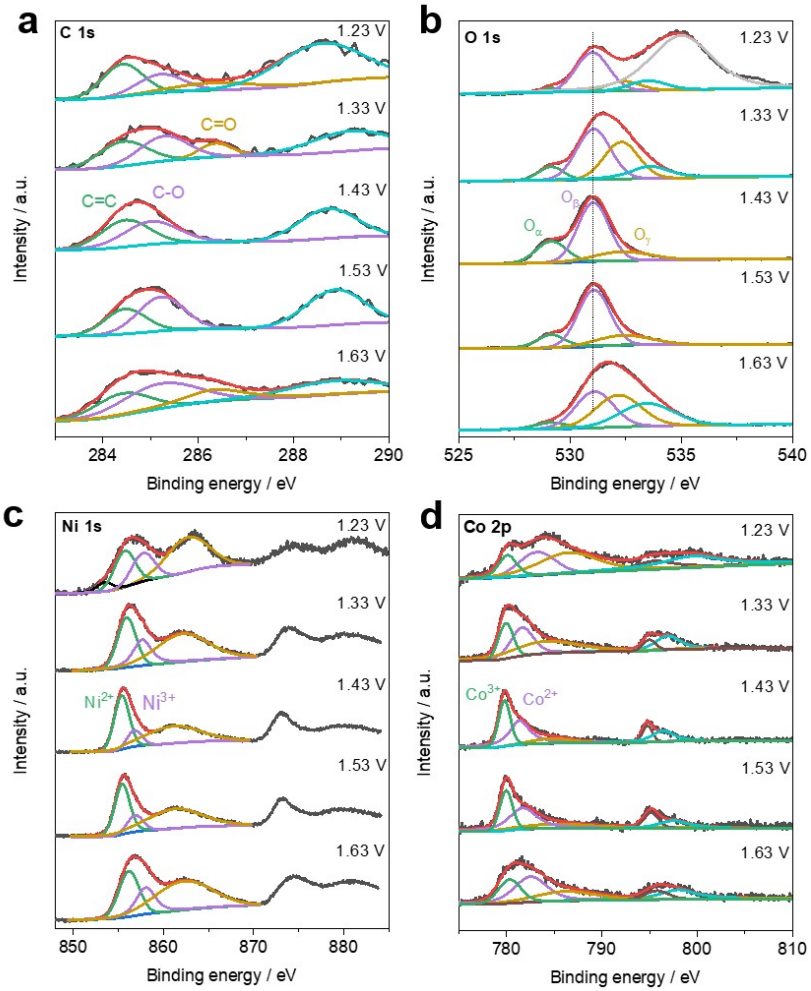


**Figure 5.23** *Ex-situ* XPS spectra of BDC@CoNi-LDH at different potentials. (a) C 1s, (b) O 1s, (c) Ni $2p_{3/2}$, (d) Co $2p_{3/2}$.

**Table 5.2** Relative contents of C species under different potential determined by C 1s XPS.

| Potential (V) | C-C (%) | C-O(%) | C=O(%) | O-C=O(%) |
|---|---|---|---|---|
| 1.23 | 21.5 | 14.0 | 9.7 | 54.8 |
| 1.33 | 26.5 | 26.9 | 9.9 | 36.6 |
| 1.43 | 29.6 | 30.7 | 0 | 39.6 |
| 1.53 | 22.1 | 33.9 | 0 | 44.0 |
| 1.63 | 23.7 | 35.6 | 14.4 | 26.4 |

**Table 5.3** Relative contents of O species under different potential determined by O 1s XPS.

| Potential (V) | M-O (%) | O vacancy(%) | OH(%) | O-C(%) | H2O(%) |
|---|---|---|---|---|---|
| 1.23 | 1.1 | 21.3 | 5.2 | 6.2 | 66.2 |
| 1.33 | 8.6 | 40.5 | 38.9 | 12.1 | 0 |
| 1.43 | 22.0 | 61.0 | 16.9 | 0 | 0 |
| 1.53 | 15.5 | 64.9 | 19.5 | 0 | 0 |
| 1.63 | 4.8 | 32.4 | 34.1 | 28.8 | 0 |

In addition, a series of *ex situ* XPS characterization of BDC@CoNi-LDH samples that underwent different potentials is performed to reveal the change in surface chemistry during OER process. **Figure 5.23a** and Table 5.2 show C 1s spectra under different potentials. The deconvoluted peak at 286.4 eV, which corresponds to C=O, disappeared at 1.43 and 1.53 V, indicating the breakage of the double-bond to form C-O-OH by attracting a hydroxyl group (Step 1 below) as shown in the following sequence of OER. The reoccurrence of C=O at 1.63 V suggests the desorption of $O_2$ (Step 5).

$$C = O \rightarrow C - O - OH \quad (1)$$

$$C - O - OH \rightarrow C - OO^* \quad (2)$$

$$C - OO^* \rightarrow C - V_O \quad (3)$$

$$C - V_O \rightarrow C - OH \quad (4)$$

$$C - OH \rightarrow C = O \quad (5)$$

These suggest that carbon sites in BDC also act as an active site for OER due to a high concentration of defects on their edge or surface, which is likely formed during urea-aided reconstruction of interlayers with LDH. The reconstructed lattice structures can effectively recreate the $\pi$ conjugation in carbon atoms and redistribution of electronic charges surrounding carbon atoms, resulting in an enhancement of electrocatalytic OER activity.[166] Moreover, the M-O (529.7 eV) and O vacancy (531.7 eV) increase from 1.23 to 1.43 V and decrease from 1.43 to 1.63 V simultaneously (Figure 5.23b), implying that the active metal center (Ni/Co) directly couples with *O intermediate and lattice oxygen to form $O_2$ molecular during OER process, in a good accordance with the lattice oxygen participation mechanism (LOM) as reported in the literature.[3,7,161,167] The relative $Ni^{3+}/Ni^{2+}$ ratio (Figure 5.23c; Table 5.4) decreases from 0.74 at OCP to 0.29 at 1.43 V and then increases to 0.69 at 1.63 V, while $Co^{3+}/Co^{2+}$ (Figure 5.23d; Table 5.5) exhibits the opposite trend, indicating that the formation of oxygen vacancies during OER occurs mostly on the Ni site. The binding energy of Co $2p_{3/2}$ and Ni $2p_{3/2}$ slightly shifted positively after OER, revealing a synergistic interplay between Co and Ni species, which

could not only yield stronger bonding to the intermediates, such as *OH, but also promote the deprotonation of adsorbates.

**Table 5.4** Relative contents of Ni species under different potential determined by Ni 2p XPS.

| Potential (V) | $Ni^{3+}/Ni^{2+}$ | $Ni^{2+}$(%) | $Ni^{3+}$(%) |
|---|---|---|---|
| 1.23 | 0.74 | 57.5 | 42.5 |
| 1.33 | 0.66 | 60.0 | 39.9 |
| 1.43 | 0.29 | 77.4 | 22.6 |
| 1.53 | 0.32 | 75.5 | 24.5 |
| 1.63 | 0.69 | 59.1 | 40.9 |

**Table 5.5** Relative contents of Co species under different potential determined by Co 2p XPS.

| Potential (V) | $Co^{3+}/Co^{2+}$ | $Co^{2+}$(%) | $Co^{3+}$(%) |
|---|---|---|---|
| 1.23 | 0.56 | 64.2 | 35.8 |
| 1.33 | 0.71 | 58.6 | 41.4 |
| 1.43 | 0.80 | 55.6 | 44.4 |
| 1.53 | 0.66 | 60.4 | 39.6 |
| 1.63 | 0.57 | 63.8 | 36.2 |

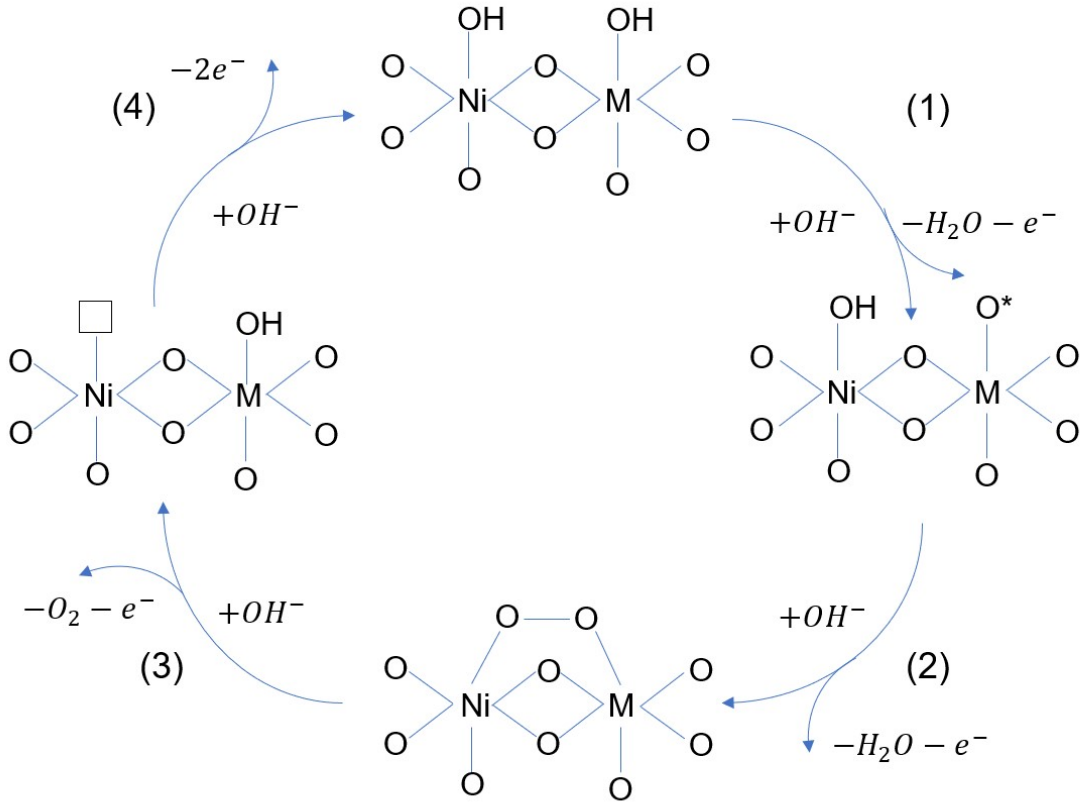


**Figure 5.24** Simplified OER dual-metal-site mechanism for BDC@CoNi-LDH structure.

Based on the discussions above, the mechanism of OER process in BDC@CoNi-LDH is proposed as follows. By incorporating an $OH^-$ group on the surface, M-OH is deprotonated to form M-O* (step 1 in **Figure 5.24**). Then, the intermediate Ni-O-O-M bridge is directly formed by incorporating another $OH^-$ group (step 2). With an additional $OH^-$ group, an $O_2$ desorbs from the surface bridge, leaving an oxygen vacancy bonded to Ni site while the other metal center is bonded to the incoming $OH^-$ (step 3). Then, a $OH^-$ group is adsorbed onto the vacant oxygen site bonded to Ni, forming Ni-OH (step 4). In this proposed mechanism, Ni facilitates the desorption of $O_2$, forming an oxygen vacancy in its adjacent O sites for a subsequent OH- adsorption, while Co serves as a strong Lewis acid to promote further oxidation of neighboring Ni.[168] On the other hand, carbon sites

away from metal centers also participate in OER as discussed above. First, $OH^-$ is adsorbed on a lattice defect and deprotonated to form O*. The *OOH intermediate is formed with the participation of $OH^-$, and the as-formed *OOH is deprotonated to form $O_2$. In comparison to the proposed OER process around metal centers (Figure 5.24), this process occurring on carbon defects is conjectured to be slower due to the additional step involving *OOH intermediate. Therefore, the multi-metal active site of layered LDHs together with carbon-based BDC defect rich structure could effectively enhance the performance of oxygen evolution reaction.

## 5.4 Conclusion

In summary, we successfully fabricated a core-shell structure comprised of CoNi-LDH nanosheets on the surface of CoNi-BDC tetragonal structure via a facile one step synthesis strategy. A unique 3D polyhedron microstructure with a coverage of numerous nanoplates is constructed by regulating the order of precursor introduction during synthesis process. The as-prepared BDC@CoNi-LDH catalyst demonstrates an excellent catalytic performance toward OER, with the overpotential of ~ 280 mV at 100 mA $cm^{-2}$ and Tafel slope of 105 mV $dec^{-1}$ in 1 M KOH. It also exhibits an excellent cyclic stability over 2,000 CV cycles. From a series of *ex situ* studies by Raman, ATR-FTIR, XPS, we further revealed the intrinsic active sites. The desorption of $O_2$ from Ni-O-O-M bridge bond is prompted on the multi-metal-site on the LDH surface while the Ni donates its active lattice oxygen. In addition, the superior high electrochemical surface area, high valence state of metal ions in $\gamma$-NiOOH/CoOOH, lattice edge sites of carbon, and the synergistic effect between neighboring metal atoms concertedly contributes to the enhanced performance. This work contributes to a general strategy for a rational design of multi-metallic hierarchical core-shell structures, and *quasi-operando* studies for revealing dynamic active sites during electrochemical process.

# CHAPTER 6. Atomically-dispersed Cerium/Titanum Oxide by ALD on Co-based LDH For Enhanced OER

## 6.1 Introduction

Recently, transition metal based layered double hydroxides (LDHs) based materials have attracted attention for the enhancement of OER performances due to their unique structural property, high specific capacitance, facile synthesis process and low cost. [117],[135] It can be represented by the general formula as $[M^{II}_{1-x} M^{III}_{x} (OH)_2]_{z+}(A^{n-})_{z/n}\cdot yH_2O$, where $M^{II}$ and $M^{III}$ are metallic divalent cations and metallic trivalent cations, and $A^{n-}$ represent for the interlayer anions, respectively. The highly flexible and tunable composition of $M^{II}$, $M^{III}$ and $A^{n-}$ in LDH structure provide large variety of possibilities for adjusting OER performance when applied as electrode materials.[119]

In this study, a simple and effective method for introducing a third metal - ceria was used to prepare high-performance Ni/Co-LDH based electrodes via hydrothermal approach followed by an ALD process, using Ni foam as the substrate to achieve the growth of Ni/Co nanostructures. A unique 3D nanoplates stand on nanowires was synthesized, achiving an uniform structure with high surface area and more active sites. The resultant Co/Ni@Ce and CoNi@Ti electrodes exhibits optimal activity and stability toward OER performance.

## 6.2 Results

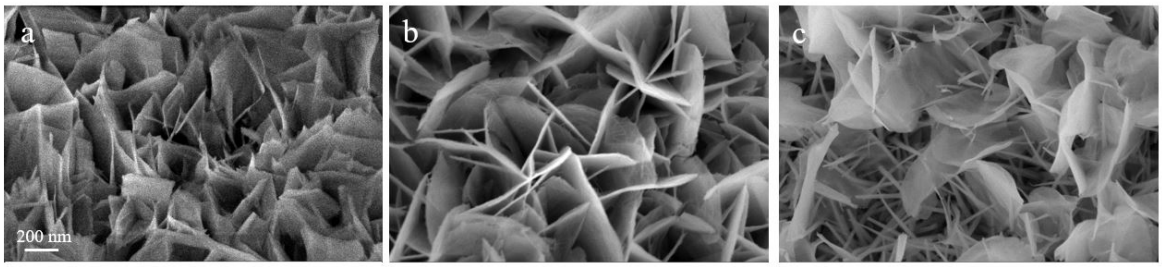

**Figure 6.1** SEM image of (a) CoNi-LDH, (b) CoNi-LDH@5Ti, (c) CoNi-LDH@5Ce and primary TEM image of CoNi-LDH@5Ce sample.

The hierarchical CoNi-LDH@X (X = Ce, Ti) nanoplate arrays are synthesized on the surface of a nickel foam substrate via simple hydrothermal procedure followed by the ALD process. A uniform coating of Ce/Ti oxide thin layer was achieved with appropriate cycles and temperature adjustment during ALD operation. The morphology of CoNi-LDH, CoNi-LDH@5Ce and CoNi-LDH@5Ti was studied by the scanning electronic microscope (SEM). As shown in Figure 6.1, all three sample displays the typical nanoplatelet arrays. Ultrathin and uniform CoNi-LDH platelets growing perpendicular to the surface of the substrate are observed, with 250–300 nm lateral length and ~10 nm thickness. In particular, the surface of the nanoplates turn to smooth after the thin layer coting of ceria and titanium oxide.

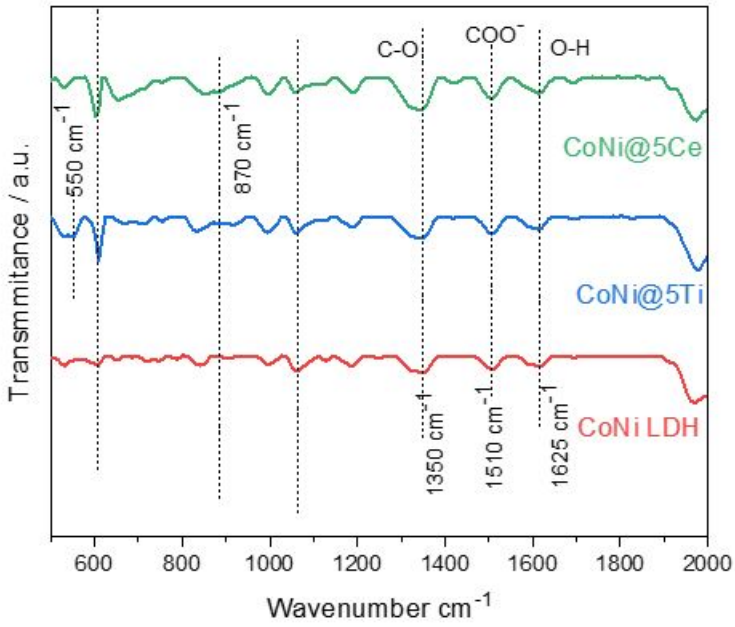


**Figure 6.2** FTIR spectra for the as-prepared samples.

Figure 6.2 shows the FTIR spectra of CoNi-LDH, CoNi@5Ce and CoNi@5Ti composite. The absorption peak at 1625 cm-1 corresponds to the typical O-H stretching vibration of the interlayer of basic LDH structures. Additionally, the peak at 1510 $cm^{-1}$ can be assigned to the vibratioin of $Co_3^{2-}$, which participated to form the nickel cobalt carbonate hydroxide hydrate with $Ni^{2+}$ and $Co^{2+}$ ions via coordinate bonds. The small peak at around 870 $cm^{-1}$ for CoNi@5Ce sample could be related with cerium-oxide stretching mode, confirms the existence of $CeO_2$. The newly emerged peak at 550 $cm^{-1}$ for sample CoNi@5Ti is attributed to the Ti stretching. Moreover, after incorporating with Ce and Ti, the peak at around 610 $cm^{-1}$ greatly intensified, suggesting the improved stretching vibration of metal oxide bond after ALD process. [135][134]

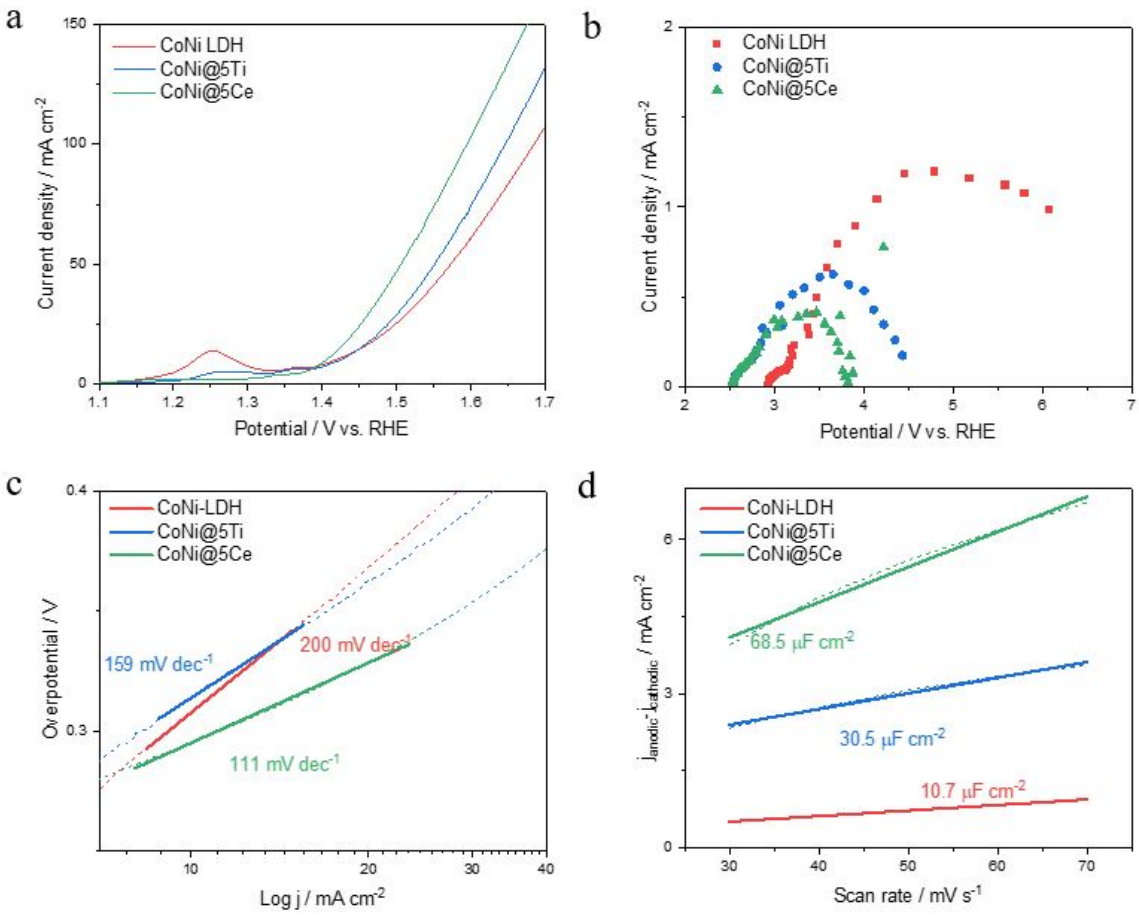


**Figure 6.3** Electrochemical measurement of CoNi-LDH, CoNi@5Ti and CoNi@5Ce. (a) LSV curves obtained in 1 M KOH for OER with the scan rate of 5 mV $s^{-1}$. (b) Nyquist plot from EIS obtained at 1.53 V versus RHE within the frequency range of 0.5 Hz – 1 MHz. (c) Tafel plot. (d) ECSA quantification of double layer capacitance based on the CVs.

The electrocatalytic activities of the as prepared catalyst toward OER were evaluated in alkaline solution (1 M KOH). Figure 6.3a plots the polarization curves of the LSV curve for three samples. For the linear sweep voltammetry (LSV) measurement, a low scan rate of 5 mV s-1 was chosen to eliminate the influence of the capacitive current. With the doping of Ti and Ce via ALD process, both sample shows improved OER performance compared with pure CoNi-LDH sample. To reach the current density of 50 mA $cm^{-1}$, the

overpotential of 343 mV is required for CoNi-LDH. In comparison, the overpotential of CoNi@5Ti and CoNi@5Ce yields overpotential of 320 mV and 270 mV, which is much lower than that of CoNi-LDH. EIS analysis is additionally performed to understand the reaction kinetics of OER. As illustrated in Figure 6.3b, ALD coated samples show decreased charge transfer resistance than that of CoNi-LDH, which indicates a more efficient charge transfer during OER process. Furthermore, both CoNi@5Ti and CoNi@5Ce shows lower ohmic resistance of 1.5 Ω, suggest a higher electronic conduction, which is also beneficial to the oxygen electrocatalysis performance. As shown in Figure 6.3c, the Tafel slope of CoNi@5Ce and CoNi@5Ti was 111 mV $dec^{-1}$ and 159 mV $dec^{-1}$, smaller than those of CoNi-LDH (200 mV $dec^{-1}$), in accordance with the LSV results. To reveal the intrinsic activity of the as-prepared catalysts, ECSAs were investigated with a cyclic voltammetry method. The scan rate dependency of cyclic voltammograms was measured between 1.10 and 1.20 V (vs RHE), and the full CV curves are shown in Figure 6.3d, from which $C_{dl}$ was calculated. The corresponding ECSA for CoNi-LDH, CoNi@5Ti and CoNi@5Ce was calculated to be 0.067 $cm^{-2}$, 0.191 $cm^{-2}$ and 0.428 $cm^{-2}$. The ECSA results further proves the CoNi@5Ce owns high active sites compared with CoNi-LDH.

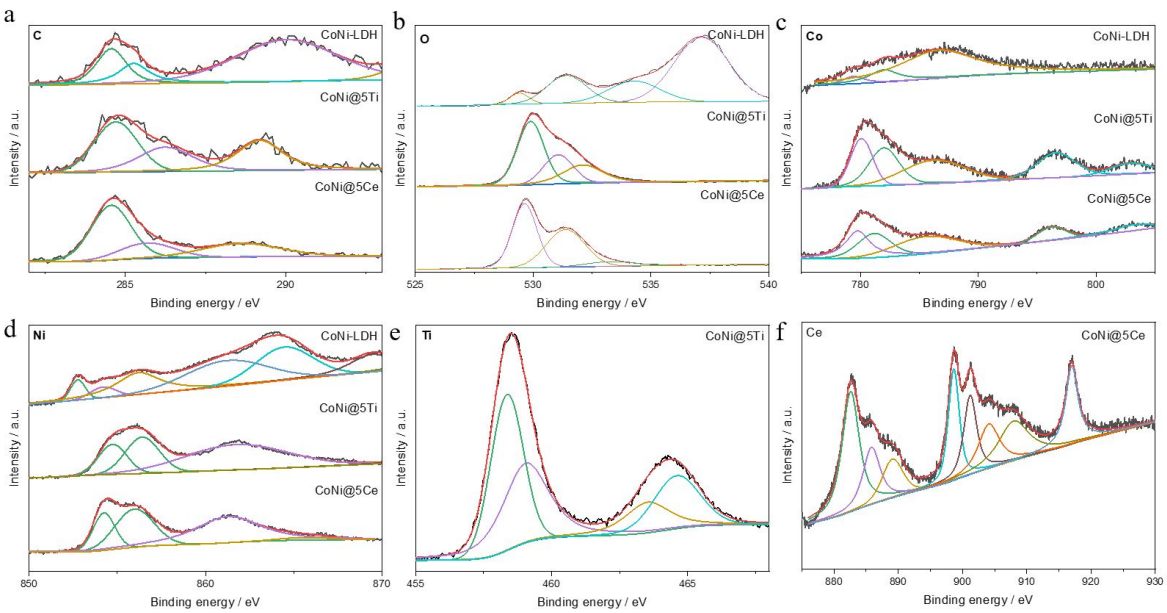


**Figure 6.4** XPS spectra of C, O, Ce, Ni, Ti and Ce element for Co/NC@X series.

XPS were performed to investigate the electronic structures of the samples. As shown in Figure 6.4 e and f, the titanium and cerium specific peaks suggests the successful doping of Ti and Ce atoms into the LDH structure. The C 1s peak (Figure 6.4a) can be deconvoluted into three peaks, corresponding to $sp^2$ C (284.7 eV), C-O/C-N (285.5 eV) and C=O/C=N (289.5 eV)[15], all inherit from the basic LDH structure. The O 1s spectrum shown in Figure 15b exhibits three peaks at 529.7, 531.8 and 533 eV for CoNi@5Ti and CoNi@5Ce samples, which corresponds to M-O, oxygen defect and hydroxyl species, respectively. In comparison with the CoNi-LDH sample, the peak at 537 and 535 eV greatly suppressed while M-O content greatly increased, indicates that the Ti and Ce species successfully bonding with the surface oxygen ligand during ALD reaction.

## 6.3 Conclusion

In summary, I demonstrated CoNi-LDH@X (X = Ce, Ti) as an efficient electrocatalytic OER catalyst. Particularly, the CoNi-LDH@5Ce sample exhibits excellent OER performance with a much lower overpotential of 270 mV to reach the current density of 50 mA $cm^{-2}$ than the others. The enhanced performance could be attributed to the synergic effect between the doping element (Ce, Ti) and base transitional metal (Co, Ni). Furthermore, the metal oxide, especially cobalt oxide species generated on the surface during ALD process would also contribute to the acceleration of O-O bond formation rates during OER process.

# REFERENCES


[1] J. Wu, Y. Huang, W. Ye, Y. Li, *Adv. Sci.* **2017**, *4*, DOI 10.1002/advs.201700194.

[2] M. Ding, R. W. Flaig, H. L. Jiang, O. M. Yaghi, *Chem. Soc. Rev.* **2019**, *48*, 2783–2828.

[3] Y.-C. Zhang, C. Han, J. Gao, L. Pan, J. Wu, X.-D. Zhu, J.-J. Zou, *ACS Catal.* **2021**, *11*, 12485–12509.

[4] Y. Li, Q. Li, H. Wang, L. Zhang, D. P. Wilkinson, J. Zhang, *Electrochem. Energy Rev.* **2019**, *2*, 518–538.

[5] T. Ghosh, A. Mohammad, S. M. Mobin, *ACS Sustain. Chem. Eng.* **2019**, *7*, 13746–13763.

[6] Z. Song, N. Cheng, A. Lushington, X. Sun, *Catalysts* **2016**, *6*, 116.

[7] Z. F. Huang, J. Song, S. Dou, X. Li, J. Wang, X. Wang, *Matter* **2019**, *1*, 1494–1518.

[8] M. Liu, L. Wang, K. Zhao, S. Shi, Q. Shao, L. Zhang, X. Sun, Y. Zhao, J. Zhang, *Energy Environ. Sci.* **2019**, *12*, 2890–2923.

[9] W. Zhang, W. Lai, R. Cao, *Chem. Rev.* **2017**, *117*, 3717–3797.

[10] J. Song, C. Wei, Z. F. Huang, C. Liu, L. Zeng, X. Wang, Z. J. Xu, *Chem. Soc. Rev.* **2020**, *49*, 2196–2214.

[11] Z.-F. Huang, J. Wang, Y. Peng, C.-Y. Jung, A. Fisher, X. Wang, *Adv. Energy Mater.* **2017**, *7*, 1700544.

[12] R. Borup, J. Meyers, B. Pivovar, Y. S. Kim, R. Mukundan, N. Garland, D. Myers, M. Wilson, F. Garzon, D. Wood, P. Zelenay, K. More, K. Stroh, T. Zawodzinski, J. Boncella, J. E. Mcgrath, M. Inaba, K. Miyatake, M. Hori, K. Ota, Z. Ogumi, S. Miyata, A. Nishikata, Z. Siroma, Y. Uchimoto, K. Yasuda, K.-I. Kimijima, N. Iwashita, **2007**, DOI 10.1021/cr050182l.

[13] Q. Wang, D. Astruc, *Chem. Rev.* **2020**, *120*, 1438–1511.

[14] Y. Wang, L. Tao, Z. Xiao, R. Chen, Z. Jiang, S. Wang, *Adv. Funct. Mater.* **2018**, *28*, 1705356.

[15] M. Zhang, Q. Dai, H. Zheng, M. Chen, L. Dai, *Adv. Mater.* **2018**, *30*, DOI 10.1002/adma.201705431.

[16] A. Bavykina, N. Kolobov, I. S. Khan, J. A. Bau, A. Ramirez, J. Gascon, *Chem. Rev.* **2020**, *120*, 8468–8535.

[17] W. Xia, A. Mahmood, R. Zou, Q. Xu, *Energy Environ. Sci.* **2015**, *8*, 1837–1866.

[18] L. Li, J. He, Y. Wang, X. Lv, X. Gu, P. Dai, D. Liu, X. Zhao, *J. Mater. Chem. A* **2019**, *7*, 1964–1988.

[19] M. Andersen, S. V Levchenko, M. Scheffler, K. Reuter, *Beyond Scaling Relations for the Description of Catalytic Materials*, **n.d.**

[20] J. Stacy, Y. N. Regmi, B. Leonard, M. Fan, *Renew. Sustain. Energy Rev.* **2017**, *69*, 401–414.

[21] Y. Li, Q. Sun, *Adv. Energy Mater.* **2016**, *6*, DOI 10.1002/aenm.201600463.

[22] B. Y. Xia, Y. Yan, N. Li, H. Bin Wu, X. W. Lou, X. Wang, *Nat. Energy* **2016**, *1*, 15006.

[23] Y. Hou, Z. Wen, S. Cui, S. Ci, S. Mao, J. Chen, *Adv. Funct. Mater.* **2015**, *25*, 872–882.

[24] T. Zhou, W. Xu, N. Zhang, Z. Du, C. Zhong, W. Yan, H. Ju, W. Chu, H. Jiang, C. Wu, Y. Xie, *Adv. Mater.* **2019**, *31*, 1807468.

[25] K. B. Ibrahim, M. Tsai, S. A. Chala, M. K. Berihun, A. W. Kahsay, T. A. Berhe, W. Su, B. Hwang, *J. Chinese Chem. Soc.* **2019**, *66*, 829–865.

[26] S. Dou, X. Li, L. Tao, J. Huo, S. Wang, *Chem. Commun.* **2016**, *52*, 9727–9730.

[27] I. S. Amiinu, X. Liu, Z. Pu, W. Li, Q. Li, J. Zhang, H. Tang, H. Zhang, S. Mu, *Adv. Funct. Mater.* **2018**, *28*, 1704638.

[28] Y. Liu, T. G. Kelly, J. G. Chen, W. E. Mustain, *ACS Catal.* **2013**, *3*, 1184–1194.

[29] L. Shang, H. Yu, X. Huang, T. Bian, R. Shi, Y. Zhao, G. I. N. Waterhouse, L.-Z. Wu, C.-H. Tung, T. Zhang, L. Shang, H. Yu, X. Huang, T. Bian, Y. F. Zhao, L.-Z. Wu, C.-H. Tung, T. Zhang, M. R. Shi, G. I. N. Waterhouse, *Adv. Mater.* **2016**, *28*, 1668–1674.

[30] X. Tian, J. Luo, H. Nan, H. Zou, R. Chen, T. Shu, X. Li, Y. Li, H. Song, S. Liao, R. R. Adzic, *J. Am. Chem. Soc.* **2016**, *138*, 1575–1583.

[31] X. Li, Q. Jiang, S. Dou, L. Deng, J. Huo, S. Wang, *J. Mater. Chem. A* **2016**, *4*, 15836–15840.

[32] Y.-Z. Chen, R. Zhang, L. Jiao, H.-L. Jiang, *Coord. Chem. Rev.* **2018**, *362*, 1–23.

[33] G. Zhong, D. Liu, J. Zhang, *J. Mater. Chem. A* **2018**, *6*, 1887–1899.

[34] Y.-X. Zhou, Y.-Z. Chen, L. Cao, J. Lu, H.-L. Jiang, *Chem. Commun.* **2015**, *51*, 8292–8295.

[35] Y.-N. Hou, Z. Zhao, Z. Yu, Y. Tang, X. Wang, J. Qiu, *Chem. Commun.* **2017**, *53*, 7840–7843.

[36] S. Sun, G. Zhang, N. Gauquelin, N. Chen, J. Zhou, S. Yang, W. Chen, X. Meng, D. Geng, M. N. Banis, R. Li, S. Ye, S. Knights, G. A. Botton, T.-K. Sham, X. Sun, **n.d.**, DOI 10.1038/srep01775.

[37] B. J. O'Neill, D. H. K. Jackson, J. Lee, C. Canlas, P. C. Stair, C. L. Marshall, J. W. Elam, T. F. Kuech, J. A. Dumesic, G. W. Huber, *ACS Catal.* **2015**, *5*, 1804–1825.

[38] J. A. Singh, N. Yang, S. F. Bent, *Annu. Rev. Chem. Biomol. Eng.* **2017**, *8*, 41–62.

[39] W. Li, S. Chen, M. Zhong, C. Wang, X. Lu, *Chem. Eng. J.* **2021**, *415*, 128879.

[40] C. Jing, B. Dong, Y. Zhang, *ENERGY Environ. Mater.* **2020**, *3*, 346–379.

[41] K. Zhu, J. Chen, W. Wang, J. Liao, J. Dong, M. O. L. Chee, N. Wang, P. Dong, P. M. Ajayan, S. Gao, J. Shen, M. Ye, *Adv. Funct. Mater.* **2020**, 2003556.

[42] X. Lu, H. Xue, H. Gong, M. Bai, D. Tang, R. Ma, T. Sasaki, *Nano-Micro Lett.* **2020**, *12*, 1–32.

[43] A. V. Rane, K. Kanny, V. K. Abitha, S. Thomas, *Synth. Inorg. Nanomater.* **2018**, 121–139.

[44] R. W. Johnson, A. Hultqvist, S. F. Bent, *Mater. Today* **2014**, *17*, 236–246.

[45] X. Wang, H. Zhang, H. Lin, S. Gupta, C. Wang, Z. Tao, H. Fu, T. Wang, J. Zheng, G. Wu, X. Li, **2016**, DOI 10.1016/j.nanoen.2016.04.042.

[46] Y.-L. Zhang, K. Goh, L. Zhao, X.-L. Sui, X.-F. Gong, J.-J. Cai, Q.-Y. Zhou, H.-D. Zhang, L. Li, F.-R. Kong, D.-M. Gu, Z.-B. Wang, *Nanoscale* **2020**, *12*, 21534–21559.

[47] J. Zhao, J.-J. Zhang, Z.-Y. Li, X.-H. Bu, *SMALL* **n.d.**, DOI 10.1002/smll.202003916.

[48] J. Zhang, Z. Zhao, Z. Xia, L. Dai, *Nat. Nanotechnol.* **2015**, *10*, 444–452.

[49] K. Zeng, X. Zheng, C. Li, J. Yan, J.-H. Tian, C. Jin, P. Strasser, R. Yang, *Adv.*

*Funct. Mater.* **2020**, *30*, 2000503.

[50] H. Osgood, S. V. Devaguptapu, H. Xu, J. Cho, G. Wu, *Nano Today* **2016**, *11*, 601–625.

[51] M. Chen, L. Wang, H. Yang, S. Zhao, H. Xu, G. Wu, *J. Power Sources* **2018**, *375*, 277–290.

[52] D. Wang, X. Pan, P. Yang, R. Li, H. Xu, Y. Li, F. Meng, J. Zhang, M. An, *ChemSusChem* **2020**, cssc.202002137.

[53] I. K. Sideri, N. Tagmatarchis, *Chem. – A Eur. J.* **2020**, *26*, 15397–15415.

[54] Y. Wang, J. Li, Z. Wei, *J. Mater. Chem. A* **2018**, *6*, 8194–8209.

[55] Z. Liu, H. Cheng, N. Li, T. Y. Ma, Y. Su, *Adv. Mater.* **2016**, *28*, 3777–3784.

[56] D. Ding, K. Shen, X. Chen, H. Chen, J. Chen, T. Fan, R. Wu, Y. Li, *ACS Catal.* **2018**, *8*, 7879–7888.

[57] P. Liu, Y. Hu, X. Liu, T. Wang, P. Xi, S. Xi, D. Gao, J. Wang, *J. Mater. Chem. A* **2019**, *7*, 12851–12858.

[58] H. Cheng, M.-L. Li, C.-Y. Su, N. Li, Z.-Q. Liu, *Adv. Funct. Mater.* **2017**, *27*, 1701833.

[59] M. Kuang, Q. Wang, P. Han, G. Zheng, *Adv. Energy Mater.* **2017**, *7*, 1700193.

[60] H. Sun, C. Tian, G. Fan, J. Qi, Z. Liu, Z. Yan, F. Cheng, J. Chen, C. Li, M. Du, *Adv. Funct. Mater.* **2020**, 1910596.

[61] N. Qiu, J. Zhang, Z. Wu, *Phys. Chem. Chem. Phys.* **2014**, *16*, 22659–22664.

[62] H. Xu, Z.-X. Shi, Y.-X. Tong, G.-R. Li, *Adv. Mater.* **2018**, *30*, 1705442.

[63] Y. Yang, Y. Wang, Y. Xiong, X. Huang, L. Shen, R. Huang, H. Wang, J. P. Pastore, S.-H. H. Yu, L. Xiao, J. D. Brock, L. Zhuang, H. D. Abruña, *J. Am. Chem. Soc.* **2019**, *141*, 1463–1466.

[64] W. Niu, J. Shi, L. Ju, Z. Li, N. Orlovskaya, Y. Liu, Y. Yang, *ACS Catal.* **2018**, *8*, 12030–12040.

[65] H. Li, H.-S. Kang, S. Grewal, A. J. Nelson, S. A. Song, M. H. Lee, *J. Mater. Chem. A* **2020**, *8*, 15927–15935.

[66] J. I. Langford, A. J. C. Wilson, *Seherrer after Sixty Years: A Survey and Some New Results in the Determination of Crystallite Size*, **1978**.

[67] K. I. Maslakov, Y. A. Teterin, A. J. Popel, A. Y. Teterin, K. E. Ivanov, S. N. Kalmykov, V. G. Petrov, P. K. Petrov, I. Farnan, *Appl. Surf. Sci.* **2018**, *448*, 154–162.

[68] U. A. Paulus, T. J. Schmidt, H. A. Gasteiger, R. J. Behm, *Oxygen Reduction on a High-Surface Area Pt/Vulcan Carbon Catalyst: A Thin-Film Rotating Ring-Disk Electrode Study*, **2001**.

[69] A. Zanon, S. Chaemchuen, B. Mousavi, F. Verpoort, *J. CO2 Util.* **2017**, *20*, 282–291.

[70] Z.-X. Low, J. Yao, Q. Liu, M. He, Z. Wang, A. K. Suresh, J. Bellare, H. Wang, *Cryst. Growth Des.* **2014**, *14*, 6589–6598.

[71] A. Khan, M. Ali, A. Ilyas, P. Naik, I. F. J. Vankelecom, M. A. Gilani, M. R. Bilad, Z. Sajjad, A. L. Khan, *Sep. Purif. Technol.* **2018**, *206*, 50–58.

[72] S. Yari, S. Abbasizadeh, S. E. Mousavi, M. S. Moghaddam, A. Z. Moghaddam, *Process Saf. Environ. Prot.* **2015**, *94*, 159–171.

[73] M. Farokhi, A. Parvareh, M. K. Moraveji, *Environ. Sci. Pollut. Res.* **2018**, *25*, 27059–27073.

[74] M. Z. Majid Farahmandjou, *J. Ultrafine Grained Nanostructured Mater.* **2015**, *48*, 5–10.

[75] S. Xu, C. Lv, T. He, Z. Huang, C. Zhang, *J. Mater. Chem. A* **2019**, *7*, 7526–7532.

[76] Chuqian Meng, Yang Cao, Yonglan Luo, Fang Zhang, Qingquan Kong, A. Ali Alshehri, K. Ahmed Alzahrani, Tingshuai Li, Qian Liu, Xuping Sun, *Inorg. Chem. Front.* **2021**, *8*, 3007–3011.

[77] W. Xu, F. Lyu, Y. Bai, A. Gao, J. Feng, Z. Cai, Y. Yin, *Nano Energy* **2018**, DOI 10.1016/j.nanoen.2017.11.022.

[78] A. Sivanantham, P. Ganesan, S. Shanmugam, *Appl. Catal. B Environ.* **2018**, *237*, 1148–1159.

[79] D. Wu, Y. Wei, X. Ren, X. Ji, Y. Liu, X. Guo, Z. Liu, A. M. Asiri, Q. Wei, X. Sun, *Adv. Mater.* **2018**, *30*, 1705366.

[80] C. Ye, L. Zhang, L. Yue, B. Deng, Y. Cao, Q. Liu, Y. Luo, S. Lu, B. Zheng, X. Sun, *Inorg. Chem. Front.* **2021**, *8*, 3162–3166.

[81] L. Xu, Q. Jiang, Z. Xiao, X. Li, J. Huo, S. Wang, L. Dai, *Angew. Chemie* **2016**, *128*, 5363–5367.

[82] Y. Yu, X. Wang, W. Gao, P. Li, W. Yan, S. Wu, Q. Cui, W. Song, K. Ding, *J. Mater. Chem. A* **2017**, *5*, 6656–6663.

[83] Y. Li, W. Zhou, H. Wang, L. Xie, Y. Liang, F. Wei, J. C. Idrobo, S. J. Pennycook, H. Dai, *Nat. Nanotechnol.* **2012**, *7*, 394–400.

[84] D. Guo, R. Shibuya, C. Akiba, S. Saji, T. Kondo, J. Nakamura, *Science (80-. ).* **2016**, *351*, 361–365.

[85] D. Yu, K. Goh, H. Wang, L. Wei, W. Jiang, Q. Zhang, L. Dai, Y. Chen, *Nat. Nanotechnol.* **2014**, *9*, 555–562.

[86] X.-R. Wang, J.-Y. Liu, Z.-W. Liu, W.-C. Wang, J. Luo, X.-P. Han, X.-W. Du, S.-Z. Qiao, J. Yang, *Adv. Mater.* **2018**, *30*, 1800005.

[87] B. Seo, Y. J. Sa, J. Woo, K. Kwon, J. Park, T. J. Shin, H. Y. Jeong, S. H. Joo, *ACS Catal.* **2016**, *6*, 4347–4355.

[88] K. Liu, X. Huang, H. Wang, F. Li, Y. Tang, J. Li, M. Shao, *ACS Appl. Mater. Interfaces* **2016**, *8*, 34422–34430.

[89] J. Liu, H. Bao, B. Zhang, Q. Hua, M. Shang, J. Wang, L. Jiang, *ACS Appl. Mater. Interfaces* **2019**, *11*, 12525–12534.

[90] J. Yang, H. Liu, W. N. Martens, R. L. Frost, *J. Phys. Chem. C* **2010**, *114*, 111–119.

[91] Y. Liang, H. Wang, P. Diao, W. Chang, G. Hong, Y. Li, M. Gong, L. Xie, J. Zhou, J. Wang, T. Z. Regier, F. Wei, H. Dai, *J. Am. Chem. Soc.* **2012**, *134*, 15849–15857.

[92] D. Jain, Q. Zhang, J. Hightower, V. Gustin, A. Asthagiri, U. S. Ozkan, *ChemCatChem* **2019**, *11*, 5945–5950.

[93] X. Chen, B. Liu, C. Zhong, Z. Liu, J. Liu, L. Ma, Y. Deng, X. Han, T. Wu, W. Hu, J. Lu, *Adv. Energy Mater.* **2017**, *7*, 1700779.

[94] Z. Xiao, Y.-C. Huang, C.-L. Dong, C. Xie, Z. Liu, S. Du, W. Chen, D. Yan, L. Tao, Z. Shu, G. Zhang, H. Duan, Y. Wang, Y. Zou, R. Chen, S. Wang, *J. Am. Chem. Soc.* **2020**, *142*, 12087–12095.

[95] J.-H. Kim, K. Shin, K. Kawashima, D. H. Youn, J. Lin, T. E. Hong, Y. Liu, B. R.

Wygant, J. Wang, G. Henkelman, C. B. Mullins, *ACS Catal.* **2018**, *8*, 4257–4265.

[96] L. Li, H. Yang, J. Miao, L. Zhang, H. Y. Wang, Z. Zeng, W. Huang, X. Dong, B. Liu, *ACS Energy Lett.* **2017**, *2*, 294–300.

[97] F. Yang, J. Graciani, J. Evans, P. Liu, J. Hrbek, J. F. Sanz, J. A. Rodriguez, *J. Am. Chem. Soc.* **2011**, *133*, 3444–3451.

[98] X. Li, Y. Fang, X. Lin, M. Tian, X. An, Y. Fu, R. Li, J. Jin, J. Ma, *J. Mater. Chem. A* **2015**, *3*, 17392–17402.

[99] M. Khalid, A. M. B. Honorato, H. Varela, L. Dai, *Nano Energy* **2018**, *45*, 127–135.

[100] Z. Wang, W. Xu, X. Chen, Y. Peng, Y. Song, C. Lv, H. Liu, J. Sun, D. Yuan, X. Li, X. Guo, D. Yang, L. Zhang, *Adv. Funct. Mater.* **2019**, *29*, 1902875.

[101] S. Feng, C. Liu, Z. Chai, Q. Li, D. Xu, *Nano Res.* **2018**, *11*, 1482–1489.

[102] Y. Li, Q. Liu, S. Zhang, G. Li, *ChemCatChem* **2019**, *11*, 861–867.

[103] H.-C. Li, Y.-J. Zhang, X. Hu, W.-J. Liu, J.-J. Chen, H.-Q. Yu, *Adv. Energy Mater.* **2018**, *8*, 1702734.

[104] L. He, J. Liu, B. Hu, Y. Liu, B. Cui, D. Peng, Z. Zhang, S. Wu, B. Liu, *J. Power Sources* **2019**, *414*, 333–344.

[105] C. Li, M. Wu, R. Liu, *Appl. Catal. B Environ.* **2019**, *244*, 150–158.

[106] L. Zhu, D. Zheng, Z. Wang, X. Zheng, P. Fang, J. Zhu, M. Yu, Y. Tong, X. Lu, *Adv. Mater.* **2018**, *30*, 1805268.

[107] J. H. Kim, K. Shin, K. Kawashima, D. H. Youn, J. Lin, T. E. Hong, Y. Liu, B. R. Wygant, J. Wang, G. Henkelman, C. B. Mullins, *ACS Catal.* **2018**, *8*, 4257–4265.

[108] S. Y. Tee, K. Y. Win, W. S. Teo, L.-D. Koh, S. Liu, C. P. Teng, M.-Y. Han, *Adv. Sci.* **2017**, *4*, 1600337.

[109] J. G. Li, H. Sun, L. Lv, Z. Li, X. Ao, C. Xu, Y. Li, C. Wang, *ACS Appl. Mater. Interfaces* **2019**, *11*, 8106–8114.

[110] L. Yu, H. Zhou, J. Sun, F. Qin, F. Yu, J. Bao, Y. Yu, S. Chen, Z. Ren, *Energy Environ. Sci.* **2017**, *10*, 1820–1827.

[111] Y. Wang, C. Xie, Z. Zhang, D. Liu, R. Chen, S. Wang, *Adv. Funct. Mater.* **2018**, *28*, 1703363.

[112] Z. Liu, A. M. Andrade, S. Grewal, A. J. Nelson, K. Thongrivong, H.-S. Kang, H. Li, Z. Nasef, G. Diaz, M. H. Lee, *Int. J. Hydrogen Energy* **2021**, *46*, 38258–38269.

[113] R. Frydendal, E. A. Paoli, B. P. Knudsen, B. Wickman, P. Malacrida, I. E. L. Stephens, I. Chorkendorff, *ChemElectroChem* **2014**, *1*, 2075–2081.

[114] Y. Lee, J. Suntivich, K. J. May, E. E. Perry, Y. Shao-Horn, *J. Phys. Chem. Lett.* **2012**, *3*, 399–404.

[115] T. Reier, M. Oezaslan, P. Strasser, *ACS Catal.* **2012**, *2*, 1765–1772.

[116] M. Gao, W. Sheng, Z. Zhuang, Q. Fang, S. Gu, J. Jiang, Y. Yan, *J. Am. Chem. Soc.* **2014**, *136*, 7077–7084.

[117] Z. Jiang, Z. Li, Z. Qin, H. Sun, X. Jiao, D. Chen, **n.d.**, DOI 10.1039/c3nr03829g.

[118] L. Huang, G. Gao, H. Zhang, J. Chen, Y. Fang, S. Dong, *Nano Energy* **2020**, *68*, 104296.

[119] L. Lv, Z. Yang, K. Chen, C. Wang, Y. Xiong, *Adv. Energy Mater.* **2019**, *9*, 1803358.

[120] D. S. Hall, D. J. Lockwood, C. Bock, B. R. MacDougall, *Proc. R. Soc. A Math. Phys. Eng. Sci.* **2015**, *471*, DOI 10.1098/RSPA.2014.0792.

[121] J. Huo, Y. Wang, L. Yan, Y. Xue, S. Li, M. Hu, Y. Jiang, Q.-G. Zhai, *Nanoscale* **2020**, *12*, 14514–14523.

[122] H. S. Jadhav, A. Roy, B. Z. Desalegan, J. G. Seo, *Sustain. Energy Fuels* **2019**, *4*, 312–323.

[123] L. Ni, J. Zhou, N. Chen, X. Li, S. Xu, L. Zhang, C. Lu, J. Chen, L. Xu, W. Hou, *Int. J. Hydrogen Energy* **2020**, *45*, 22788–22796.

[124] Y. Luo, Y. Wu, D. Wu, C. Huang, D. Xiao, H. Chen, S. Zheng, P. K. Chu, *ACS Appl. Mater. Interfaces* **2020**, *12*, 42850–42858.

[125] B. Huang, Y. Tang, C.-H. Yan, M. Sun, H. Xu, F. Chang, X.-X. Wu, *Energy Environ. Sci.* **2020**, DOI 10.1039/D0EE02113J.

[126] H. Zhang, L. Zhang, J. Deng, Y. Han, X. Li, *J. Mater. Sci.* **2018**, *53*, 8474–8482.

[127] L. Lv, Z. Yang, K. Chen, C. Wang, Y. Xiong, *Adv. Energy Mater.* **2019**, *9*, 1803358.

[128] N. Liu, J. Lin, J. Wu, M. Huang, L. Fan, Z. Song, C. Geng, T. Zhu, W. Pan,

*Electrochim. Acta* **2020**, *336*, 135550.

[129] A. Pimsawat, A. Tangtrakarn, N. Pimsawat, S. Daengsakul, *Sci. Reports 2019 91* **2019**, *9*, 1–11.

[130] C. Xing, F. Musharavati, H. Li, E. Zalezhad, O. K. S. Hui, S. Bae, B.-Y. Cho, *RSC Adv.* **2017**, *7*, 38945–38950.

[131] Y. Zhao, G. Gu, S. You, R. Ji, H. Suo, C. Zhao, F. Liu, *RSC Adv.* **2015**, *5*, 53665–53670.

[132] Y. Wang, M. Qiao, Y. Li, S. Wang, Y. Wang, S. Wang, M. Qiao, Y. Li, *Small* **2018**, *14*, 1800136.

[133] C. A. Téllez S., E. Hollauer, M. A. Mondragon, V. M. Castaño, *Spectrochim. Acta Part A Mol. Biomol. Spectrosc.* **2001**, *57*, 993–1007.

[134] M. Dinari, H. Allami, M. M. Momeni, *J. Electroanal. Chem.* **2020**, *877*, 114643.

[135] T. M. Masikhwa, M. J. Madito, D. Y. Momodu, J. K. Dangbegnon, O. Guellati, A. Harat, M. Guerioune, F. Barzegar, N. Manyala, **n.d.**, DOI 10.1039/c6ra07419g.

[136] P. E. Lokhande, U. S. Chavan, *Mater. Sci. Energy Technol.* **2019**, *2*, 52–56.

[137] C. W. Tang, C. Bin Wang, S. H. Chien, *Thermochim. Acta* **2008**, *473*, 68–73.

[138] Z. Ni, Y. Wang, T. Yu, Z. Shen, *Nano Res.* **2008**, *1*, 273–291.

[139] X. Meng, M. Feng, H. Zhang, Z. Ma, C. Zhang, *J. Alloys Compd.* **2017**, *695*, 3522–3529.

[140] J. H. Zhong, A. L. Wang, G. R. Li, J. W. Wang, Y. N. Ou, Y. X. Tong, *J. Mater. Chem.* **2012**, *22*, 5656–5665.

[141] B. Wang, J. Jin, B. Ding, X. Han, A. Han, J. Liu, *Front. Mater.* **2020**, *7*, 37.

[142] Z. Gao, J. Liu, X. Chen, X. Zheng, J. Mao, H. Liu, T. Ma, L. Li, W. Wang, X. Du, *Adv. Mater.* **2019**, *31*, 1804769.

[143] M. Arif, G. Yasin, M. Shakeel, M. A. Mushtaq, W. Ye, X. Fang, S. Ji, D. Yan, *Mater. Chem. Front.* **2019**, *3*, 520–531.

[144] A. Macedo Andrade, Z. Liu, S. Grewal, A. J. Nelson, Z. Nasef, G. Diaz, M. H. Lee, *Dalt. Trans.* **2021**, *50*, 5473–5482.

[145] S. Pacley, W. Mitchell, P. T. Murray, D. Anderson, H. E. Smith, E. Beck-Millerton, A. A. Voevodin, *Carbon Nanotub. Graphene, Assoc. Devices V* **2012**,

*8462*, 846205.

[146] A. Furlan, J. Lu, L. Hultman, U. Jansson, M. Magnuson, *J. Phys. Condens. Matter* **2014**, *26*, 415501.

[147] Z. Liu, A. M. Andrade, S. Grewal, A. J. Nelson, K. Thongrivong, H. Sen Kang, H. Li, Z. Nasef, G. Diaz, M. H. Lee, *Int. J. Hydrogen Energy* **2021**, *46*, 38258–38269.

[148] H. Y. Wang, Y. Y. Hsu, R. Chen, T. S. Chan, H. M. Chen, B. Liu, *Adv. Energy Mater.* **2015**, *5*, 1500091.

[149] F.-L. Li, P. Wang, X. Huang, D. James Young, H.-F. Wang, P. Braunstein, J.-P. Lang, F. Li, P. Wang, X. Huang, H. Wang, J. Lang, D. J. Young, P. Braunstein, *Angew. Chemie Int. Ed.* **2019**, *58*, 7051–7056.

[150] C. Chen, Y. Tuo, Q. Lu, H. Lu, S. Zhang, Y. Zhou, J. Zhang, Z. Liu, Z. Kang, X. Feng, D. Chen, *Appl. Catal. B Environ.* **2021**, *287*, 119953.

[151] Z. Cai, X. Bu, P. Wang, J. C. Ho, J. Yang, X. Wang, *J. Mater. Chem. A* **2019**, *7*, 5069–5089.

[152] L. Zhang, X. Li, A. Augustsson, C. M. Lee, J. E. Rubensson, J. Nordgren, P. N. Ross, J. H. Guo, *Appl. Phys. Lett.* **2017**, *110*, 104106.

[153] Y. Liang, H. Wang, J. Zhou, Y. Li, J. Wang, T. Regier, H. Dai, **2012**, DOI 10.1021/ja210924t.

[154] Y. Zhang, O. Kizilkaya, H. K. Bilan, R. Kurtz, E. J. Podlaha, *ACS Appl. Energy Mater.* **2020**, *3*, 7239–7245.

[155] D. Drevon, M. Görlin, P. Chernev, L. Xi, H. Dau, K. M. Lange, *Sci. Reports 2019 91* **2019**, *9*, 1–11.

[156] J. Yang, C. Yu, C. Hu, M. Wang, S. Li, H. Huang, K. Bustillo, X. Han, C. Zhao, W. Guo, Z. Zeng, H. Zheng, J. Qiu, *Adv. Funct. Mater.* **2018**, *28*, 1803272.

[157] M. L. Baker, M. W. Mara, J. J. Yan, K. O. Hodgson, B. Hedman, E. I. Solomon, *Coord. Chem. Rev.* **2017**, *345*, 182–208.

[158] X. X. Wang, D. A. Cullen, Y.-T. Pan, S. Hwang, M. Wang, Z. Feng, J. Wang, M. H. Engelhard, H. Zhang, Y. He, Y. Shao, D. Su, K. L. More, J. S. Spendelow, G. Wu, *Adv. Mater.* **2018**, *30*, 1706758.

[159] J. Suntivich, W. T. Hong, Y. L. Lee, J. M. Rondinelli, W. Yang, J. B.

Goodenough, B. Dabrowski, J. W. Freeland, Y. Shao-Horn, *J. Phys. Chem. C* **2014**, *118*, 1856–1863.

[160] L. Zhang, C. Lu, F. Ye, Z. Wu, Y. Wang, L. Jiang, L. Zhang, C. Cheng, Z. Sun, L. Hu, *Appl. Catal. B Environ.* **2021**, *284*, 119758.

[161] R. G. Gast, E. R. Landa, G. W. Meyer, *Clays Clay Miner. 1974 221* **1974**, *22*, 31–39.

[162] B. Wang, K. Zhao, Z. Yu, C. Sun, Z. Wang, N. Feng, L. Mai, Y. Wang, Y. Xia, *Energy Environ. Sci.* **2020**, DOI 10.1039/D0EE00755B.

[163] T. Wu, S. Sun, J. Song, S. Xi, Y. Du, B. Chen, W. A. Sasangka, H. Liao, C. L. Gan, G. G. Scherer, L. Zeng, H. Wang, H. Li, A. Grimaud, Z. J. Xu, *Nat. Catal. 2019 29* **2019**, *2*, 763–772.

[164] Z. Qiu, C. W. Tai, G. A. Niklasson, T. Edvinsson, *Energy Environ. Sci.* **2019**, *12*, 572–581.

[165] J. Jiang, F. Sun, S. Zhou, W. Hu, H. Zhang, J. Dong, Z. Jiang, J. Zhao, J. Li, W. Yan, M. Wang, *Nat. Commun.* **2018**, *9*, 1–12.

[166] J. Zhang, J. Zhang, F. He, Y. Chen, J. Zhu, D. Wang, S. Mu, H. Y. Yang, *Nano-Micro Lett. 2021 131* **2021**, *13*, 1–30.

[167] M. Kim, J. Park, M. Kang, J. Y. Kim, S. W. Lee, *ACS Cent. Sci.* **2020**, *6*, 880–891.

[168] N. Li, D. K. Bediako, R. G. Hadt, D. Hayes, T. J. Kempa, F. Von Cube, D. C. Bell, L. X. Chen, D. G. Nocera, *Proc. Natl. Acad. Sci. U. S. A.* **2017**, *114*, 1486–1491.